University of Salerno

DEPARTMENT OF PHYSICS "E. R. CAIANIELLO"
Doctor of Philosophy in Mathematics, Physics and Applications -
Curriculum Physics - XXXIII cycle - New Series

Doctoral thesis in

Exploring the Transport Properties of Quantum Systems on Different Length Scales

Guerino Avallone

PhD Coordinator:
Prof. C. Attanasio

Tutors:
Prof. C. Attanasio

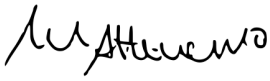

Prof. Jan Aarts

Dr Carla Cirillo

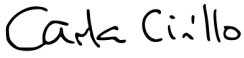

Academic Year 2020/2021

To my Grandparents

Contents

Introduction

QUANTUM MECHANICS has earnestly changed the classical view of Physics, stimulating a half-century of scientific investigation for unusual physical phenomena and technological progress such as computing systems with quantum-enhanced security and speed. For these reasons, the scientific community is in continuous fervour to make Quantum Technologies a reality. Indeed, novel materials, which frequently exhibit unexpected or even revolutionary physical properties, are essential for significant advances in fundamental Physics knowledge and to increase technological progress. In this respect, simultaneous control of structural and physical properties through a small electrical current or voltage is of extreme relevance, and have been a long-desired but elusive aim of science.

Contemporary studies of spin-orbit-coupled materials, especially 4d- and 5d-transition metal oxides [1, 2], have provided a strong indication that this goal may be finally achieved [3–5]. These metal oxides highlight strong spin-orbit coupling and host uncommon energy scales defined by comparable and competing spin-orbit and Coulomb interactions. This energy configuration produces a unique interplay between the fundamental interactions and places these materials poised between different ground states. Consequently, these materials are very susceptible to even small external stimuli [6, 7]. In this scenario, the electrical current as a new external stimulus (joining the magnetic and electric field, pressure, light, etc) is surprisingly effective. Indeed, the electrical current can couple to the lattice and expands it, thus generating new electronic arrangements or ground states. In this regard, the Mott insulators form a fascinating research platform.

In this thesis, we first introduce some theoretical aspects of Mott insulators, then we concentrate our experimental research on pure single crystals

of Ca_2RuO_4 in which application of a small current causes drastic changes in both structural and physical properties. In particular, we combined electrical transport and x-ray diffraction measurements to refine the crystallographic structural phases induced by electrical current.
Moreover, we electrically characterised the eutectic system constituted by Ca_2RuO_4 with embedded metallic Ru inclusions. Our study on this system shows that it can be relevant for electronic applications since it maintains the properties of the pure system but is structurally stiffer.

Although it is much debated whether the insulate to metal transition in Ca_2RuO_4 is a result of Joule heating or electronic effects, a parameter that has been left unexplored in this context is the size of the samples. Here, we have tackled this issue by utilising an innovative technique that involves a Ga^+ focused ion beam to prepare microscopic samples out of bulk crystals of Ca_2RuO_4. That not only allowed adequate measurements of samples since the geometry of the micro-crystal has been accurately controlled but also gave us the possibility to establish that the size of the samples is a tuning parameter of the electrical transport properties of this material. Generally, with Ca_2RuO_4, the main difficulty is accessing the local sample temperature that makes the local Joule heating out of control, and this can give rise to deceptive behaviour. Therefore, extreme care must be taken to assure that the current-controlled phenomena in Ca_2RuO_4 are intrinsic. For this reason, we carefully evaluated the role of the local unavoidable Joule heating in our experiment. Indeed, exploiting the potentiality of our microscopic samples, we have lithographically fabricated a platinum thermometer directly on top of selected microscopic samples. This way, we ensured the robustness of the observed phenomena by ruling out any possible effect coming from Joule heating.
In conclusion, we believe that our results on the Mott insulator Ca_2RuO_4 have greatly improved the current scientific understanding of this complex system.

The "non-conventional" searching of these exotic quantum properties have also been studied in another flavour of the Physics field: The Superconductivity.
In the majority of physical systems, the individual quantum states start to smear by increasing the number of interacting particles. As a result, almost all the charming characters of quantum mechanics are typically observed in systems with less than few atoms. Superconductors, however, do not suffer

this drawback, making them an ideal platform for investigating quantum phenomena. In fact, in superconductors, due to the bosonic nature of the Cooper pairs [8], there is only one order parameter that can represent the whole superconducting condensate. On the other hand, this does not mean that the size of a superconducting system has no importance. On the contrary, mesoscopic systems can give considerably better control over superconductivity. Indeed, they can be employed to identify some of the unique and exotic quantum states in nature that are crucial to our comprehension of the mechanisms involved in some of the most debatable phenomena of modern Physics.

The behaviour of any quantum system is determined by its wave function. In superconductors, this corresponds to the pairing function of the electrons that form the Cooper pairs. A superconductor can therefore be characterized by the type of symmetry that defines its pairing function. However, it is well established by the Pauli principle that fermions, such as electrons, can only be paired with each other if their combined wavefunction is antisymmetric. One way to satisfy this condition would be if the pairing occurred between electrons with opposite spins. This turns out to be the case with conventional superconductors. There is, however, no reason for this to be the only stable configuration. Cooper pairs can also be formed by electrons of equal spin as long as its total wave function is odd. This is the case of unconventional superconductors. Moreover, in superconductors with inversion symmetry, the parity symmetry imposes a constraint on the pairing state, which must be either spin-singlet with even parity (conventional superconductors) or spin-triplet with odd parity (unconventional superconductors). On the other hand, there is another class of superconductors without an inversion centre known as non-centrosymmetric superconductors. In this case, the broken parity symmetry is expected to give rise to an admixture of spin-triplet and spin-singlet pairing states. However, experimental confirmation of pairing mixing remains still elusive. In the last chapter of this thesis, we will introduce the Little-Parks experiment as a way to establish the symmetry of the Cooper pairing. This phase-sensitive experiment can be helpful in determining the presence of spin-triplet components in polycrystalline rings of non-centrosymmetric superconductors [9]. The experiment was performed on a submicrometer-sized ring array designed for field-dependent transport measurements on the non-centrosymmetric superconductor $Nb_{0.18}Re_{0.82}$. The main reason to use such a mesoscopic structure in our studies is related to the possible observation of an unusual state known as the half-quantum flux. Such state can form

equal-spin triplet pairing, and in contrast to the classic full-quantum flux, it is accompanied by a spin current whose free energy grows logarithmically with the dimensions of the system. Consequently, the half-quantum flux states become energetically less favourable and improbable to stabilise in macroscopic (bulk) systems. Our preliminary results on the anomalous behaviour of the magnetovoltage curves suggest that these anomalies could be originated by unconventional superconducting mechanisms in $Nb_{0.18}Re_{0.82}$. However, the experimental work is still in progress.

OUTLINE OF THE THESIS

- **Chapter 1** (*Mott Insulators*) provides a general theoretical introduction to the Mott insulators. The focus of this chapter is then directed towards a peculiar member of this family, Ca_2RuO_4, whose particular known properties are presented here.

- **Chapter 2** (*Properties of Ca_2RuO_4 Induced by Current and Voltage*) is related to the current induced electrical and structural properties of mm-sized samples of pure Ca_2RuO_4 single crystals, and with the voltage and current induced electrical properties of mm-sized samples of the eutectic system Ca_2RuO_4-Ru (Ca_2RuO_4 with embedded Ru inclusions).

- **Chapter 3** (*Universal size-dependent nonlinear charge transport in single crystals of the Mott insulator Ca_2RuO_4*). Here we present a totally new effect in Ca_2RuO_4. We discovered that reducing the size of the samples down to μm range we find a four orders of magnitude increase in the current density required for driving the material out of the insulating state into a metastable phase that is the precursor to the fully metallic one. Furthermore, fabricating a microscopic platinum thermometer directly on the microscopic Ca_2RuO_4 samples, and performing thermal simulations, we gain insight into the local temperature during simultaneous application of current, and established that the size dependence is not a result of Joule heating.

- **Chapter 4** (*Unconventional Features of Non-Centrosymmetric Superconductors*) is based on unconventional superconductors with an emphasis on the non-centrosymmetric ones. Here, we introduce the non-centrosymmetric superconductor $Nb_{0.18}Re_{0.82}$ that we employed to investigate its unconventional nature in terms of pairing symmetry and physical features. The last section of this chapter revisits the Little-Parks half-quantum flux in $Nb_{0.18}Re_{0.82}$ as a powerful phase-sensitive experiment. We report the fabrication method to obtain a $Nb_{0.18}Re_{0.82}$ array of submicrometer-sized rings, and our preliminary measurements.

The research presented in this thesis, being an experimental work that deals with extremely complicated systems, fabrication techniques, and measurements, has been strongly affected by the COVID-19 pandemic since it has slowed down the experimental activities.

Chapter 1

Mott Insulators

The transport of electrons is a fundamental matter at the basis of science in any field. In general, the directed motion of energy, charge, spin, etc., is a process that happen out of thermodynamic equilibrium. Moreover, in the case of electron transport in a solid there are also three different effects to be accounted: the potential of the ions, the electron-electron interaction, and externally applied fields. In view to treat the basic theoretical aspect of the Mott metal-insulator transition, let's provide the definition for metal and insulator and a schematic division of this latter using the dominant interaction that causes the insulating behaviour as a criterion.

For interacting many-particle systems far from thermal equilibrium, a very complex formalism has to be employed to calculate transport properties. Here we consider the conducting properties near thermal equilibrium, hence the presence of any external perturbations is "small". Therefore, to ensure the validity of Ohm's law we restrict to the case of weak external fields.

Another restriction we need to take into account is that the distinction between metal and insulator is strictly meaningful only at zero temperature ($T = 0$). One could think this is only a theoretical simplification but, the limit $T \to 0$ is actually of fundamental importance to distinguish between metal and insulator. With these restrictions in mind, we may define an insulator in terms of its static electrical conductivity, σ^{DC}, in momentum and frequency space as

$$\sigma^{DC}_{\alpha\beta}(T=0) \equiv \lim_{T\to 0}\lim_{\omega\to 0}\lim_{|\mathbf{q}|\to 0} Re\{\sigma_{\alpha\beta}(\mathbf{q},\omega)\} = 0 \tag{1.1}$$

where $\alpha, \beta = 1, ..., d$ being d the dimension of the system.

In the case of a finite metallic conductivity at small frequencies we may apply the Drude model that yields

$$Re\{\sigma_{\alpha\beta}(T=0,\omega\to 0)\} = (D_c)_{\alpha\beta}\frac{\tau}{\pi(1+\omega^2\tau^2)} \tag{1.2}$$

where $(D_c)_{\alpha\beta}$ is the Drude weight and τ is the *mean free time*. Suppose we have no scattering, then in this case the translational invariance is restored and $\tau^{-1}\to 0$ which leads to the case of an ideal metal. In that situation the equation (1.2) becomes

$$Re\{\sigma_{\alpha\beta}(T=0,\omega\to 0)\} = (D_c)_{\alpha\beta}\delta(\omega) \tag{1.3}$$

The assumption to consider $T=0$ and small external fields allows us to identify two basic categories of insulators. Indeed we can distinguish insulators due to the electron-ion interaction, and those due to the electron-electron interaction. If we consider only static ion configurations, then the insulators due to the electron-ion interaction can be understood in terms of a single-electron theory. The following classes of insulators are prominent representatives:

- Bloch-Wilson or band insulators
- Peierls insulators
- Anderson insulators

The Bloch-Wilson insulators are materials due to the electrons' interaction with the periodic potential of the ions while the Peierls insulators are due to the electrons' interaction with static lattice deformations, and the Anderson insulators to the presence of disorder, e.g., the electrons' interaction with impurities and other lattice imperfections.

The insulators due to the electrons' mutual interaction are conceptually different. In this case, we can define another class of insulators, the so called *Mott insulators*. In other words, Mott insulators constitute a category, where the insulating behaviour is understood as a cooperative many-electron phenomenon. However, it is possible to distinguish further between Mott-Heisenberg and Mott-Hubbard insulators, depending on whether or not there is long-range order in the charge and/or spin density of the electrons.

In real materials the interactions used in the above classification scheme are always simultaneously present such that the classification of experimen-

tally observed insulators is not always that straightforward. In fact, an observed metal-insulator transition need not be dominated by one interaction alone to the exclusion of the others. Although a single interaction may drive the transition, its nature often is strongly affected by the others. In the vicinity of the transition they can become relevant perturbations. Here we will address only "pure" cases of Mott transitions, where the Coulomb interaction dominates the others throughout the transition.

1.1 Theoretical Aspects

In this section, we introduce some basic theoretical concepts that allow to understand the role of electron-electron interactions in the solid-state. Its influence on low-energy properties is successfully included in metals in the Landau's Fermi-liquid theory that fails at the metal-insulator transition. It is immediately clear that the problem of the Mott transition is strictly related to the stability of Fermi-liquid theory thus the contribution of the electron-electron interactions plays a key role.

To evaluate the strength of the electron-electron interaction, with respect to the electrons' kinetic energy, we will introduce the pair correlation function and the local magnetic moment. This way, we can naturally introduce the Mott insulators.

Considering independent electrons may seem a very unrealistic assumption since the Coulomb interaction is long-range and strong. Nevertheless, many experiments can be explained qualitatively and even semi-quantitatively neglecting it. However, there are two aspects that explain the remarkable success of the independent electron approximation and how, in many cases, the interaction can qualitatively be taken into account. First, in systems with itinerant electrons the Coulomb interaction between the charge carriers is very effectively screened within the inverse of the Fermi wave number k_F^{-1}. Secondly, let's consider a set of noninteracting electrons and imagine to gradually switch on the interactions between them. What happen now is that the energies of each one-electron level will be modified as in the Hartree-Fock approximation and its refinements. Moreover, electrons will be scattered in and out of the single electron levels, which are no longer stationary. This does not happen in the Hartree-Fock approximation, where one-electron levels continue to give valid stationary states of the interacting system. Whether this scattering is relevant enough to invalidate the independent electron pic-

ture depends on how rapid the rate of scattering is. One may think that the electron-electron scattering rate is quite high since the Coulomb interaction is rather strong. However, the Pauli principle comes to gives us a lifeline by reducing the scattering rate in many cases of major interest. Indeed, in the presence of a Fermi surface the scattering rate between electrons near the Fermi surface with energy $E_F + \omega$ vanishes proportional to ω^2 since the exclusion principle strongly reduces the number of scattering channels that are compatible with energy conservation. This concept is at the base of Landau's Fermi-liquid theory [10, 11].

Suppose a Fermi surface exists for the interacting Fermi system as for the non-interacting case (Fermi gas). In that case, the excitations near the Fermi surface are long-living fermions (*Landau quasi-particles*) in a one-to-one correspondence to the electron and hole excitations of the Fermi gas. Thus the energetically low-lying one-electron excitations of the Fermi gas and the Fermi liquid can be mapped completely onto each other. Since the Fermi energy in metals is almost always very much larger than typical thermal energies, only low-energy excitations are relevant for the thermodynamics and electrical transport properties. The residual interaction between Landau quasiparticles can effectively be described in terms of a few Landau parameters. Consequently, physical properties are only quantitatively modified in a Fermi liquid as compared to a Fermi gas. However, there is no qualitative difference between a Fermi gas and a Fermi liquid, both describe metallic states. Under which conditions a Fermi surface exists remains an open problem within the solely phenomenological Fermi-liquid theory. We can only base on the physical point of view the self-consistency of the Fermi-liquid picture in describing the influence of electron-electron interactions in metals. Indeed, we can argue that the electrons are highly mobile in the crystal, thus their mutual interaction is well screened. Therefore, we may apply Fermi-liquid theory for their description, which implies that the screened electron-electron interaction does not qualitatively change the picture, which was the starting point of our analysis. It is clear, as we anticipated before, that these arguments have to break down at the metal-Mott insulator transition.

Exchange and Correlations

The dynamic self-screening of itinerant electrons is one of the most important effect in metals. However, most of the time, the interaction effects cannot be

simply neglected, or merely subsumed into an effective single-electron description. In general, the repulsive electron-electron interaction tends to keep the electrons apart from each other. This localization tendency is in conflict with the electrons' kinetic energy that tries to spread out the electrons over the whole crystal. To evaluate the effective strength of the electron-electron interactions as compared to their kinetic energy, a quantitative parameter needs to be defined.

Let's consider s electrons with spin $\sigma = \uparrow, \downarrow$ and electron density n (where n is the ratio of the number of electrons to the number of ions, $n = N_e/N_I$). In second quantization it is possible to define the Fermi creation and annihilation operators for σ electrons in position space as $\hat{\psi}^+_\sigma(\mathbf{r})$ and $\hat{\psi}_\sigma(\mathbf{r})$, respectively, and the corresponding particle density operators $\hat{n}_\sigma(\mathbf{r}) = \hat{\psi}^+_\sigma(\mathbf{r})\hat{\psi}_\sigma(\mathbf{r})$, $\hat{n}(\mathbf{r}) = \sum_\sigma \hat{n}_\sigma(\mathbf{r})$. The average potential energy for the Coulomb interaction between these electrons is given by

$$\langle V \rangle = \sum_{\sigma,\sigma'} \int d\mathbf{r} d\mathbf{r}' \frac{e^2}{|\mathbf{r} - \mathbf{r}'|} \langle \hat{\psi}^+_\sigma(\mathbf{r}) \hat{\psi}^+_{\sigma'}(\mathbf{r}') \hat{\psi}_{\sigma'}(\mathbf{r}') \hat{\psi}_\sigma(\mathbf{r}) \rangle \tag{1.4}$$

Now, to determine the strength of the electron-electron interaction from (1.4) we need to know the probability distribution to find a σ' electron at $\mathbf{r}'$ when there already is a σ electron at $\mathbf{r}$. This information is contained in the pair correlation function g

$$g_{\sigma,\sigma'}(\mathbf{r}, \mathbf{r}') = \langle \hat{\psi}^+_\sigma(\mathbf{r}) \hat{\psi}^+_{\sigma'}(\mathbf{r}') \hat{\psi}_{\sigma'}(\mathbf{r}') \hat{\psi}_\sigma(\mathbf{r}) \rangle - \langle \hat{n}_\sigma(\mathbf{r}) \rangle \langle \hat{n}_{\sigma'}(\mathbf{r}') \rangle \tag{1.5}$$

It is worth to note that this quantity differs from the expectation value we need for the evaluation of (1.4) by the subtraction of a product of two-fermion expectation values. The reason for this is twofold: first, we expect the pair correlation function $g_{\sigma,\sigma'}(\mathbf{r}, \mathbf{r}')$ to vanish at large electron separation. Second, if the probability of finding a σ electron at $\mathbf{r}$ is independent of the σ' electron at $\mathbf{r}'$, the pair correlation function as defined in (1.5) will indeed vanish. Hence, $g_{\sigma,\sigma'}(\mathbf{r}, \mathbf{r}')$ measures the correlations in the system.
In the pair correlation function there is the contribution due to the particle statistics (Pauli exclusion principle) and the pure electron correlations induced by the electron-electron interaction. Following, we address these two contributions separately.

The Pauli principle guarantees that two electrons of the same spin cannot

occupy the same orbital. Hence, the pair correlation function for electrons with like spin is different from zero even if no electron-electron interaction was present. Considering for example the three-dimensional homogeneous Fermi-gas ground state, we have

$$g_{\sigma,\sigma'}(\mathbf{r},\mathbf{r}') = -\left[\left(\frac{3n}{2}\right)\frac{\sin x - x\cos x}{x^3}\right]^2 \tag{1.6}$$

hence on the scale of the reciprocal Fermi wave number $1/k_F$ the Pauli principle reduces the probability to find a σ electron in the vicinity of another σ electron (*exchange hole*). This effect is completely independent of the presence of electron-electron interactions and is only due to the Fermi statistics of the electrons. For electrons with different spin quantum numbers the exclusion principle does not hold, thus

$$g_{\sigma,-\sigma}(\mathbf{r},\mathbf{r}') = 0 \tag{1.7}$$

this means that $\uparrow$ and $\downarrow$ spins are entirely uncorrelated in the Fermi gas.

To illustrate how the Pauli principle leads to an "exchange interaction" we can consider the exact N-electron Schrödinger equation in the equivalent variational form, which affirm that a solution to $H\Psi = E\Psi$ is given by any Ψ that makes stationary the quantity

$$\langle H\rangle_\Psi = \frac{(\Psi, H\Psi)}{(\Psi,\Psi)} \tag{1.8}$$

with $(\Psi,\Phi) = \sum_{s_1}\ldots\sum_{s_N}\int d\mathbf{r}_1 \ldots d\mathbf{r}_N \Psi^*(\mathbf{r}_1 s_1,\ldots,\mathbf{r}_N s_N)\Phi(\mathbf{r}_1 s_1,\ldots,\mathbf{r}_N s_N)$ and H is the Hamiltonian. Particularly, the ground state wave function is the one that minimizes (1.8). A suitable choice is a Ψ that is a Slater determinant of one-electron wave functions, namely

$$\Psi(\mathbf{r}_1 s_1, \mathbf{r}_2 s_2, \ldots, \mathbf{r}_N s_N) = \begin{vmatrix} \psi_1(\mathbf{r}_1 s_1)\psi_1(\mathbf{r}_2 s_2) & \ldots & \psi_1(\mathbf{r}_N s_N) \\ \psi_2(\mathbf{r}_1 s_1)\psi_2(\mathbf{r}_2 s_2) & \ldots & \psi_2(\mathbf{r}_N s_N) \\ \vdots & & \vdots \\ \psi_N(\mathbf{r}_1 s_1)\psi_N(\mathbf{r}_2 s_2) & \ldots & \psi_N(\mathbf{r}_N s_N) \end{vmatrix} \tag{1.9}$$

Indeed, is relatively easy to show that the (1.9) is the simplest combination that satisfy the Pauli principle which requires the sign of Ψ to change when

any two of its arguments are interchanged

$$\Psi(\mathbf{r}_1 s_1, ..., \mathbf{r}_i s_i, ..., \mathbf{r}_j s_j, ..., \mathbf{r}_N s_N) = -\Psi(\mathbf{r}_1 s_1, ..., \mathbf{r}_j s_j, ..., \mathbf{r}_i s_i, ..., \mathbf{r}_N s_N) \tag{1.10}$$

Using (1.9) in (1.8) and minimizing this latter with respect to the ψ_i^* leads to the so called Hartree-Fock equations

$$\begin{aligned} -\frac{\hbar^2}{2m}\nabla^2\psi_i(\mathbf{r}) + U^{ion}(\mathbf{r})\psi_i(\mathbf{r}) + U^{el}(\mathbf{r})\psi_i(\mathbf{r}) - \\ + \sum_j \int d\mathbf{r}' \frac{e^2}{|\mathbf{r}-\mathbf{r}'|}\psi_j^*(\mathbf{r}')\psi_i(\mathbf{r}')\psi_j(\mathbf{r})\delta_{s_i s_j} = \epsilon_i \psi_i(\mathbf{r}) \end{aligned} \tag{1.11}$$

the last term on the left side is the *exchange term.* Due to this term, the (1.11) are usually quite intractable except for the Fermi gas. Indeed, when the periodic potential is zero (or constant) the Hartree-Fock equations can be solved exactly by using a set of orthonormal plane waves as ψ_i. Furthermore, we can evaluate the energy of the $N-$electron system that now include the electron-electron interaction that yields to

$$E = N\left[\frac{3}{5}\epsilon_F - \frac{3}{4}\frac{e^2 k_F}{\pi}\right] \tag{1.12}$$

this equation is usually expressed in terms of the rydberg (1 Ry$= e^2/2a_0$) and the parameter r_s/a_0 where r_s is defined as the radius of a sphere whose volume is equal to the volume per conduction electron, and a_0 is the Bohr radius

$$\frac{E}{N} = \left[\frac{2.21}{(r_s/a_0)^2} - \frac{0.916}{r_s/a_0}\right] \text{Ry} \tag{1.13}$$

the first term is the usual energy contribution in the non-interacting electrons picture, while the second one is due to the exchange term and is known as *exchange interaction.* For example, this energy contribution is crucial to explain ferromagnetism in transition metals and is also at the basis of the metal-insulator transition in the Slater theory.
It is important to note that in metals the ratio r_s/a_0 is in $2 \div 6$ range. Consequently, the second term in (1.13) is the same order of magnitude of the first one, indicating that electron-electron interactions cannot be neglected in any free electron evaluation of the electronic energy of a metal.

However, in a high-density expansion (i.e., small r_s/a_0) of the ground-

state energy of the electron gas, M. Gell-Mann et al. [12] have calculated that E/N is

$$\frac{E}{N} = \left[\frac{2.21}{(r_s/a_0)^2} - \frac{0.916}{r_s/a_0} + 0.0622\ln(r_s/a_0) - 0.096 + O(r_s/a_0)\right] \text{Ry} \quad (1.14)$$

the first two terms are the Hartree-Fock result (1.13) while the next two and all other corrections are conventionally known as the *correlation energy.*

The true many-body effects, over the exchange effect, is contained in the correlation function $g_{\sigma,-\sigma}(\mathbf{r},\mathbf{r}')$ between electrons of different spin. However, as we have seen above, the Fermi statistics of the electrons produces an "exchange term" between electrons of the same spin (consequently $g_{\sigma,\sigma'}(\mathbf{r},\mathbf{r}') \neq 0$), but sometimes this effect is misleadingly interpreted as the result of "correlations" instead of "exchange".

We refer to systems with a non-vanishing pair correlation function between $\uparrow$ and $\downarrow$ electrons as "correlated electron systems". Naturally, the interaction also changes the correlation function between electrons of the same spin species. If the pair correlation functions for electrons of the same spin and electrons of opposite spin are comparable in size, the system is termed "strongly correlated". In general, a σ electron will not only be surrounded by an exchange hole but also by a "correlation hole" since the repulsive electron-electron interaction will also prevent electrons of different spin to come close to each other. In contrast to Slater's views Mott emphasizes the significance of correlations for the understanding of the metal-insulator transition.

Magnetic Moments

Unfortunately, the pair correlation function is not easily accessible either experimentally or theoretically. Consequently, one have to restrict to a less complete and more local probe of systems' properties. Thus we focus ourselves to the terms $\mathbf{r} = \mathbf{r}'$ in the pair correlation function $g_{\sigma,\sigma'}(\mathbf{r},\mathbf{r}')$. In other words, we suppose our electrons moving on a lattice with sites $\mathbf{R}$.

Using natural units and choosing the z axis as the quantization axis, is possible to define the local magnetic moment in the z direction as

$$[M^z(\mathbf{R})]^2 = \langle \hat{S}^z(\mathbf{R})\hat{S}^z(\mathbf{R})\rangle \quad (1.15)$$

where $\hat{S}^z(\mathbf{R}) = (\hat{n}_\uparrow(\mathbf{R}) - \hat{n}_\downarrow(\mathbf{R}))/2$. We can write the instantaneous magnetic

moment into three positive definite terms, namely

$$[M^z(\mathbf{R})]^2 = [M^z(\mathbf{R})]^2_{FG} + [M^z(\mathbf{R})]^2_{LRO} + [M^z(\mathbf{R})]^2_C \tag{1.16}$$

The Fermi-gas contribution $[M^z(\mathbf{R})]^2_{FG} = 1/8\langle\hat{n}(\mathbf{R})\rangle(2-\langle\hat{n}(\mathbf{R})\rangle)$, is a consequence of the Pauli principle, thus reflects the particle statistics only, therefore can be ignored in discussions of local moments due to interactions. The second term $[M^z(\mathbf{R})]^2_{LRO} = 1/2\langle\hat{S^z}(\mathbf{R})\rangle^2$ is non-zero only if the spin rotational symmetry is broken, for example as a result of ferromagnetism or antiferromagnetism. This term is referred as the contribution due to "long-range order". The last term $[M^z(\mathbf{R})]^2_C = -1/2g_{\uparrow,\downarrow}(\mathbf{R},\mathbf{R})$ is the "correlation contribution" to the moment. It is the importance of this term that is emphasized in Mott's view.
The relative local moment defined as $[M^z(\mathbf{R})]^2_{Rel} = [M^z(\mathbf{R})]^2 - [M^z(\mathbf{R})]^2_{FG}$ may not show up in low-energy properties in the metallic phase but it is nevertheless present at finite frequencies for all non-zero interaction strengths. As a consequence, a proper description of the metal-insulator transition where the low-energy (Fermi-liquid) picture breaks down must necessarily include the effects of local moments.

Mott Insulator

Following Mott's description, if there are no moments formed, a Mott insulator would be a metal. Also he emphasizes that this notion "... *depends on the existence of moments and not on whether or not they are ordered*". This is reflected, for example, in the fact that "*for an antiferromagnetic insulator the most important property is that the magnitude of the Hubbard gap is not greatly affected when the temperature goes through the Néel point* T_N" [13].

The pre-formed local moments arise because the electrons try to stay away from each other to keep at minimum their Coulomb repulsion. Furthermore, the electrons may but need not localize on different sublattices as in Slater's view.

These arguments lead to the following definition of a Mott insulator: *for a Mott insulator the electron-electron interaction leads to the occurrence of (relative) local moments. The gap in the excitation spectrum for charge excitations may arise either from the long-range order of the pre-formed moments (Mott-Heisenberg insulator) or by a quantum phase transition induced by charge and/or spin correlations (Mott-Hubbard insulator)* [14].

Mott-Hubbard Insulator

Mott [15,16] provided the following example for a metal-insulator transition (see also [13]) which is formalized in the Hubbard model and also, more precisely, in the Harris-Lange model.

Consider a d-dimensional cubic lattice with a constant a and hydrogen atoms with Bohr radius a_B arranged on it. The L lattice sites are provided by protons for $N = L$ electrons (half filling).

To formulate the potential energy part of our Hamiltonian we assume that the effective electron-electron interaction will be local. We can define now the intra-atomic energy, ionization energy minus electron affinity called the "Hubbard" U

$$U = E(\mathrm{H} \to \mathrm{H}^+) - |E(\mathrm{H} \to \mathrm{H}^-)| \tag{1.17}$$

In this picture it is tacitly assumed that the electrons dominantly sit *on* and not *between* the lattice sites. Moreover, we assume that electrons may hop between neighboring atoms. This "tight-binding" approximation for independent electrons [17] (tunneling between nearest neighbors on a cubic lattice) results in a cosine dispersion relation

$$\epsilon(\mathbf{k}) = -2A_t \sum_{l=1}^{d} \cos(k_l a) \tag{1.18}$$

with a bandwidth $W = 2ZA_t$, where $Z = 2d$ is the number of nearest neighbors and $A_t > 0$ is the tunnel amplitude which depends on a/a_B.

At large distances between the H atoms, $a \gg a_B$, the overlap between the atomic wave functions is small, which implies $W \ll U$. In the ground state every lattice site will be singly occupied since we are at half band-filling. The Fig. 1.1 illustrates the situation schematically. The energy $\mu^+(N) = E_0(N+1) - E_0(N)$ necessary to add another electron is given by $\mu^+(N = L) = U - W_1/2$ since charge excitations with energy U are mobile such that they form a band of width $W_1 = W_1(U/W)$ (see Fig. 1.1(a)). This band is the "upper Hubbard band", which is generally not a one-electron band. Instead, it describes the spectrum of charge excitations for an extra electron added to the ground state of the half-filled electron system. The energy required to remove an electron, $\mu^-(N) = E_0(N) - E_0(N-1)$, is given by $\mu^-(N = L) = +W_2(U/W)/2$. The corresponding spectrum for the removal of a charge

from the half-filled ground state constitutes the "lower Hubbard band" (see Fig. 1.1(b)). At half band-filling and for $(W_1 + W_2)/2 \ll U$ we expect that the chemical potential $\mu(N)$ is not continuous, but a gap for charge excitations occurs, $\Delta\mu(N = L) = (\mu^+ - \mu^-)(N = L) \approx U - (W_1 + W_2)/2 > 0$. Since we find an energy gap for charge excitations at half band-filling, if $(W_1 + W_2)/2 \approx W \ll U$, the system is an insulator. Moreover, a gap for a single charge excitation implies a vanishing DC conductivity if electron pairing is absent.

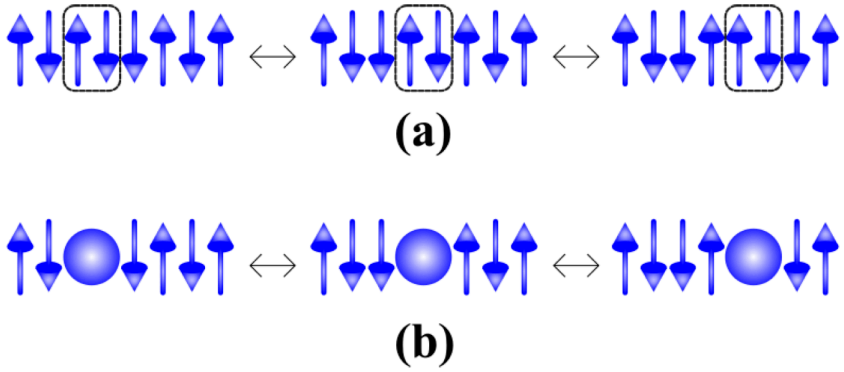

Fig. 1.1: (a) Electrons coherently move as double occupancies in the upper Hubbard band and (b) as holes in the lower Hubbard band.

In a thought experiment we may now reduce the distance between the hydrogen atoms, which increases the overlap in their atomic wave functions and corresponds to an enhancement of the screening and the electrons' tendency to delocalize. The combined bandwidth of the upper and lower Hubbard band $W_1 + W_2$ increases accordingly: the two bands finally overlap for $a \approx a_B$, and the gap for charge excitation vanishes. Low-energy excitations hardly change the charge distribution in this situation and thus are gapless. For $W \gg U$ the system is a paramagnetic metal, while for intermediate values, around $U \approx W$, we expect a metal-insulator transition. This transition appears to be a metal-band insulator transition since the upper and lower Hubbard band begin to "overlap". However, these bands do not represent single-electron states; the transition is at heart a consequence of electron correlations, and not merely the result of a simple band crossing. These considerations lead us to the following definition of a Mott-Hubbard insulator. For a Mott-Hubbard insulator the electron-electron interaction leads to the formation of a gap in the spectrum for single charge excitations. The correlations force a quantum phase transition from a correlated metal to a paramagnetic Mott-Hubbard insulator, in which the local magnetic moments do not display long-range order.

We will observe drastic changes in the resistivity even at finite temperatures when we go through the quantum phase transition value for our external parameters (e.g., pressure) that control the relative strength of the electrons' kinetic and potential energy, U/W. For temperatures small compared to the single-electron gap, $k_{\mathrm{B}}T \ll \Delta\mu$, we may then speak of a "Mott-Hubbard insulator" in practical terms even at finite temperatures.

Mott-Heisenberg Insulator

In our above discussion of the Mott-Hubbard insulator we did not consider the possibility of an ordering of magnetic moments. Thus, the concept of the Mott-Hubbard insulator has to be supplemented by that of the Mott-Heisenberg insulator for which the insulating state displays long-range order. What we totally ignored in the previous subsection was the exchange interaction between localized spins. Even for $U \gg W$ the tunneling of electrons to neighboring sites is allowed ("virtual" hopping processes). Formal perturbation theory in second order around the half-filled ground state with all electrons localized provides an antiferromagnetic coupling $J \sim A_t^2/U$ between the spin-1/2 electrons on neighboring lattice sites ("itinerant exchange") [18]. For large interactions, $U \gg W$, and half band-filling the energy scales for charge excitations ($\Delta\mu \approx U - W$) and spin excitations ($J \sim A_t^2/U$) are well separated. We are in the Mott-Hubbard insulating regime since the gap $\Delta\mu \approx U - W$ due to the quantum phase transition at $U \approx W$ is finite. The spin energy scale, however, cannot be ignored for temperatures around or below that of the corresponding exchange interaction. The local magnetic moments in the Mott-Hubbard insulator may long-range order at the temperature $k_{\mathrm{B}}T_{\mathrm{N}} = O(ZJ) \ll \Delta\mu$. The system goes over from the Mott-Hubbard insulator into the (antiferromagnetic) Mott-Heisenberg insulator in a thermodynamic phase transition at $T = T_{\mathrm{N}}$. According to Mott [13] the size of the local moments does not change much in the transition through the Néel temperature. For small interactions, below the quantum phase transition at $U \approx W$, the Mott-Hubbard gap is absent but correlations for all $U > 0$ lead to preformed magnetic moments. Again, these moments may long-range order at the Néel temperature, and we observe a thermodynamic phase transition from a paramagnetic (correlated) metallic state into the (antiferromagnetic) Mott-Heisenberg insulating state. Again, the magnitude of the local moments does not change (much) at the Néel temperature. These

considerations lead us to the following definition of the Mott-Heisenberg insulator. The Mott-Heisenberg insulating state is the result of a thermodynamic phase transition in which the pre-formed local (magnetic) moments (antiferromagnetically) order below the critical (Néel) temperature. Above the Néel temperature the Mott-Heisenberg insulator goes into a paramagnetic phase, which can either be a correlated metal or the Mott-Hubbard insulator. We emphasize that, the moments are already present in the Mott-Heisenberg insulating state and remain in the paramagnetic metallic phase above the transition temperature. Since pre-formed moments, the important signature of electron correlations, order at the metal-insulator transition we introduced the concept of the "Mott-Heisenberg insulator" to provide a clear distinction between the ideas of Slater (self-consistent single-electron theory) and Mott (many-electron correlations).

1.2 Ca_2RuO_4

The Mott-Hubbard insulator Ca_2RuO_4 (hereafter Ca214) was synthesized for first time in 1997 at the Kyoto University, Japan [19]. It is a noncuprate ruthenium layered perovskite belonging to the solid solution series $Ca_{2-x}Sr_xRuO_4$. The one end member ($x = 2$) is the Sr_2RuO_4 [20] (hereafter Sr214), supposed to be a spin-triplet superconductor, while complete substitution ($x = 0$) of isovalent Ca changes the superconductor into the Mott insulator Ca214 by introducing distortions to RuO_6 octahedra which correspond to compressions, tilting and rotations [21]. However, both Sr214 and Ca214 have the single-layered tetragonal K_2NiF_4 structure. In Fig. 1.2 a schematic draw of the Ca214 crystalline structure is reported. We can think of it as made of RuO_2 layers built up of corner-sharing RuO_6 octahedra (space group *Pbca*, $a = 0.5402$ nm $b = 0.5493$ nm $c = 1.1932$ nm). The unique crystal structure of Ca214, and in particular the role of the octahedra deformations, are at the basis of its peculiar physics properties. Indeed, the distortion induced in the lattice structure by Sr $\rightarrow$ Ca substitution lowers the crystal symmetry from cubic to orthorhombic, resulting in significant changes in magnetic, electronic, and structural properties [22–24].

The ground state of Ca214 is antiferromagnetic (AFM) insulating. With increasing temperature, it becomes paramagnetic (PM) insulating at the Néel temperature $T_N = 113$ K. Further increasing on temperature leads it to perform a thermally driven Mott insulator-to-metal transition (IMT) bringing

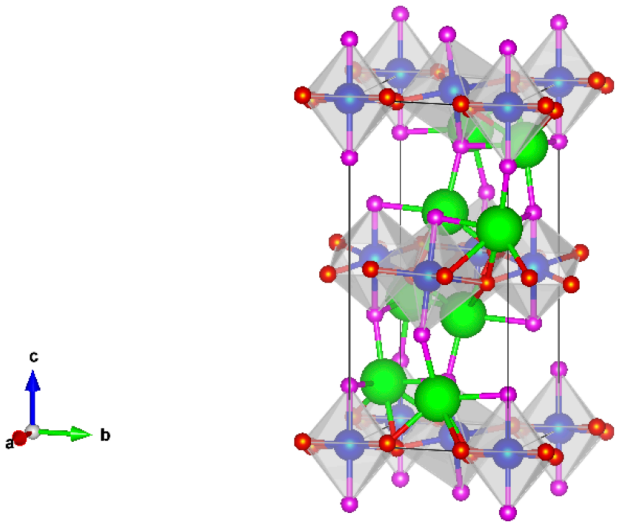

Fig. 1.2: Crystalline structure of Ca214.

the material in a PM metallic state at $T_{IMT} = 357$ K.

The IMT is first order, as evidenced by the observation of thermal hysteresis. Further, the transition is driven by an elongation of the RuO_6 octahedra with increasing temperature through IMT temperature, and therefore the insulating and metallic states are characterized by short *S-Pbca* and long *L-Pbca* *c*-axis lattice parameters, respectively [24, 25].

In the insulating phase, Ca214 shows an orbital order. This orbital-ordered insulating phase is highly sensible for external stimulations such as pressure application, which induces a ferromagnetic metal and subsequently a superconducting state with a critical temperature below 0.4 K [26].

The most remarkable feature that Ca214 shows is the electrically driven Mott IMT. Indeed, recently, low electric-field-induced IMT and current induced IMT have been observed in Ca214 [27, 28]. Consequently, thanks to the relatively simple tuning methods, this material attracted considerable interest from the scientific community. Although a considerable effort has been expended to understand the nature of its physical properties, fundamental issues remain. Here, in part of this thesis, we investigated the transport properties of mm-size single crystals of Ca214 that expanded the knowledge at the basis of the electrical transport of the material (see Chapter 2). Sub-

sequently, thanks to an innovative method, we reduced the dimensionality of the crystals down to the μm range. Moreover, in the μm range we have been able to shape the geometry of the crystals with very high accuracy. This gave us the possibility to have access to unexplored physics of the Ca214 obtaining unprecedented results (see Chapter 3).

Chapter 2

Properties of Ca_2RuO_4 Induced by Current and Voltage

In this chapter, the electrical response of Ca214 single crystals is explored. The experiments had set as a function of both temperature, T, and bias-current density, J, crossing from the insulating to the metastable (MS) state, the precursor of the metallic one, where non-equilibrium processes possibly take place. Moreover, the resistivity map, $\rho(J,T)$, of the system, where ρ is the electrical resistivity, is plotted. This study, systematically performed on a large number of crystals, is a relevant starting point for further investigations. Indeed, it naturally highlights different conducting regimes, giving access to the characteristic temperatures and current densities at which they take place. In particular, here, the attention focuses on the less explored MS state since scarce information is currently available on both the conduction mechanisms and the corresponding crystallographic structure. For these reasons, the transport measurements have been combined with x-ray diffraction (XRD) spectra acquired as a function of J. Since these samples show a strong anisotropic behaviour [29] both transport and XRD measurements have been acquired in two different configurations, namely feeding the sample with the current along the c axis, and within the ab plane of the crystals. Moreover, in the configuration where the current is within the ab plane, the XRD spectra have been acquired also as a function of T.

The sections 2.1 and 2.2.1 of this chapter are based on Cirillo et al. *Phys. Rev. B*, 100(23):1–9, 2019.

Finally, we have analysed the electrical properties of Ca214 with Ru metallic inclusions.

2.1 Fabrication Method and Experimental Setup

Single crystals of Ca214 were grown by a flux feeding floating zone technique with Ru self-flux using a commercial image furnace equipped with double elliptical mirrors (see Fig. 2.1) described elsewhere [30]. A number of techniques including XRD, energy, and wavelength dispersive spectroscopy have been used to fully characterize the structure, quality, and purity of the crystals.

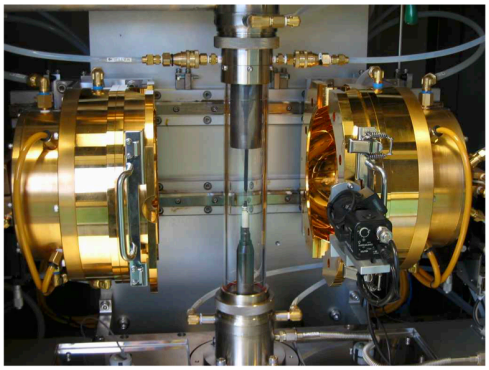

Fig. 2.1: The furnace in use at M.U.S.A. laboratory of CNR-Salerno. In particular, the image shows the double elliptical mirrors and the central rod.

The typical average dimensions of the probed crystals are about ($2.0 \times 1.0 \times 0.15$) mm. To ensure the reliability of the measurements a substantial amount of data was collected on several Ca214 single crystals, which all behaved consistently. The Ca214 has a rich phase diagram that is quite far from being fully explored and understood. Moreover, it is of relevant importance to keep under control the many experimental parameters that can influence the state of this material. Indeed, the Ca214 is very sensitive to external conditions, and consequently, the scientific research on this material is very challenging. For this reason, to efficiently study this system, precise control of the actual state of the sample, as a function of the external variables, is required. Indeed, a systematic approach is essential to obtain reproducible and scientifically sound results. In this respect, it is necessary to clarify that many different measurement protocols exist in the literature under the simple names of current or voltage drives. Therefore, the comparison of the results

obtained by different experimental procedures may be difficult.

Here, a very straightforward measurement protocol was used, namely the sample was current biased in a continuous mode, with the use of a steady current source. This approach can give access to different states of the system compared with those already reported in the literature. For instance, in the work of Bertinshaw et al., the authors first use the voltage to bias the sample, and once the switching to the metallic phase is achieved, they let an electrical current to flow in the sample [3]. Instead, in Ref. [31], voltage and current are simultaneously controlled by the use of two variable resistors.

In our work, resistivity versus temperature, for different values of the bias-current, and $V(I)$ characteristics as a function of T, were acquired. Since the crystals have high resistance values compared to the ones of the wiring and the contacts, we conducted our experiments setting the samples in a 2-probe or 4-probe configuration indifferently (see Fig. 2.2) [27, 32]. Specifically, we have fed the crystals along the c direction and within the ab plane with a Keithley 2635 SourceMeter and read the voltage drop with a Keithley 2182A Nanovoltmeter. In some specific situations, due to technical limitations, we have exploited the potential of the SourceMeter using it as a current source and voltage reader at the same time without losing any significant accuracy (see Fig. 2.2(a)). The electrical current was chosen as the biasing stimulus since it can drive the system into an intermediate phase. This phase, as demonstrated, does not have an equilibrium analog and strongly differs from the insulating or the metallic thermodynamic phases explored by the voltage-driven measurements. The accessible area of the acquired resistivity values is determined by the limit of our SourceMeter (210 V). Extreme attention was paid to adopt all the precautions necessary to maximize sample cooling and reduce contact resistance at the sample terminals. First, to keep contact resistance as low as possible, silver pads were sputtered on the crystal. Subsequently, gold wires (diameter $25\mu m$) were connected on the silver pads using an epoxy silver-based glue. Then, the crystals were thermally anchored with a small amount of cryogenic high vacuum grease on a custom-built dip probe. The sample holder consists of massive high-thermal-conductivity copper in which a *Cernox* thermometer was embedded. The temperature was controlled by lowering or lifting the probe into a cryogenic liquid nitrogen storage dewar by taking advantage of the temperature stratification naturally occurring in the vapor space above the liquid surface. In this case, the thermal stability is guaranteed by the proper design of the sample holder and

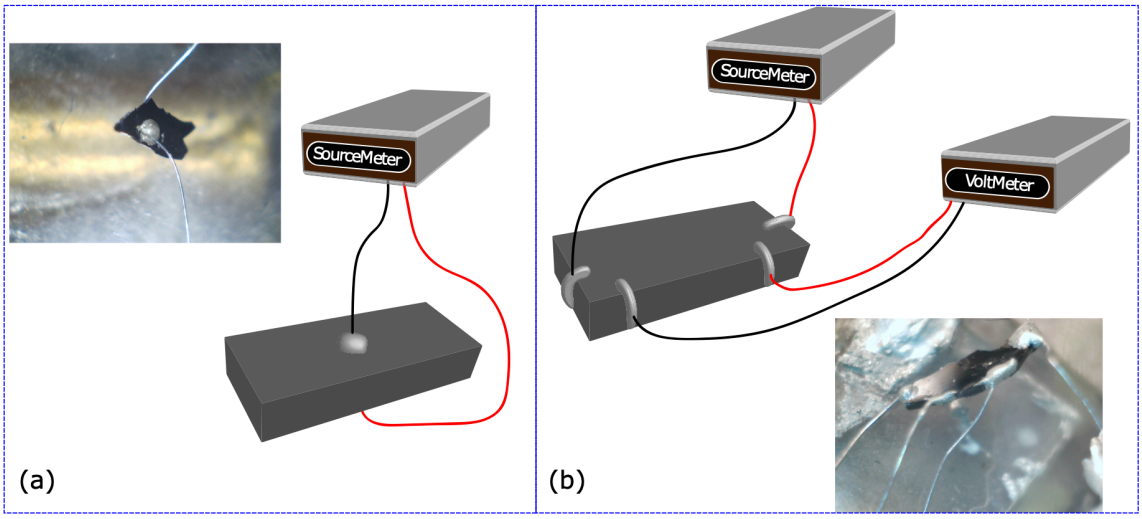

Fig. 2.2: (a) Configuration with the bias-current along the c axis in the case where the SourceMeter was used as a single instrument to source the current and read the voltage. (b) Configuration with the bias-current within the ab plane in the 4-probe configuration. Note: we remark that the Nanovoltmeter has also been used in the 2-probe configuration, namely sourcing the current with the SourceMeter and sensing the voltage with the Nanovoltmeter in both configurations (with the current along the c axis and within the ab plane).

by the extremely slow temperature sweeps.

As mentioned before, we also performed XRD measurements at room T (at different bias-current applied along the c axis of the crystal) in a specular $\omega - 2\theta$ geometry (ω is the radiation incident angle on the sample surface, while 2θ is the angle between the incident and the diffracted beam) by using a *Philips X'Pert-MRD* high-resolution analytic diffractometer (see Fig. 2.3) equipped with a four-circle cradle. A Cu $K_{\alpha 1}$ ($\lambda = 1.5406$ Å) source at 40 kV and 30 mA was employed. Measurements were carried out by using monochromatic radiation obtained by equipping the diffractometer with a four-crystal Ge 220 Bartels asymmetric monochromator and a graded parabolic Guttman mirror positioned on the primary arm. On the secondary arm, the diffracted beam reaches the detector with an angular divergence of 12 arcsec crossing a triple-axis attachment and undergoing three (002) reflections within a channel-cut Ge crystal. The XRD measurements at different T (and at different bias-current applied within the ab plane of the crystal), instead, were performed by using an automatic *Bruker D8 Advance* diffractometer (see Fig. 2.4) at 35 kV and 40 mA, using the nickel filtered Cu-K_α radiation ($\lambda = 1.5418$ Å) in

Fig. 2.3: The *Philips X'Pert-MRD* high-resolution analytic diffractometer at the M.U.S.A. laboratory CNR-Salerno. On the right, there is a zoomed image that shows the complex apparatus of this system.

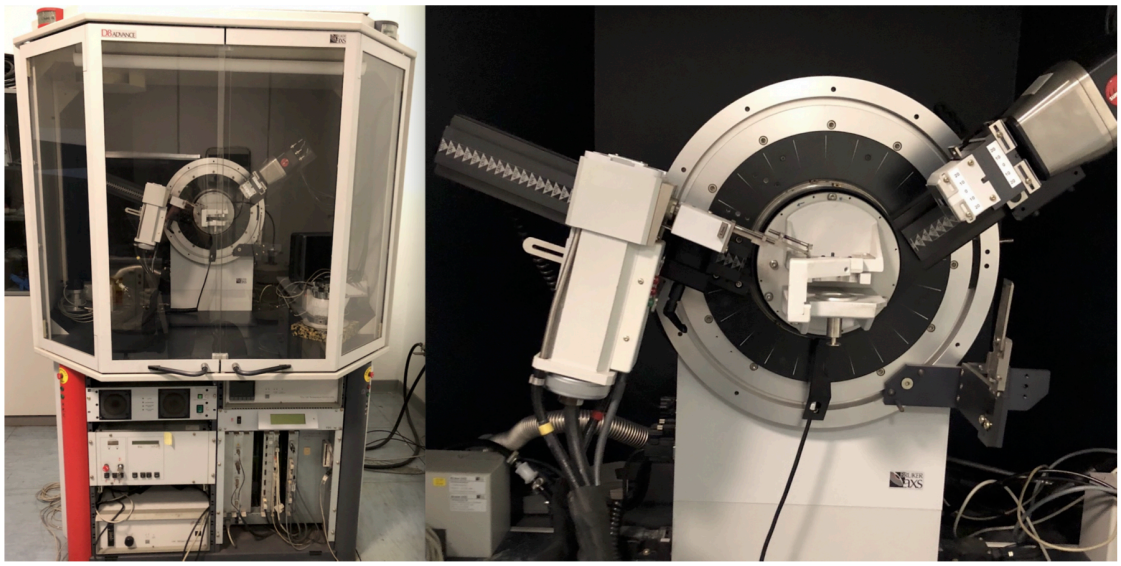

Fig. 2.4: The *Bruker D8 Advance* diffractometer at the Department of Chemistry of the University of Salerno. On the right, there is a zoomed image that shows the x-ray source (left arm), the sample holder (in the centre) and the detector (right arm). The cooling system is not shown in these pictures.

the Bragg-Brentano $\theta - 2\theta$ configuration. In this configuration, the distance from the x-ray focal spot to the sample is the same as from the sample to the detector. In this way, the reflected (diffracted) beam will stay focused on the circle of constant radius, and the detector moves on this circle. In summary, for the $\theta - 2\theta$ geometry, the x-ray tube is stationary, the sample moves by the angle θ, and the detector simultaneously moves by the angle 2θ. Moreover, this system has the possibility of lowering the temperature of the sample down to 77 K. However, the sample holder was best suited to measure our samples in the configuration with the current applied within the ab plane. Taking the advantage of this facility, we were able to acquire XRD patterns at different T and different bias-current values.

2.2 Results and Discussion

2.2.1 Configuration with the bias-current along the *c* axis

Feeding the samples with a current along the c axis (see Fig. 2.2(a)), we acquired the ρ_c (resistivity along the c axis), as a function of T and J, and $E(J)$ characteristics as a function of T. Fig. 2.5(a) shows in a semilogarithmic scale the temperature dependence of ρ_c for selected values of J. It is important to remark that on all the investigated samples, similar data were obtained. The increasing of J results in a ρ_c lowering by up to four orders of magnitude [28]. Moreover, despite ρ_c is always a decreasing function of the temperature ($d\rho_c/dT < 0$) [33], the shape of the resistivity curves evolves as J is increased. As indicated in the inset of Fig. 2.5(a), distinct $\rho_c(T)$ behaviours can be observed. The labels VRH, SE, and MS, stand for variable range hopping, semiconducting, and metastable, respectively, that will be discussed more in detail later. Additionally, looking at the $\rho_c(T)$ curves in the semilogarithmic scale, it is immediately evident that there is a critical value $J_{sep} \approx 0.4$ mA/cm^2, which sets the change in the concavity of the $\rho_c(T)$ curves in agreement with the literature. The curves acquired for $J < J_{sep}$ slightly depend on the value of J, as for the ones at $J = 0.2$ and 0.4 mA/cm^2, which entirely overlap [28]. By measuring ρ_c, lowering and increasing T, an irreversible behaviour, never reported in the literature, was observed. There are parts of the $\rho_c(T)$ curves whose accessibility depends on the sample history, as shown, for example, for $J = 22$ and 440 mA/cm^2. Here the continuous lines indicate the data obtained by lowering T. For $J < J_{sep}$, the resistance surge beyond the measurable range of our experimental setup at a characteristic temperature, $T_{irr} \approx 130$ K, while for $J > J_{sep}$, the resistance is still measurable below this value. However, by increasing the temperature from the lowest T reached in the experiment, a measurable ρ_c is detected only for $T > T_{irr}$ (black dotted lines). The values of T_{irr} are represented as blue triangles in Fig. 2.5(a). Curiously, for all the analyzed crystals and independently on J, $T_{irr} \approx 130$ K, a value comparable with T_{AFM}. Contrary to what reported in the literature, the measure of $\rho_c(T)$ can give information on the magnetic ordering temperature in Ca214 [33]. Furthermore, this result confirms that J induces a more conductive MS state where AFM is suppressed [3]. More generally, J can be used to control the magnetic ordering of this class of materials [3,32]. However, a detailed analysis of this result is beyond the scope of this work and will be the subject of future studies.

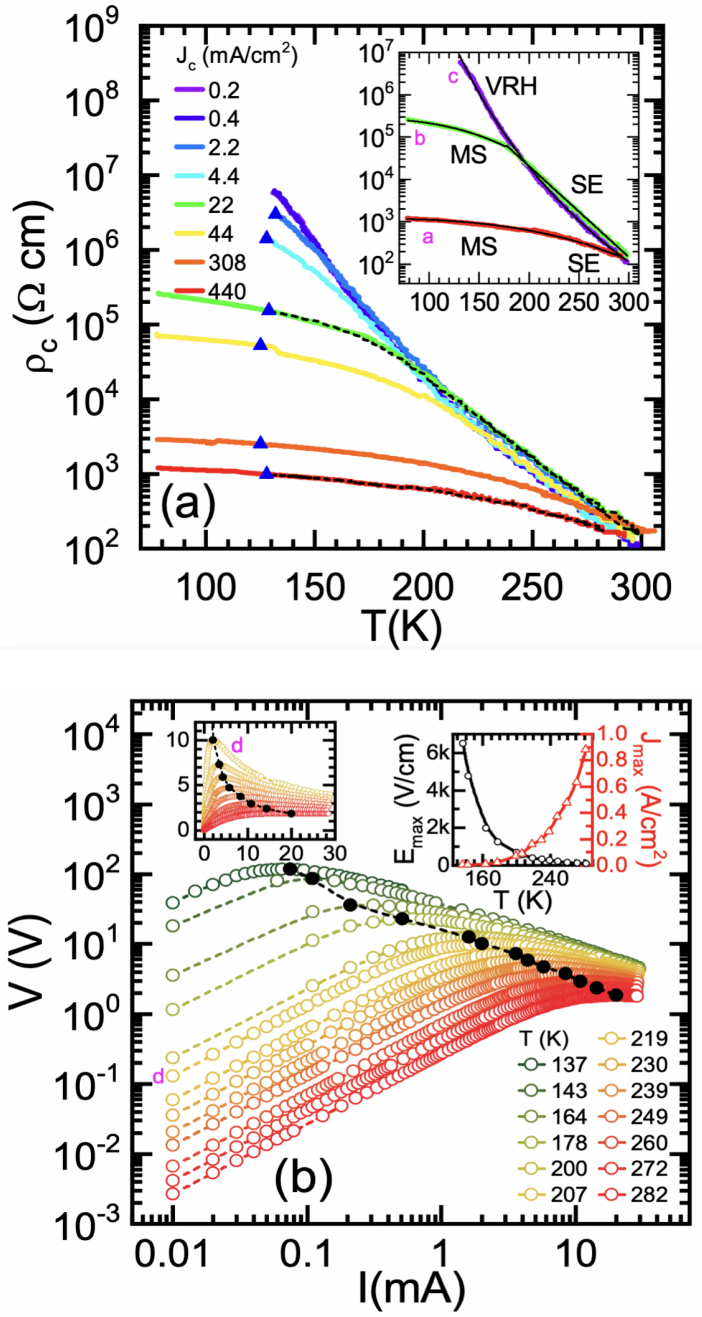

Fig. 2.5: (a) Resistivity versus temperature of Ca214 single crystal. The $\rho_c(T)$ curves for $J = 22$ (green) and 440 (red) mA/cm^2 measured by first decreasing T (continuous lines) and then heating the sample (dashed lines) are highlighted. Inset: selection of $\rho_c(T)$ curves (labeled as a, b, c) plotted together with the different conduction regimes (VRH, SE, and MS). (b) $V(I)$ as a function of T. A representative curve is labeled by the letter d. The black solid circles connect the maximum of all the curves, (V_{max}, I_{max}), as also shown on linear scales (left inset). Right inset: temperature dependence of E_{max} (left scale) and J_{max} (right scale).

In Fig. 2.5(b), a selection of $V(I)$ characteristics, plotted on a double logarithmic scale, is shown. A negative differential resistance can be observed beyond the low J regime when the samples show an evident insulating behaviour [31, 34]. This is consistent with the dramatic reduction of resistivity observed in the $\rho_c(T)$ curves by increasing J. The change in the conduction results in a maximum in the characteristics at (V_{max}, I_{max}) [or equivalently at (E_{max}, J_{max})], as highlighted in the left inset of Fig. 2.5(b) by black solid circles, where the curves on a linear scale are displayed. By further increasing the current, an ohmic dependence, signature of the IMT, is expected [27]. However, we carefully avoid exceeding this threshold to preserve the crystal integrity and acquire the whole resistivity map. At room temperature, $E_{max} \approx 100$ V/cm and $J_{max} \approx 0.9$ A/cm^2. In the right inset of Fig. 2.5(b), their temperature dependence is reported. While E_{max} (black points, left scale) rises with T [27], J_{max} (red points, right scale) decreases on cooling. This last behaviour is counterintuitive and requires further investigation to be understood. It is worth noting that E_{max} should not be confused with E_{th}. Clearly, E_{th} is the value at which one reaches the metallic phase [27], while E_{max} is the value to reach the MS state.

In order to draw the $\rho_c(J,T)$ contour plot of the crystal resistivity shown in Fig. 2.6, we combined both $\rho_c(T)$ curves acquired at different value of J, and $E(J)$ characteristics as a function of T. For ease of reference, only a selection of $\rho_c(T)$ curves, representative of different conduction behaviours, are reported in Fig. 2.6 as vertical lines (*a, b, c*). The same $V(I)$ curve labelled as *d* in Fig. 2.5(b) is represented as a horizontal line (see Fig. 2.6). The $\rho_c(J,T)$ phase diagram covers different regions corresponding to different conducting regimes (UR, VRH, SE, MS, and AFM), identified by the three contours in Fig. 2.6. The dot-dashed vertical line denotes the value of J_{sep}. The positions of the maximum of the $V(I)$ curves at the investigated temperature are represented by black dashes (as in Fig. 2.5(b)). Finally, the blue dotted line at $T_{irr} \approx 130$ K shows the nonreversible behaviour of the $\rho_c(T)$ curves, specifically, the onset of the AFM order. Consequently, we can identify the following conducting regimes. The limit of both low J and T is the so-called unexplored region (UR). Precisely, it is a deep insulating part that is not accessible due to the limit of our experimental setup. Moreover, scrolling along the J axis ($J < J_{sep}$, all T), the $\rho_c(T)$ has a variable range hopping behaviour. Here the resistivity is not influenced by the bias-current. Passing through the dot-dashed line, where $J > J_{sep}$, a decrease of $\rho_c(T)$ is

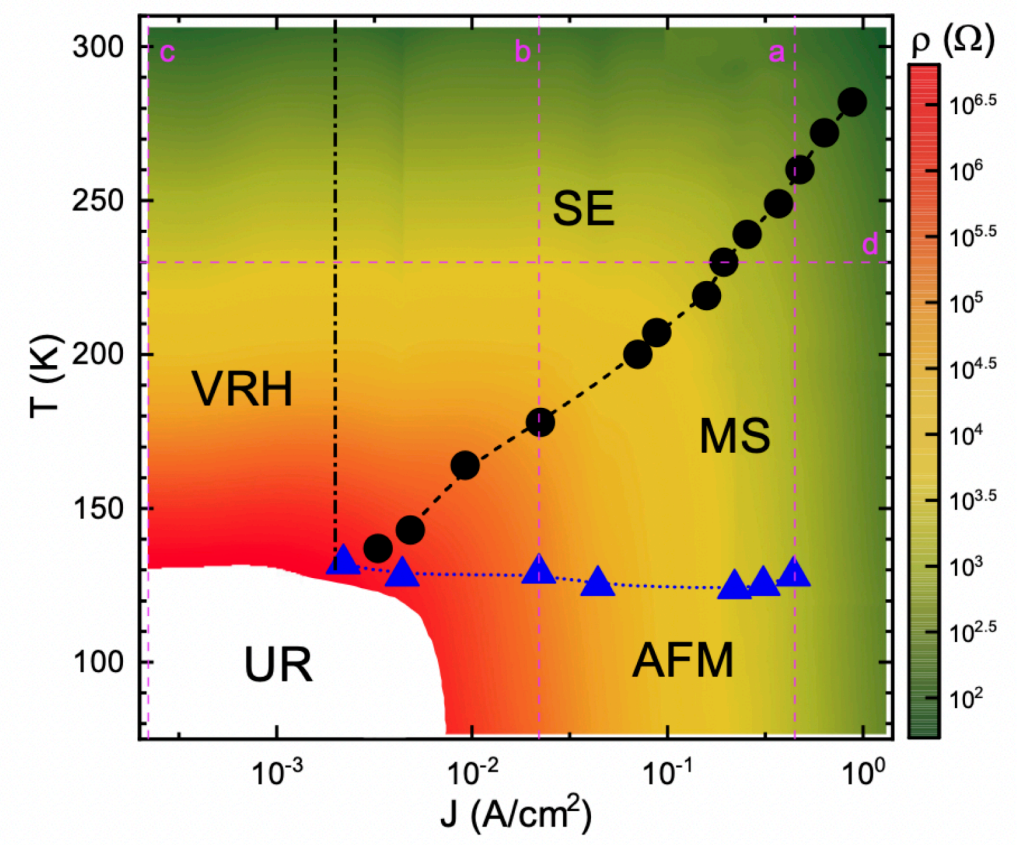

Fig. 2.6: $\rho_c(J,T)$ contour plot of the crystal obtained by combining the $\rho_c(T)$ and the $V(I)$ curves. The $\rho_c(T)[V(I)]$ curves labeled by the letters a, b, and c [d] in Fig. 2.5(a) [2.5(b)] are reported here. The different regions that correspond to the conduction regimes UR, VRH, SE, MS, and AFM are highlighted. The blue triangles (black circles) are the same of Fig. 2.5(a) [2.5(b)].

observed [28]. On this side, the regions labelled as SE and MS, separated by the black dashed line, define the semiconducting and the metastable regimes. The SE regime, ($J_{max} > J > J_{sep}$ and $T > T_{max}$), resembles the one of an intrinsic semiconductor at sufficiently high T, while the MS regime, ($J > J_{max}$ and $T < T_{max}$), is characterized by a $\rho_c(T)$ that has a behaviour very different from both an insulator (decreasing, positive concavity in both linear and log scale) and metal (increasing, positive concavity in both linear and log scale). However, a decreasing behaviour with a negative (positive) concavity in the log (linear) scale, is observed. Furthermore, this change of concavity in the log scale allows us to identify J_{sep}. Such a situation, still interpreted in the VRH model, denotes the divergence of the localization length. We interpreted this as the sign that at least a part of the sample becomes conducting,

leading to a resistivity that strongly matches those of alloys. However, the specific nature of the conducting mechanism needs to be further clarified in this case.

To have access to the microscopic properties of the crystals at the different conduction regimes, we combined XRD and electronic measurements. Specifically, we acquired the XRD patterns while passing the current along the c axis of the crystal at room temperature. The experimental configuration can be schematically seen in Fig. 2.7. Panel (a) of Fig. 2.8 shows the

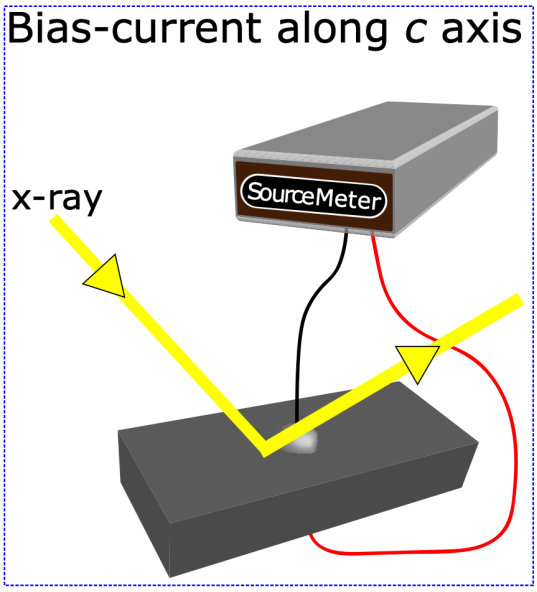

Fig. 2.7: Schematic configuration of the experiment. Using the SourceMeter, the bias-current was applied along the c axis of the crystal, and the corresponding voltage drop was sensed at the same time. For each bias-current value applied to the sample, an XRD pattern was acquired.

dependence of the c-lattice parameter (left scale) on the normalized current density, J/J_{max}. In the same graph, we have also plotted the normalized $E(J)$ characteristic (right scale), and reported the specific level arrangements (I-SC, M$'$, M-long, see below). The position of (006) reflection of the XRD $\omega - 2\theta$ scans is employed to estimate the values of the c axis by using the Bragg law. These values, indicated by black-closed circles, represent the elongation of the short c axis of the insulating S phase (at $J = 0$ $c = 11.914$ Å, we have used a magenta closed circle) [27]. This elongation originates a distortion of the lattice cell, which now is labelled as S'. Following the trend of the c axis elongation, at $J \approx J_{max}$, a new phase indicated as L' and denoted by open circles, clearly appears. Curiously, by increasing J, the c axis of

this L' phase also elongates in the whole examined current range, that covers the region of negative differential resistance of the $E(J)$ curve. Subsequently, at $J/J_{max} \approx 3.7$, the diffraction peak correlated with the metallic L phase appears ($c = 12.264$ Å, black triangle) [27]. These data prove that in the MS state, a new, possibly metallic L' crystallographic phase coexists with the short insulating one S' in a quite broad range of current values and even with the metallic one L, at the maximum current reached in the experiment. Considering the reflections (208) and (028) we computed the lattice parameters a and b. In Fig. 2.8(b) the dependence on J/J_{max} of a and b is compared with the c axis. Remarkably, the value of the b axis (red dots) splits into two parts at $J/J_{max} \approx 1$, as the value of the a axis (blue dots) is relatively constant instead. Moreover, in the same region, the b axis data show statistical scattering, probably due to the release of the in-plane strain in the crystal while the S' and L' phases coexist and compete with each other. It is noteworthy that in terms of the crystallographic axis, the L' phase moves toward a metallic tetragonal structure, while the S' phase gradually relaxes back toward the S one. Indeed, once the L' phase nucleates and expands, S transport only a modest fraction of the flowing current. Finally, we want to point out that the values of the lattice parameters, both in the S and in the L phases, are consistent with the results reported in the literature [21,27,35]. Particularly, the value of the c axis in the metallic phase is in accordance with the ones reported for structural transitions induced by the electric field, pressure, and temperature [27]. This shows that, contrary to the MS state, L is a proper thermodynamic phase.

The negative differential resistivity of the MS state and the counterintuitive increase of J_{max} with T could be explained by the appearance of the metallic phase L' in the crystal. Indeed, to maintain a systematic increment of current flow in an overall insulating state at a determined critical $J(T)$ comparable with $J_{max}(T)$, the system finds it energetically more convenient to nucleate a more conductive crystallographic phase, L'. As a consequence, over $J_{max}(T)$, the electrical potential required to further increase the current flow diminishes, and the more-conductive L' phase grows. Furthermore, on increasing T, the S' phase itself can transport more current, since it becomes less insulating. Therefore, $J_{max}(T)$ is an increasing function of T. This is just one of the clearest signatures that the emergence of L' is not a classical effect driven by Joule heating, but that it comes from a much more subtle and complex energy balance.

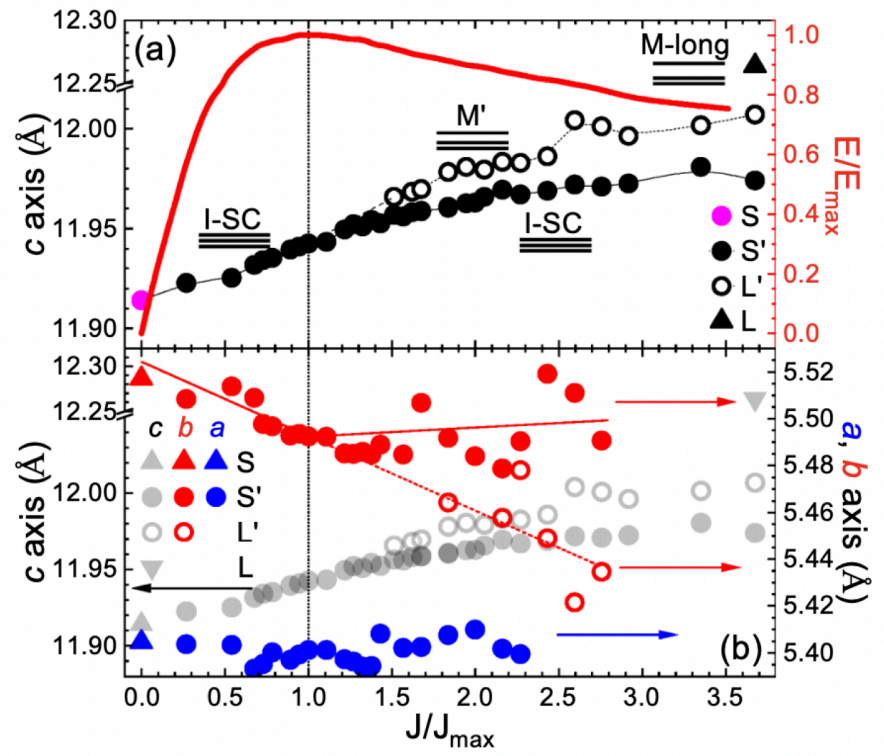

Fig. 2.8: (a) Left scale: dependence of the $c-$lattice parameter corresponding to the different crystallographic phases (S, S', L', and L) as a function of J/J_{max}. Right scale: normalized $V(I)$ curve ($E/E_{max} - J/J_{max}$) acquired on the same crystal. (b) On the left (right) scale, the dependence of the $c-$ ($a-$, $b-$) lattice parameter as a function of J/J_{max} is plotted. The error bars are smaller than the data symbols. Lines are guides to the eyes.

To provide further evidence of the coexistence of the three distinct crystallographic phases in the current-induced MS state, additional XRD data for another single crystal are displayed in Fig. 2.9. Here the values of the c-lattice parameters as a function of the normalized electrical current density were derived from the (002) reflection. Again the comparison with the normalized $E(J)$ curve measured for the same crystal (right scale) confirms that the S' phase splits into the L' phase at $J \approx J_{max} = 0.8$ A/cm^2 (see vertical dashed line).

This phase is well distinguished in all the investigated current ranges from the other two diffraction peaks, as shown in Fig. 2.10, where three representative $\omega - 2\theta$ scans of the (002) reflection are reported for different values of J/J_{max}, corresponding to different regions of the $E/E_{max} - J/J_{max}$ characteristic. It is evident that before reaching the maximum of the $E/E_{max} - J/J_{max}$ characteristic, namely, in the insulating regime, only the peaks identifying

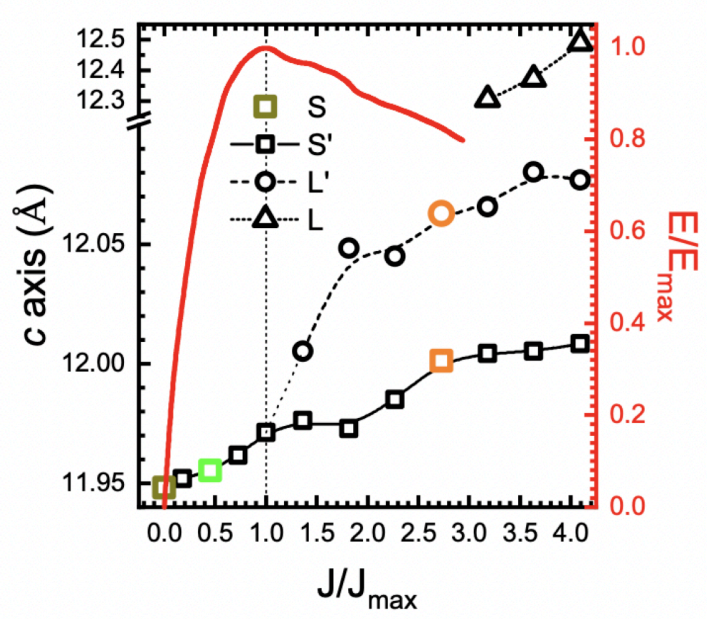

Fig. 2.9: Left scale: dependence of the $c-$lattice parameter at room T as a function of J/J_{max}. The bigger coloured points indicate the values of the c axis extracted from the XRD scans of the corresponding colour reported in Fig. 2.5(a). Right scale: normalized $V(I)$ curve ($E/E_{max} - J/J_{max}$) measured at room T on the same sample.

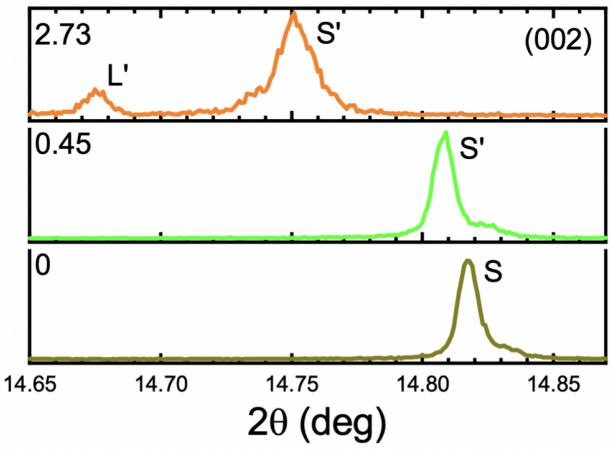

Fig. 2.10: Representative $\omega - 2\theta$ scans of the (002) reflections at different values of J/J_{max} for the same sample of Fig. 2.9. The labels on the diffraction peaks correspond to the different crystallographic phases (S, S', L') at different conduction regimes.

the phases S and S' are present (dark yellow and green scans, respectively). Above J_{max}, the diffraction peak of the L' phase develops, as shown by the orange line, acquired at $J/J_{max} = 2.73$.

2.2.2 Configuration with the bias-current within the *ab* plane

Feeding the samples with a current within the ab plane of the crystals, and using the same experimental setup, but changing the configuration of the sample as shown in Fig. 2.2(b), we acquired, in this case, the resistivity within the ab plane, ρ_{ab}, as a function of T and J, and $E(J)$ characteristics as a function of T. Fig. 2.11(a) shows the temperature dependence of ρ_{ab} for selected values of J in a semilogarithmic scale. The results are qualitatively the same observed with the bias-current along the c axis. Indeed, the increase of J still results in a ρ_{ab} lowering. However, in this configuration, the sample appears less resistive. In fact, comparing $\rho_{ab}(T)$, and $\rho_c(T)$, acquired with roughly the same J, it is immediately clear that $\rho_{ab}(T)$ is about three order of magnitude less resistive than $\rho_c(T)$. Moreover, ρ_{ab} keeps its behaviour of a decreasing function of the temperature, albeit the shape of the resistivity curves evolves with J increasing. In this configuration the value which sets the change in the concavity of the $\rho_{ab}(T)$ curves is $J_{sep} \approx 0.2$ A/cm^2 (for $J < J_{sep}$, $\rho_{ab}(T)$ curves slightly depend on the value of J). As found before also here there is the characteristic temperature T_{irr} but in this case is ≈ 160 K. The values of T_{irr} are represented as blue triangles in Fig. 2.11(a). In Fig. 2.11(b), a selection of $E(J)$ characteristics, plotted on a double logarithmic scale, is shown. A negative differential resistance, in this case, can be still observed beyond the low J regime when the sample shows an evident insulating behaviour. This is consistent with the dramatic reduction of resistivity observed in the $\rho_{ab}(T)$ curves by increasing J. The change in the conduction results in a maximum in the characteristics at (E_{max}, J_{max}), as highlighted in the left inset of Fig. 2.11(b) by black solid circles, where the curves on a linear scale are displayed. By further increasing the current, an ohmic dependence, signature of the IMT, is expected. However, again, we carefully avoid exceeding this threshold to preserve the sample integrity. At room temperature, $E_{max} \approx 30$ V/cm (a value lower than the one measured in the c axis configuration) and $J_{max} \approx 1.3$ A/cm^2 (a value slightly bigger than the one measured in the c axis configuration). In the right inset of Fig. 2.11(b), their temperature dependence is reported. As in the case of the c axis configuration, while E_{max} (black points, left scale) rises with T, J_{max} (red points, right scale) decreases on cooling, albeit with different values. However, these measurements show that the ab plane, although is more resistive than the c axis, has qualitatively the same behaviour found in the c axis.

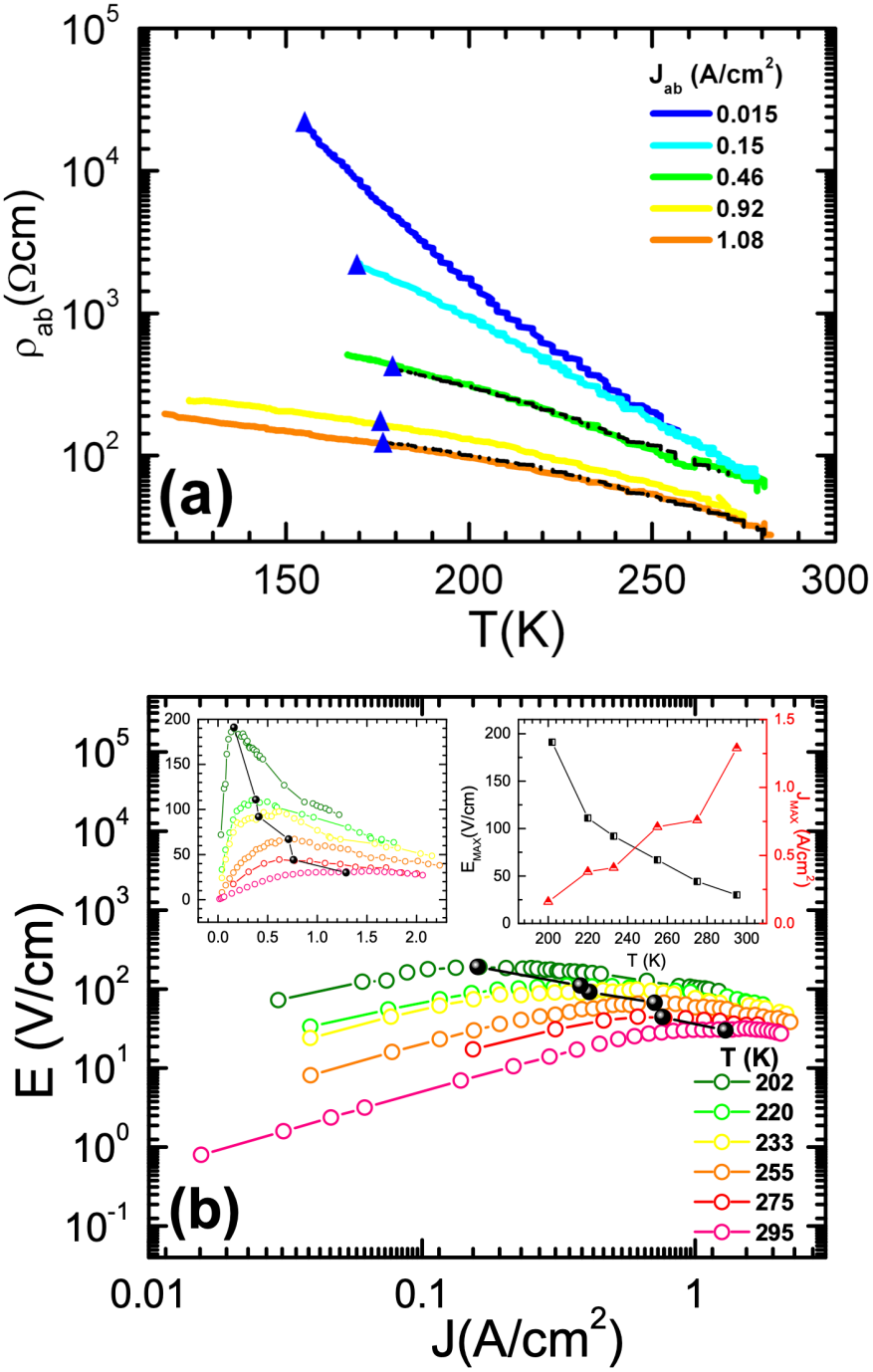

Fig. 2.11: (a) Resistivity versus temperature of Ca214 single crystal. The $\rho_{ab}(T)$ curves for $J = 0.46$ (green) and 1.08 (red) A/cm^2 measured by first decreasing T (continuous lines) and then heating the sample (dashed lines) are highlighted. (b) $E(J)$ as a function of T. The black solid circles connect the maximum of all the curves, (E_{max}, J_{max}), as also shown on linear scales (left inset). Right inset: temperature dependence of E_{max} (left scale) and J_{max} (right scale).

To have access to the microscopic properties of the crystals at the different conduction regimes, also in this configuration, we combined XRD and electronic measurements. Specifically, we acquired the XRD patterns while passing the current within the *ab* plane of the sample, but this time at different T (by using the *Bruker D8 Advance* diffractometer see Fig. 2.4). The experimental configuration can be schematically seen in Fig. 2.12.

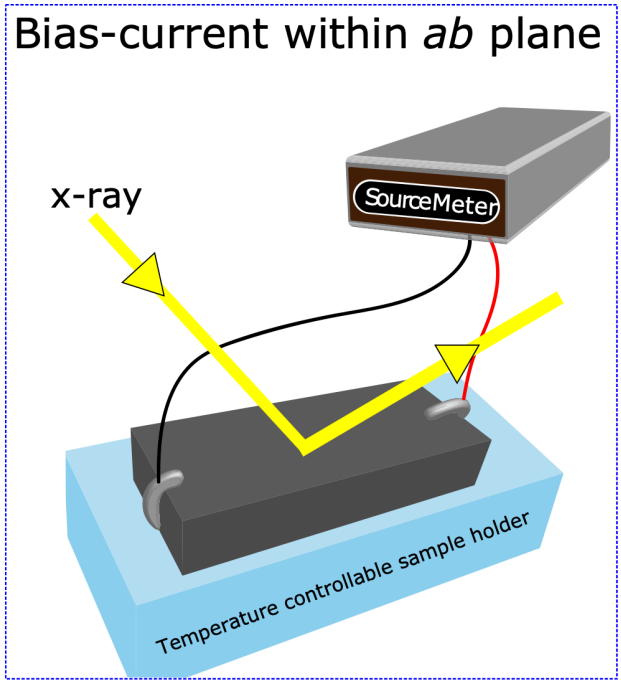

Fig. 2.12: Schematic configuration of the experiment. Using the SourceMeter, the bias-current was applied within the *ab* plane of the crystal, and the corresponding voltage drop was sensed at the same time. For each temperature and bias-current value applied to the sample, an XRD pattern was acquired.

All the diffraction peaks of the XRD spectra can be identified with the expected $(00l)$ Bragg reflections coming from Ca214 oriented with c axis perpendicular to the surface of the sample. The data were collected by step-scanning in the angle range of $10° \leq 2\theta \leq 65°$ at step size of $0.02°$. In this case, the c axis values have been calculated considering the (002), (004), (006), and (008) reflections. A representative spectrum, acquired at $T = 198$ K and $J = 2.65$ A/cm^2 is reported in Fig. 2.13.

Fig. 2.14(a) shows the dependence of the c-lattice parameter versus J at different T, while in Fig. 2.14(b) the corresponding $E(J)$ curves at the same T are reported for reference. The data show qualitatively the same behaviour

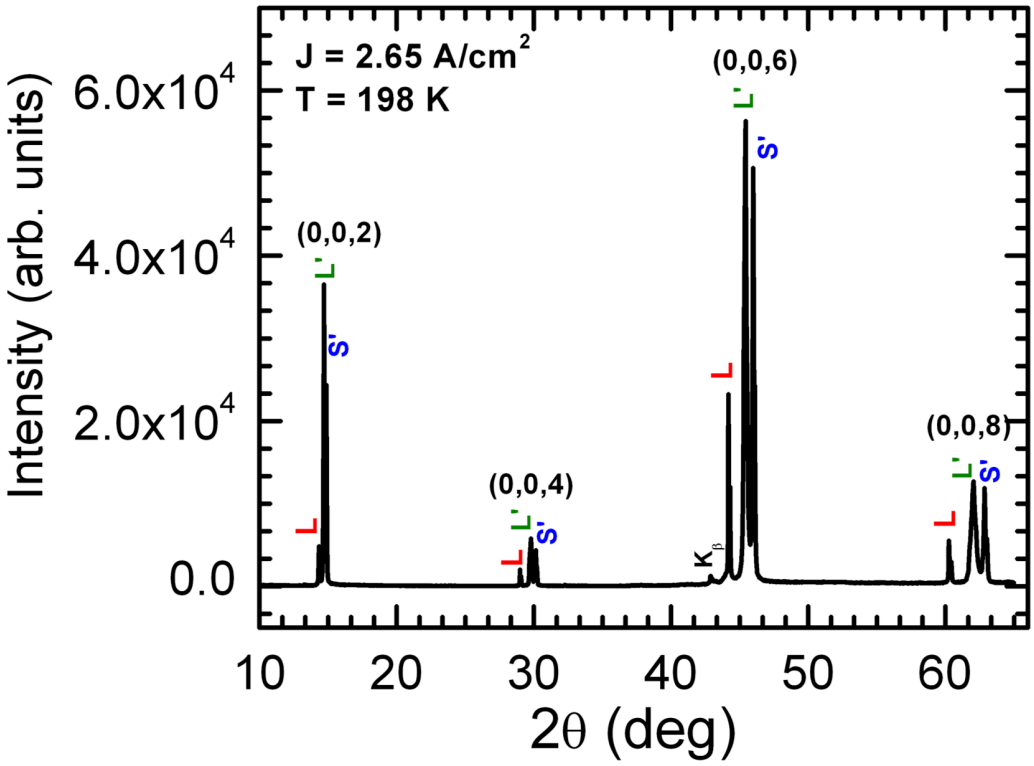

Fig. 2.13: Representative $\theta - 2\theta$ spectrum acquired at $T = 198$ K, and $J = 2.65$ A/cm^2. The labels on the diffraction peaks correspond to the different crystallographic phases (S', L', L).

we found in the c axis configuration (see Fig. 2.8). Indeed, the Fig. 2.14(a) shows that all the phases (S, S', L', L) are still present at low T, albeit, at $T = 170$ K the metallic L peak phase have not been observed since, to preserve the sample integrity, we have not continued to increase the bias-current density. Moreover, the value of the c axis in the metallic phase (L) does not change with temperature and current. In particular, it remains the same value found at room temperature ($c \approx 12.26$ Å [3, 27]) independently of the configuration used to measure the sample. This is a further evidence that, contrary to S, S', and the MS state (L' phase), L is a structurally rigid phase from the elastic point of view.

In fact, as shown in Fig. 2.14(a), the other phases depend also on temperature. In particular at $J = 0$ A/cm^2 the c axis values of the S phase (light grey solid symbols) decrease with the temperature lowering as shown in Fig. 2.15, and in accordance with Alexander et al. [35].

In Fig. 2.16 are reported the spectra of the (004) reflection, acquired at $T = 255$ K at different bias-current densities. These three representative $\theta - 2\theta$

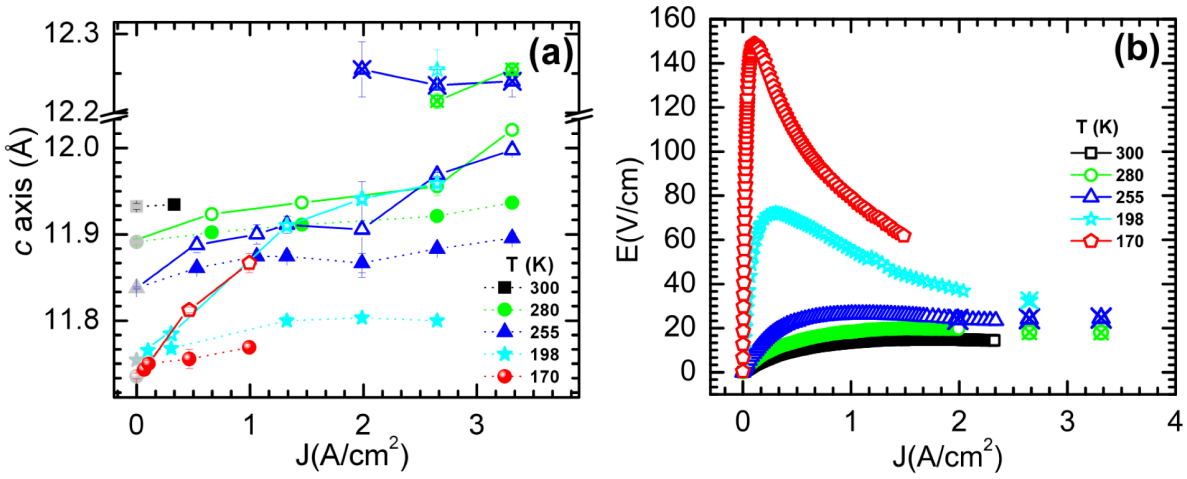

Fig. 2.14: (a) Dependence of the c lattice parameter corresponding to the different crystallographic phases (S, S', L', and L) as a function of J and T. The solid symbols are the S' phases, the open ones are the L' phases, the cross marked symbols are the L phases and the light grey solid symbols are the S phases (the phase at $J = 0$ A/cm^2). The lines are guides to the eyes. (b) $E(J)$ curves acquired at the same temperature of panel (a) on the same crystal. Here, the points where the metallic L phase appear are also reported with the same symbols used in panel (a).

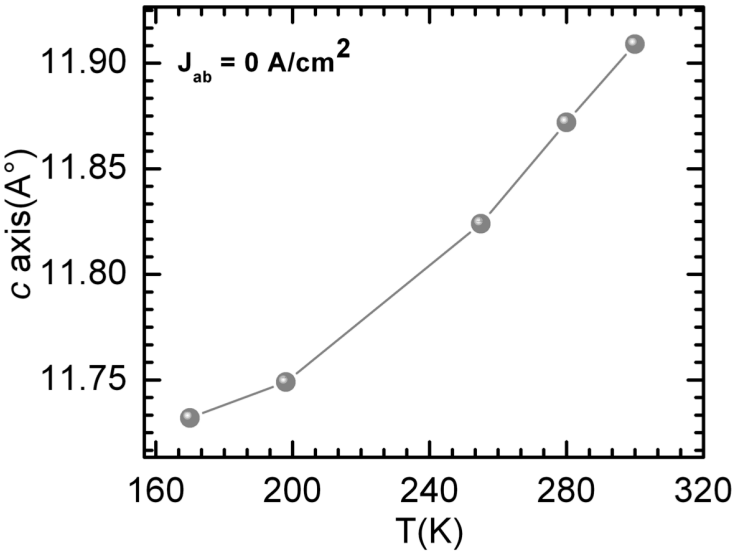

Fig. 2.15: c axis evolution as a function of the temperature at $J = 0$ A/cm^2 (S phase). Lines are guides to the eyes.

scans highlight that all the phases are well distinguished also at temperatures lower than the room one. It possible to observe that while the bias-current density is increased the peaks of the S' and L' phases shift to lower 2θ values,

indicating the increasing of the c axis. Lastly, at $J = 1.99$ A/cm^2 the L phase peak emerges. To extract information from the spectral data, the curve fitting (black lines in Fig. 2.16) with Lorentzian function has been used[1] [36]. Finally, we point out that this analysis is a valuable starting point to get the

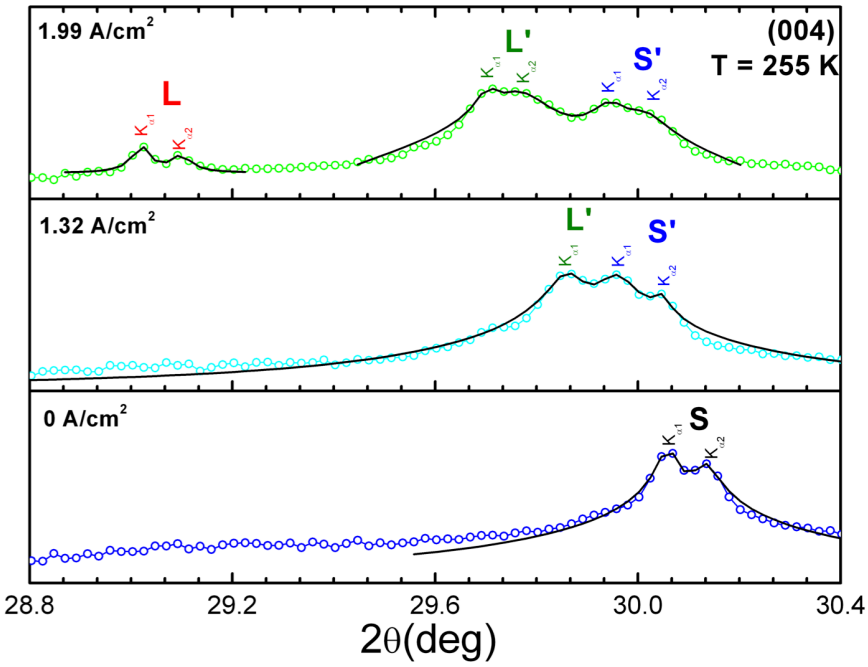

Fig. 2.16: Representative $\theta - 2\theta$ scans of the (004) reflections at $T = 255$ K, and at different values of J for the same sample of Fig. 2.14. The labels on the diffraction peaks correspond to the different crystallographic phases (S, S', L', L) at different conduction regimes. The black lines are the best fits to the spectra obtained by using a Lorentzian function.

c axis phase diagram that would allow distinguishing the conduction states as a function of temperature and current density in Ca214 single crystals. Moreover, these data show that the MS phase (L') is present also in this configuration within the temperature range we explored. For this reason, one should be very careful to identify in which region of the phase diagram the crystal is when studying the Ca214 physical properties. In particular, to investigate the electronic properties of Ca214 in a pristine state (e.g. avoid any complications arising from non-equilibrium conditions), the crystal should be kept far from the MS state that is below the J_{max} (or E_{max}). Indeed, in Chapter 3, we have conducted our experiments maintaining the samples in the S and S' phase but never reaching J_{max}.

[1]We are grateful to Dr V. Granata for this analysis.

2.3 Ca_2RuO_4 with Metallic Ru Inclusions

It has been proved that chemical engineering is an effective way of exploring or inducing new properties in Ca214. Indeed, a prominent example is the $Ca_{1-x}Sr_xRuO_4$ where the physical properties strongly depend on the composition [22,37]. Generally speaking, the synthesis of an appropriate composite can also offer an interesting opportunity to improve the physical properties of the starting material. As an example, it has been found that in a composite system formed by Ru metal embedded in the primary phase of Sr214 the critical temperature, T_c, raised up to 3 K, which is twice that reported for the best quality of Sr214 single crystals [38]. For these reasons, Ca214 is a good playground to test if intriguing physical properties may be observed in a composite made by Ca214 and Ru metal inclusions. A question naturally arises whether it is possible to tune the metallicity in Ca214 solidifying Ru inclusions in single crystals of Ca214. Similar to what has been done in the case of Sr214-Ru (Sr214 with embedded metallic Ru), the synthesis of an eutectic like a composite of Ca214-Ru (Ca214 with embedded metallic Ru) could be prepared controlling the solidification of an appropriate liquid, and for this purpose, the floating zone method is the most effective. Indeed, as previously discussed, this growth technique is a powerful tool for controlling the crystallization of many materials and therefore to get high-quality single crystals. Moreover, by changing the synthesis conditions and the initial composition it is possible to grow polyphasic systems formed by a crystalline matrix embedding a secondary phase [39,40]. Therefore, samples of Ca214-Ru were grown for the first time at M.U.S.A. laboratory of CNR-Salerno, by using the flux feeding floating zone technique described in Ref. [41]. To confirm the presence of metallic Ru in the Ca214 matrix, scanning electron microscope (SEM) and XRD measurements have been performed. In Fig. 2.17 an SEM image of the Ca214-Ru sample is shown. This image has been acquired on a polished surface parallel to the *ab* plane of the crystal. The small bright particles are the Ru inclusions enclosed in the Ca214 matrix as confirmed by energy dispersive spectroscopic analysis, while the composition of the main dark area is in agreement with stoichiometric Ca_2RuO_4 [41]. Moreover, a further confirmation of Ru inclusions has been obtained by acquiring, on a cleaved surface of the sample, an XRD spectrum that in Fig. 2.18 is shown. The expected $(00l)$ Bragg reflections coming from Ca214 are present, as well as the peaks related to the Ru inclusions. These latter are emphasized in a zoomed image

in the inset of Fig. 2.18. Furthermore, to get insight into this new system from the electrical point of view, the transport properties should be analysed. Indeed, in this preliminary study, we describe the electrical characterisation of Ca214-Ru. In particular, we acquired the resistivity as a function of the temperature at different J, $E(J)$ and $J(E)$ characteristics, namely, for these last, the sample has been measured using a current-bias and a voltage-bias correspondently. The typical average dimensions of the probed crystals are about $(1.8 \times 0.6 \times 0.5)$ mm.

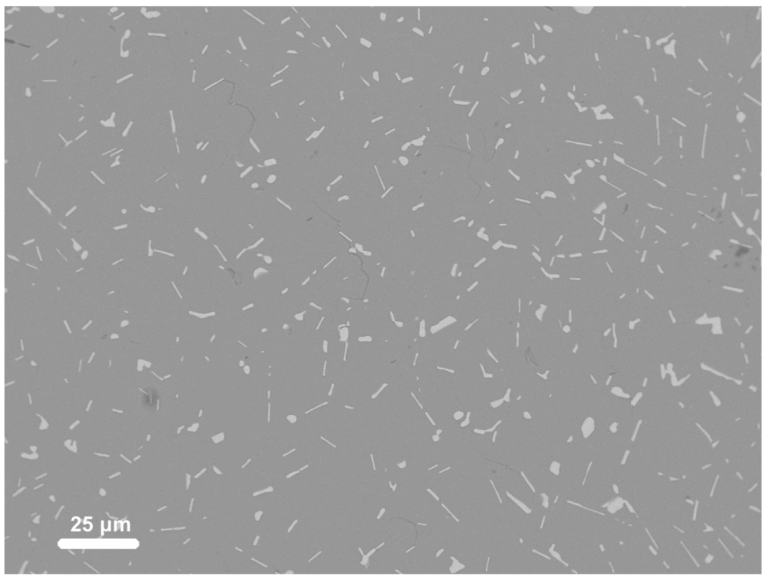

Fig. 2.17: SEM image of the Ca214-Ru. The white domains are the metallic Ru inclusions, while the main dark area is the stoichiometric Ca_2RuO_4 matrix.

Feeding the sample with a current within the ab plane of the crystal (see the setup in Fig. 2.2), we acquired the resistivity within the ab plane, ρ_{ab}, as a function of T at different values of J. At first glance, the results, shown in Fig. 2.19 in a semilogarithmic scale, confirm that the behaviour of $\rho_{ab}(T)$ curves is qualitatively the same observed in the ab plane of Ca214 (see Fig. 2.11). However, from a careful analysis emerges that in the case of Ca214-Ru the sample is less resistive than Ca214 in accordance with Granata et al. [41]. In fact, the light grey curve in Fig. 2.19, that is the $\rho_{ab}(T)$ of Ca214 acquired with $J = 0.46$ A/cm^2, highlights the increased metallicity of Ca214-Ru. On the other hand, it is quite intuitive that the presence of metallic Ru in the matrix of Ca214 can increase the metallicity of the system, but, as we pointed out before, it is not obvious that this new system preserves

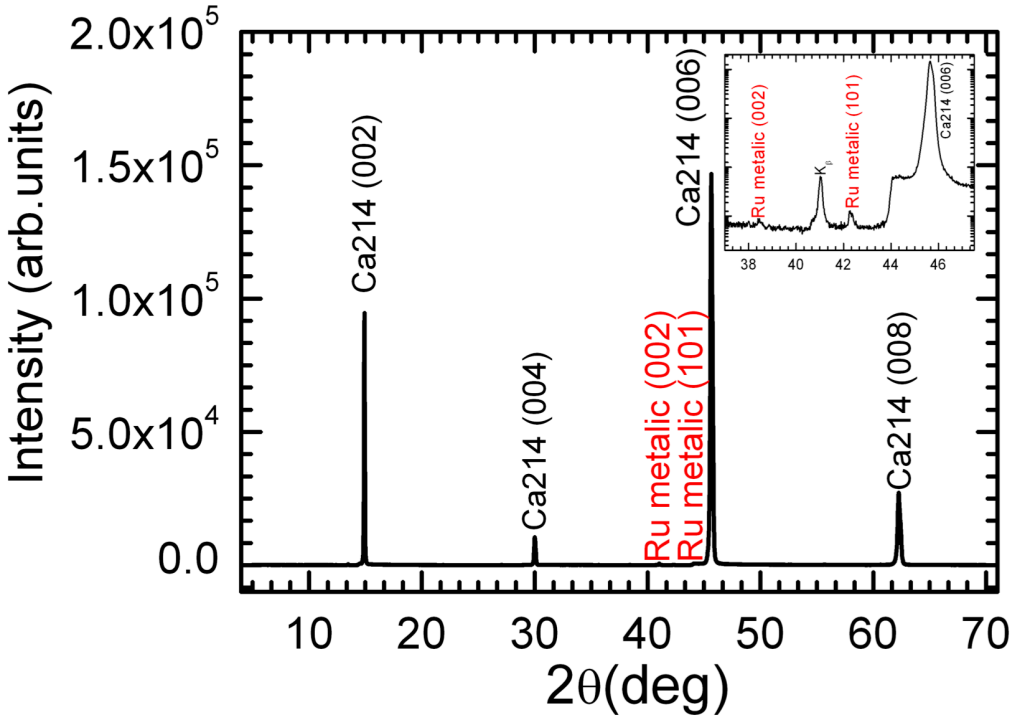

Fig. 2.18: XRD spectrum of the Ca214-Ru. The peaks related to the Ca214 and the metallic Ru inclusions are present and well distinguished. The inset is a zoomed image of the Ru peaks zone.

all the electric properties of the pure Ca214. Indeed, here, the characteristic temperature T_{irr} has the same value found for Ca214 ($\approx$ 160 K), represented as blue triangles in Fig. 2.19. Moreover, the value of J_{sep} which sets the change in the concavity of the $\rho_{ab}(T)$ curves is between 0.03 and 0.3 A/cm^2 (remembering that for $J < J_{sep}$, $\rho_{ab}(T)$ curves slightly depend on the value of J).

The panel (a) of Fig. 2.20 shows the $J(E)$ measured in the configuration with the voltage-bias (E field) applied within the ab plane, while the panel (b) displays the $E(J)$ acquired in a second run on the same sample, but using a current-bias within the ab plane. The first, very surprising effect we observed is that, albeit the behaviour of the curves is qualitatively the same observed in Ca214, this time, the sample does not break as in the case of pure Ca214 [27]. This effect is also observed in other similar systems, such as Ca214 doped with 1% of Ti [42]. However, in Ca214-Ru samples, we do not provide doping to the material in the real sense but add a metallic Ru substructure to the Ca214 matrix. This substructure possibly reduces the strain in the material since there is a scarce mismatch between the metallic Ru and the Ca214

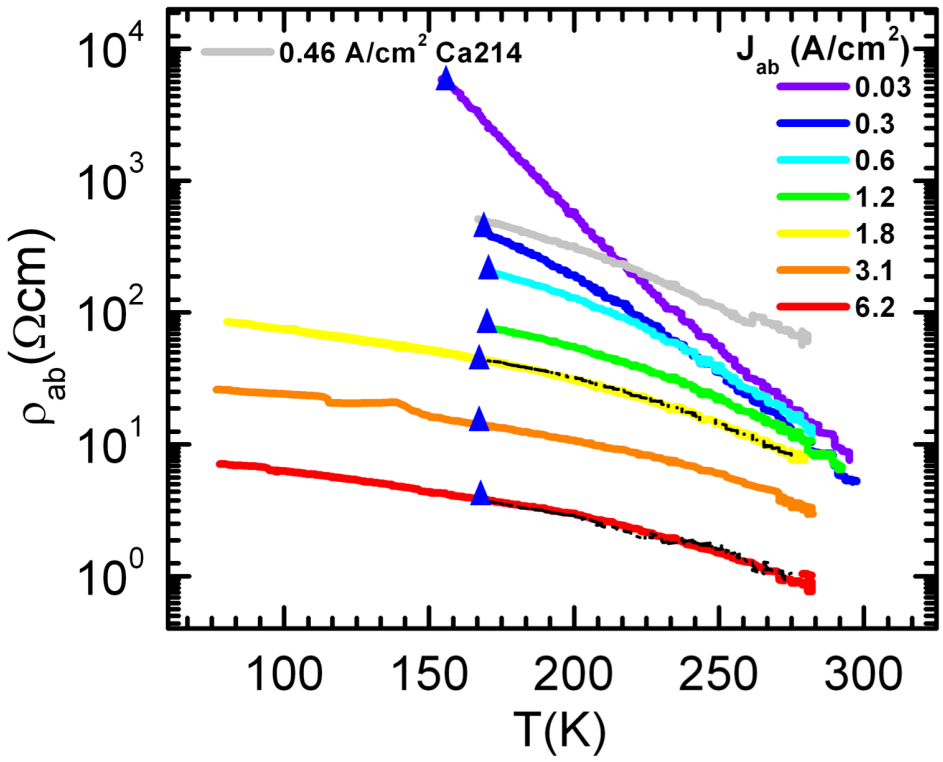

Fig. 2.19: Resistivity versus temperature of Ca214-Ru metal single crystal. The $\rho_{ab}(T)$ curves for $J = 1.8$ (yellow) and 6.2 (red) A/cm^2 measured by first decreasing T (continuous lines) and then heating the sample (dashed lines) are highlighted. The light grey curve is a $\rho_{ab}(T)$ curve of the Ca214 acquired at $J = 0.46$ A/cm^2. This latter emphasises the metallicity increases of Ca214-Ru with respect to Ca214.

matrix. As a consequence, the crystal structure of the Ca214-Ru samples expands more freely, avoiding the samples shatterer. Furthermore, as in the case of Ti-doped Ca214, it is possible to acquire the S-shaped $J(E)$ or $E(J)$ characteristics entirely. Moreover, the measurements can be repeated multiple times without damaging the sample. In addition, as reported in Fig. 2.21 we observed the same effect biasing the sample along the c axis. Curiously, in this configuration, although the sample is more resistive than the ab plane configuration, to induce the IMT is more manageable. Indeed, while in the ab plane configuration, considerable care has to be placed to maximize the sample cooling as in the case of Ca214 (see section 2.1), in this case, the wires on the sample, can be simply connected by using a commercial silver epoxy, and any other precaution is not needed. Finally, it is worth noting that in Ca214-Ru the values at which the IMT transition occur, E_{th}, in the ab plane

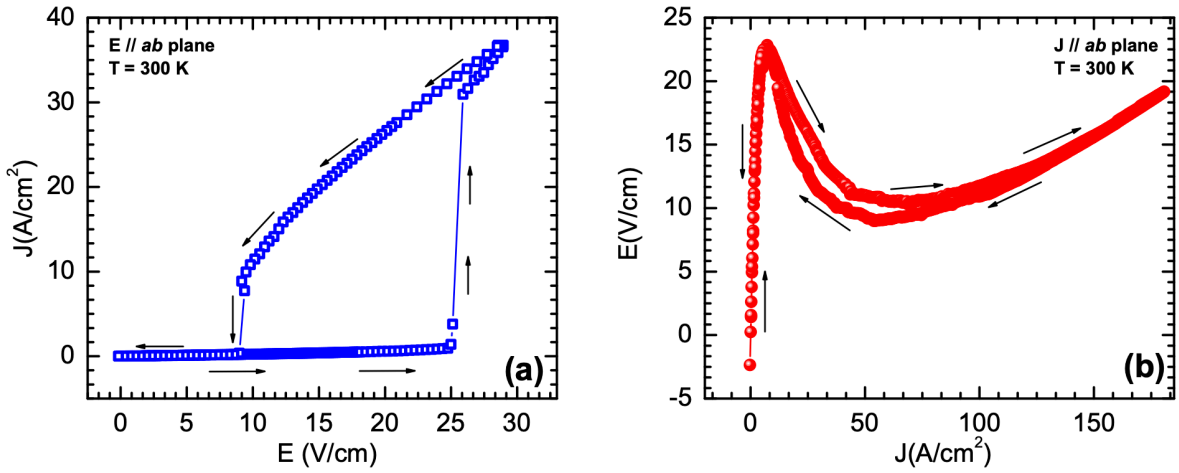

Fig. 2.20: (a) $J(E)$ characteristic of Ca214-Ru at room temperature acquired providing a bias-voltage parallel to the ab plane. (b) $E(J)$ characteristic on the same sample and measurement configuration, but feeding it with a bias-current.

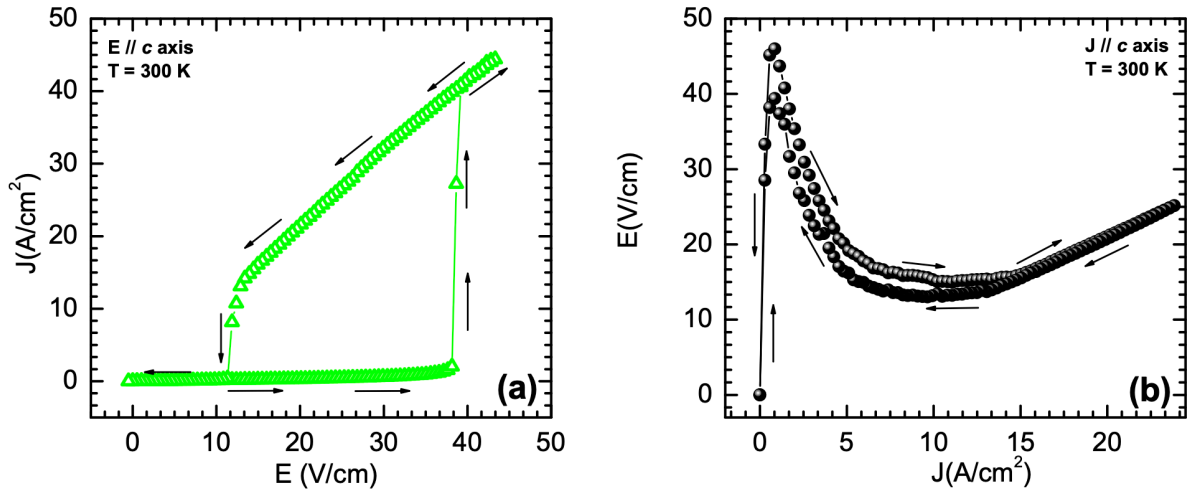

Fig. 2.21: (a) $J(E)$ characteristic of Ca214-Ru (same sample of Fig. 2.20) at room temperature acquired providing a bias-voltage parallel to the c axis. (b) $E(J)$ characteristic on the same sample and measurement configuration, but feeding it with a bias-current.

and c axis configurations, are consistent with the values found in the Ca214 literature [27,28]. Moreover, we point out that our results make the Ca214-Ru a valuable and durable system that not only conserve the properties of the Ca214, allowing a deep understanding of the physics underneath its features, but it is also a relevant material that could be used for electronic applications.

Chapter 3

Universal size-dependent nonlinear charge transport in single crystals of the Mott insulator Ca_2RuO_4

G. Avallone†, R. Fermin†, K. Lahabi, V. Granata, R. Fittipaldi, C. Cirillo, C. Attanasio, A. Vecchione, and J. Aarts

This chapter has been accepted for publication in *npj Quantum Materials - Nature.*
†These authors contributed equally to this work.

Abstract

The surprisingly low current density required for inducing the insulator to metal transition has made Ca_2RuO_4 an attractive candidate material for developing novel Mott-based electronics devices. The mechanism driving the resistive switching, however, remains a controversial topic in the field of correlated electron systems. Here we probe an uncovered region of phase space by studying high-purity Ca_2RuO_4 single crystals, using the sample size as principal tuning parameter. Upon reducing the crystal size, we find a four orders of magnitude increase in the current density required for driving Ca_2RuO_4 out of the insulating state into a non-equilibrium phase which is the precursor to the fully metallic phase. By integrating a microscopic platinum thermometer and performing thermal simulations, we gain insight into the local temperature during simultaneous application of current and establish that the size dependence is not a result of Joule heating. The findings suggest an inhomogeneous current distribution in the nominally homogeneous crystal. Our study calls for a reexamination of the interplay between sample size, charge current, and temperature in driving Ca_2RuO_4 towards the Mott insulator to metal transition.

3.1 Introduction

Strongly correlated electron systems, and in particular the metallic oxides, have truly marked a paradigm shift in physics, inspiring a decades-long search for novel quantum materials to explore exotic phenomena, such as high-temperature superconductivity [43], electron hydrodynamics [44,45], and holography [46,47]. A prime example of this, is the family of ruthenates witch exhibits a rich and diverse phase diagram that includes Mott insulators [19,48], unconventional superconductivity [49, 50], and magnetism [51, 52]. The $4d$ electron Mott insulator Ca_2RuO_4 [19] (hereafter Ca214) has become the subject of intense research in recent years due to its intriguing electrical [3, 22, 26,29,31,35,37,53–58] and magnetic properties [21, 59]. Specifically, at room temperature it undergoes a current-driven insulator to metal transition (IMT) which occurs at unusually low electric (E-)field or current density (J) thresholds ($\sim$40 V/cm or few A/cm^2 respectively) [27, 28]. This is in contrast to previous reports on Mott insulators, where the IMT is limited to low temperatures and/or to the application of high E-fields [60,61]. The capacity to switch between resistive states at room temperature is a desirable property to realize current switchable memories, neuromorphic devices, and next-generation oxide electronics [62, 63].

The underlying mechanism responsible for such low current densities is still a topic of intense debate. Due to its high resistivity in the insulating state, Joule heating plays a significant role since the IMT can also be thermally driven by heating the crystal above 357 K [35]. This has led to ambiguity about the origin of the IMT, and whether it is thermally or electronically driven, as evident by the large number of works discussing local heating [5, 28, 31, 42, 64–66]. Specifically, in a recent work, it was found that the IMT is always accompanied by a local temperature increase to the transition temperature [64]. Moreover, as a precursor to the metallic phase, a third and non-equilibrium phase has been detected by x-ray and neutron diffraction experiments, and additionally with Raman spectroscopy [3, 53, 54]. This non-equilibrium phase seems to be induced by low current densities, but its role in the current-driven IMT remains elusive. Another major hurdle is the pronounced structural transition accompanying the IMT, in which the RuO_2 octahedra are elongated, and the unit cell is transformed from orthorhombic to tetragonal [3, 24, 25, 27, 29, 31, 53]. This transition leads to a strong temperature dependence of the unit cell volume ($\sim$1% between 100 K and 400 K), introducing large internal strains in the crystal, often resulting in the formation of cracks or even shattering the crystal upon reentering the insulating phase [24].

Although it is much debated whether the IMT is primarily triggered by Joule heating or driven by electronic effects, a parameter that has been left unexplored in this discussion is the *size* of the samples. Decreasing the size of bulk samples down to μm range gives larger control over current paths in the crystal (due to the uniform rectangular cross section). Furthermore, micro cracks and step-like terraced edges, which occur naturally in mm-sized bulk crystals, are scarce in microscopic samples. Also, since the voltage contacts cover the full side of the microscopic samples, current injection is more homogeneous. This is in contrast with mm-sized crystals where point contacts, and their entailing current crowding effects, are more common. Finally, due to the enhancement of the surface to volume ratio and the direct contact with an isothermal substrate, the flakes are expected to be less susceptible to thermal gradients and heating effects.

Here we carry out an extensive size-dependent study using a large number (39) of ultra-pure single crystal samples of Ca214, ranging between the hundreds of nm and the millimeter scale. We examine the role of the current density in inducing the non-equilibrium phase, which we can probe reversibly

(i.e., without inducing the IMT and consequently damaging or altering the crystal). We find a surprising enhancement of the required current density by at least four orders of magnitude upon decreasing the cross section. By integrating a micrometer-sized platinum thermometer, we are able to directly probe the local temperature of the microscopic samples, and demonstrate that the pronounced size dependence is not caused by thermal effects. Our findings call for a careful reexamination of the relevant mechanism behind the non-equilibrium phase and its relation to the IMT in Ca214.

3.2 Results

3.2.1 Characterizing microscopic samples

To examine the crossover from large mm-sized bulk behaviour to the microscopic one, we have produced samples of varying cross section between 0.5 mm^2 and 0.5 μm^2. The microscopic samples were fabricated using mechanical exfoliation [67]. This enables us to produce micron-sized "crystal flakes", which can be lithographically contacted for electrical transport measurements, without compromising the material quality. In addition to the microscopic samples, we have fabricated mm-sized bulk samples that are hand-contacted by the use of silver paint. We employed a focused Ga^+-ion beam (FIB) as the principal structuring technique throughout this work. This provides us with the means to control the cross section in a systematic manner. Fig. 3.1(a) and 3.1(b) show scanning electron microscope and optical microscope images of samples in microscopic and mm-sized ranges respectively.

All measurements are carried out by biasing a current in the ab-plane rather than a voltage, since inducing the metallic state by the application of electric field is more abrupt and therefore the crystals are more likely to break. Furthermore, current density as a function of electric field is hysteretic which complicates the study of size effects carried out here. We have conducted electric field versus current density ($E(J)$-characteristic) and resistivity measurements as a function of temperature, and found that the microscopic samples qualitatively show similar behaviour as the mm-sized bulk samples [53]. Typical results from microscopic samples are summarized in Fig. 3.1(c) and 3.1(d). It is important to note that, despite several orders of magnitude of size variation, we find the room temperature resistivity of all our samples (microscopic and mm-sized bulk) to be comparable, and in

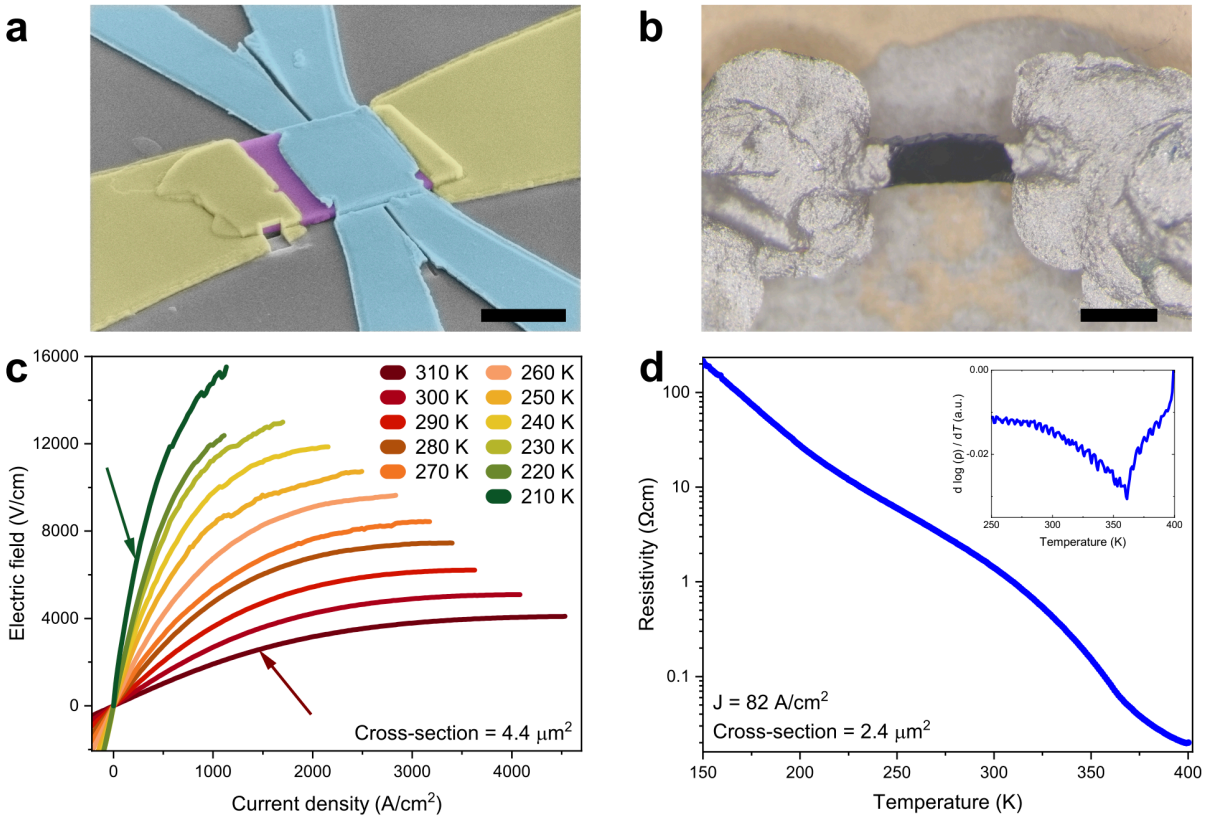

Fig. 3.1: Transport characteristics of microscopic samples. (a) Displays a false colored scanning electron micrograph of a microscopic sample (in purple) that is contacted by yellow colored Ti/Au contacts. In blue the embedded Pt-thermometer, that can be employed to locally measure the temperature, is shown. The scale bar represents 3 μm. (b) Shows an optical microscope image of a mm-sized sample, where the scale bar measures 500 μm. Panel (c) shows $E(J)$-characteristics acquired on a microscopic sample at different temperatures. The arrows indicate the current density that would correspond to the Figure of Merit (see section 3.2.2). Note that these curves are obtained below the IMT. The resistivity versus temperature of a typical microscopic sample is shown in panel (d). In the microscopic size range we do not observe a sharp temperature induced IMT, however, as indicated by the inset (the derivative of the curve in the main figure), there is a clear inflection point indicating the thermal transition.

good agreement with the literature values [19]. Curiously, however, the temperature induced IMT is broadened in microscopic samples with respect to mm-sized bulk samples (see Fig. 3.1(d)). We attribute the broadening of the transition to the small sample thickness since similar effects are observed in thin film samples [68–71]. We did observe an abrupt change in resistivity upon cooling a relatively thick (T = 1.5 μm) microscopic sample through the

metal to insulator transition for further discussion on this aspect the reader is referred to the Supplementary Note S2.

3.2.2 Comparing samples of different cross section

Fig. 3.1(c) shows $E(J)$-characteristics obtained on a microscopic sample at different temperatures. These curves qualitatively show similar behaviour as the mm-sized bulk samples. However, the current density required for triggering the meta-stable phase, which is indicated by a negative $\mathrm{d}E/\mathrm{d}J$ as a function of J, exceeds the literature values (for mm-sized crystals) by at least four orders of magnitude [27, 31, 64]. This is demonstrated in Fig. (a), where we plot the differential resistivity $\mathrm{d}E/\mathrm{d}J$ as a function of J for selected samples. The current density at which $\mathrm{d}E/\mathrm{d}J$ begins to decline, corresponding to nonlinear conduction, increases if the sample size is reduced to microscopic scales. In order to compare the nonlinear conduction under applied current between different samples in a systematic manner, we propose a Figure of Merit (FOM) that can be applied to samples of different sizes (see Fig. 3.2). First, differential resistivity versus current density curves are computed by analytically differentiating the $E(J)$-characteristics (Fig. 3.2(a)). The curves are then normalized with respect to their low current value (i.e., currents for which the resistivity is current independent and conduction is linear). We choose the current density at which the slope of the $E(J)$-curve has halved as our Figure of Merit, called the 50%-slope current density. The choice for this FOM is suitable since we can compare the size dependence of the $E(J)$-characteristic in a regime where heating effects play a relative unimportant role (see section 3.2.3). Furthermore, at the FOM current density, neither the metallic phase nor even the meta-stable phase is induced in the sample [53]. However, we find the shape of the $E(J)$-curves to be the same between all measured samples. Therefore, the current density required for inducing the meta-stable phase, scales with the FOM current density accordingly, which allows for determining the current density needed to induce the meta-stable phase. Lastly, the slope of the differential resistivity appears to be maximal at the FOM. Therefore, the choice of this FOM leads to a small uncertainty in the estimated current density, which would not be the case when using the current density at the maximum E-field, for instance.

Fig. 3.2(b) displays the FOM as a function of the sample cross section for all measured samples. The current density at which nonlinear conduction sets

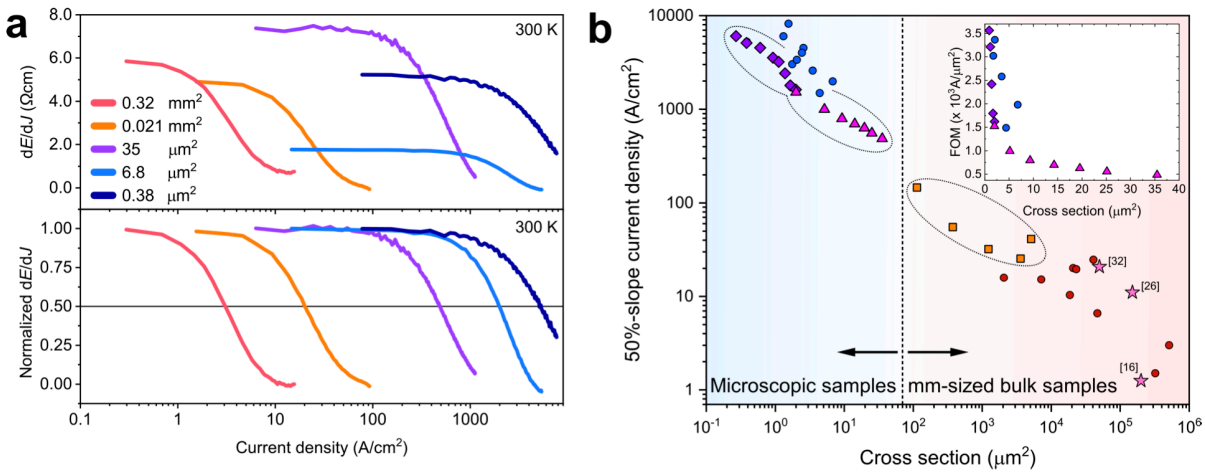

Fig. 3.2: Size dependence of nonlinear conduction. The top panel of (a) shows the differential resistivity $\mathrm{d}E/\mathrm{d}J$ as a function of current density of a few selected samples at room temperature. The legend shows the cross-sectional area of these samples. For all microscopic and mm-sized bulk samples the low current resistivity at room temperature is found to be corresponding to the literature values. In the lower panel of (a), the differential resistivity of these samples is normalized with respect to the low current resistivity (i.e., where the resistivity is current independent). Even though the $E(J)$-characteristics of all samples are qualitatively the same, the current density scale at which they exhibit nonlinear conduction differs orders of magnitude. The current density at which the slope of the $E(J)$-characteristic is halved, is chosen as the Figure of Merit (FOM), which corresponds to the horizontal reference line. (b) shows the FOM as a function of cross-sectional area for all measured samples at room temperature on a log-log scale. N.B. each circular point corresponds to a single sample. The thinning study samples are depicted with a unique non-circular symbol and a different color. The inset displays the FOM vs sample cross section for selected samples on linear scales. The star-symbols correspond to the FOM extracted from literature; the label indicates the reference number.

in, grows monotonically with decreasing sample dimensions and, curiously, the FOM shows a power law dependence on the cross-sectional area. To exclude any potential artifacts associated with sample preparation, we performed a thinning study on three samples over a large size range. We incrementally modify the width and thickness of the same crystal through consecutive FIB structuring steps, and measure the $E(J)$-characteristic, after each one. Following this procedure, we changed the width of a single microscopic sample in up to seven different thinning steps. Moreover, in a mm-sized bulk sample, we were able to decrease the sample width by a factor 50. Samples on which

a thinning experiment was carried out are encircled and highlighted in Fig. 3.2(b) by a non-circular symbol and a different color. The FOM as a function of only the width or thickness of the sample (see Supplementary Note S3) reveals the size dependence is not exclusively formed by any of these two parameters, but is rather a combination between them, which means that neither of these dimensions are more significant in determining the transport properties of the crystal. The simplest combination of the two parameters is the cross section, which is chosen in Fig. 3.2(b). Supplementary Fig. S5 shows the FOM as a function of volume.

Despite the clear trend in Fig. 3.2(b), there is a sample to sample variation that cannot be explained by the uncertainty in the measured crystal dimensions. The deviation from the trend in the mm-sized samples can be explained by irregular current paths in the sample and inconstant cross-sectional area throughout the length of the sample. For the microscopic samples this does not hold. However, the ratio between width and thickness differs among the samples, and therefore they are expected to respond differently to decreasing dimensions if surface layer effects are important. Furthermore, oxygen relocation can play a role in modifying the crystal structure when passing a current, resulting in a change of transport properties between current cycles. This is consistent with our observations, where, in some cases, the $E(J)$-characteristic slightly changes after different current or temperature cycles. These arguments can explain the increase in spread observed in Fig. 3.2(b).

3.2.3 The role of temperature

All the experiments reported previously, where the temperature is locally measured in Ca214, are carried out on mm-sized bulk samples using optical techniques, since local contact thermometry is experimentally difficult to realize at these dimensions. Microscopic samples do not have this limit and enable contact thermometry to give insight into the local sample temperature. To implement this, we carefully designed and fabricated a platinum thermometer on top of selected microscopic samples (see Fig. 3.1(a)). Since platinum has a distinctly linear temperature dependence, we are able to accurately measure the temperature of the microscopic samples, while simultaneously driving a current using an independent bias (see Supplementary Note S1 for details).

In order to make plausible that the temperature difference between the Pt and the sample is negligible and to investigate the likelihood of potential

temperature gradients in the sample, we have performed thermal simulations accompanying the thermometry results. Here we solved for a steady-state temperature, under the assumption that heat is generated uniformly in the crystal flake while the substrate temperature remains constant 50 μm away from the sample. The full technical details of these simulations can be found in Supplementary Note S6.

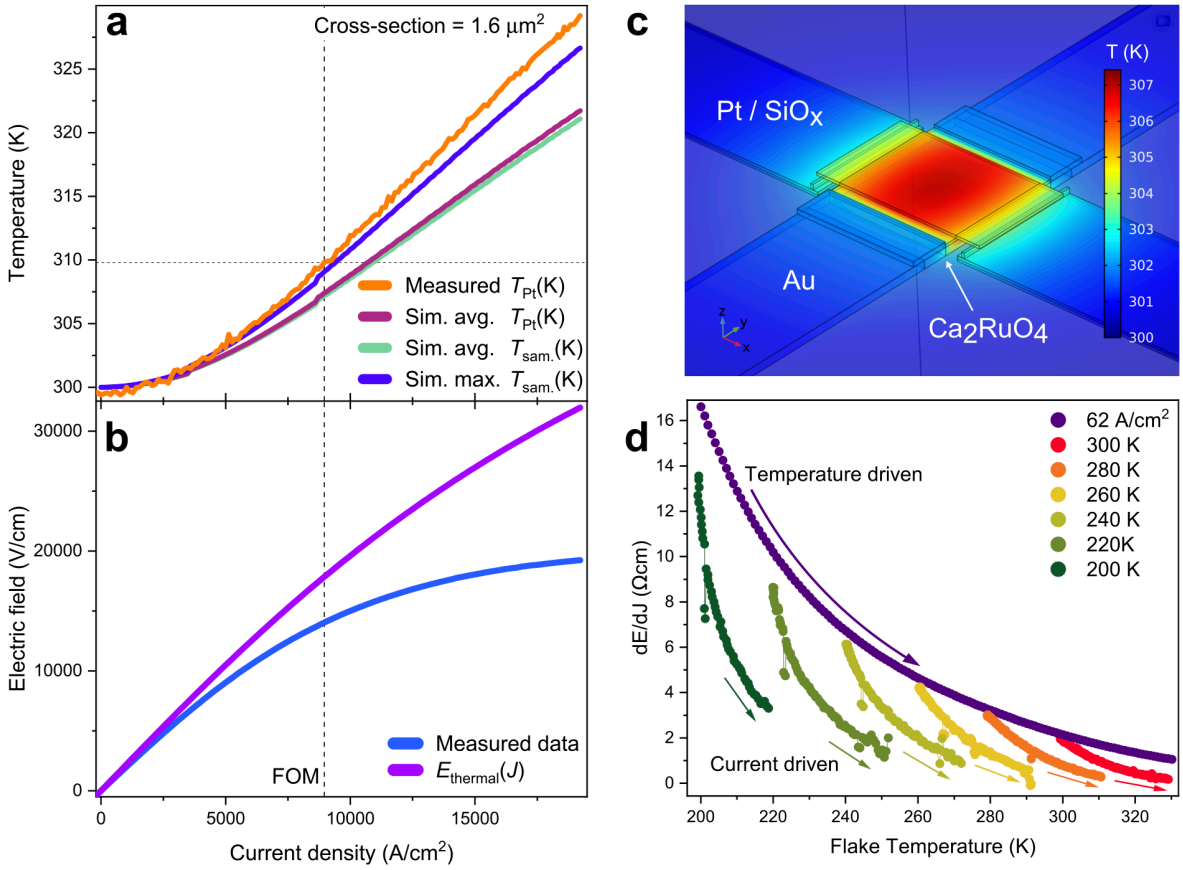

Fig. 3.3: The role of temperature in microscopic samples. (a) displays the local measured Pt temperature and multiple simulated temperatures as a function of the applied J. The data is acquired on the sample depicted in Fig. 3.1(a). The substrate temperature is 300 K. (b) shows the electric field acquired simultaneously with the temperature measurement. The measured data is compared to E_{thermal} (i.e., the calculated electric field on basis of Joule heating only). The vertical reference line indicates the FOM. The local temperature increase at the FOM is below 10 K. A simulated temperature heatmap of the sample at the FOM current density is shown in (c). (d) displays the differential resistivity as a function of the flake temperature. Either the background temperature or the driven current density is changed. At all current densities, the nonlinear conduction is stronger than heating effects can provide.

Fig. 3.3(a) displays the platinum temperature obtained on the sample

shown in Fig. 3.1(a) (orange curve) together with the simulation results as a function of current density. The measured temperature is exceeding the expected averaged Pt temperature (purple curve) for high currents. This can be caused by the absence of heat transfer barriers between the simulated elements, whereas in experiments these can be expected. The purple curve can therefore be considered as a lower bound of the expected Pt temperature. Nevertheless, the simulated average sample (green curve) and Pt temperature (purple curve), show correspondence to a high degree. We have also examined temperature gradients in the sample and found temperature differences to be limited to 3 K in the sample (see Fig. 3.3(c) and Supplementary Note S6). Furthermore, we evaluate the maximum temperature within the simulated flake geometry (blue curve) and compare it to simulated average Pt temperature. We find these to differ less than 2 K at the FOM current density. Therefore, we consider our Pt thermometry technique suited for acquiring the average sample temperature at the FOM. At the FOM current density, the locally measured temperature increase is found to be less than 10 K. Therefore, we conclude that Joule heating is non-zero but similar to mm-sized bulk samples [64].

The measurement of the local temperature enables us to calculate what the $E(J)$-characteristic would look like on the basis of heating effects only. For the resistivity versus temperature measurement on this sample, we compute the $\mathrm{d}E/\mathrm{d}J$ from our $E(J)$-characteristics for low currents (i.e., where the resistivity ρ is current independent):

$$\rho(T) = \frac{\mathrm{d}E}{\mathrm{d}J}(T, J \approx 0) \tag{3.1}$$

Since the temperature is homogeneous up to a variation of 3 K over the entire sample, we can use the locally measured temperature as a function of current density to find the $\mathrm{d}E/\mathrm{d}J$ as a function of heating effects:

$$\frac{\mathrm{d}E_{\mathrm{thermal}}}{\mathrm{d}J}(J) = \frac{\mathrm{d}E}{\mathrm{d}J}(T(J), J \approx 0) = \rho(T(J)) \tag{3.2}$$

Integrating the equation (3.2), we can reconstruct the $E(J)$-characteristic that would have been measured if Joule heating was the only mechanism

causing the nonlinear conduction[1]:

$$E_{\text{thermal}}(J) = \int \frac{\mathrm{d}E_{\text{thermal}}}{\mathrm{d}J}(J)\mathrm{d}J \tag{3.3}$$

We denote this reconstructed function as $E_{\text{thermal}}(J)$ and plot it alongside the measured data in the lower panel of Fig. 3.3. Even at low current densities, the actual measured data shows stronger nonlinear conduction than $E_{\text{thermal}}(J)$, indicating that current-driven effects are significant in the microscopic samples for all applied current densities probed in this study.

Alternatively, the differential resistivity as a function of local sample temperature is plotted in Fig. 3.3(d). The purple curve describes the resistivity as a function of temperature with a constant current density (62 A/cm^2). Alongside, we plot the differential resistivity as a function of increasing bias current, while maintaining a constant substrate temperature. Evidently, the slope decrease of $E(J)$-characteristic, caused by the application of current, is not primarily driven by Joule heating.

We conclude on the basis of our thermometry experiments that the size dependence presented in Fig. 3.2(b) cannot be explained by Joule heating. Furthermore, we find that a current-driven mechanism is present parallel to Joule heating in the non-equilibrium phase.

3.3 Discussion

Before discussing the possible origin of the observed size dependence, we consider the following notes. Firstly, there seems to be no intrinsic length scale found in our measurements. This can be seen from the absence of a specific cross section where the FOM changes discontinuously. Secondly, we can exclude the effects of micro cracks since the size dependence continues even in the microscopic regime where micro cracks are not present. By inspecting the samples with a scanning electron microscope, we could confirm that no micro cracks were induced by measuring the $E(J)$-characteristic. Thirdly, the observation of a current-driven mechanism parallel to Joule heating, as observed here, was recently also reported by Jenni et al. [42]. Lastly, we note that our findings are consistent with the reports on epitaxially grown thin

[1]Here the integration constant is set by the zero electric field for zero current density criterion: $E(0) = 0$. See Supplementary Note S5 for more details.

films of Ca214, where the current density required to induce the IMT was also found to be many orders of magnitude higher than in bulk literature values [68].

The emergence of the metallic phase was recently attributed by Terasaki et al. to energy flow, as opposed to charge transport [65]. In this study, the energy flow corresponds to the dissipated power (product of current and voltage IV), in contrast, here it is more insightful to describe the product of electric field and current density EJ (power dissipation density), enabling the comparison of samples of different length scales. Since microscopic samples show a four order of magnitude increase in current density at which we observe nonlinear transport, we find that the power dissipation density is eight orders of magnitude larger in microscopic samples than in mm-sized bulk samples (see top panel of Fig. 3.3). It is therefore unlikely that the energy flux through the crystal is responsible for observed size dependence.

Alternatively, the size dependence might be explained by strain induced through coupling to the substrate. In the zero-current limit, however, the substrate does not exercise any strain on the crystal, as we will discuss below. The room temperature resistivity of Ca214 is strongly dependent on strain and the IMT can be induced by applying $\sim$0.5 GPa of pressure [29, 57, 58]. By using ultra low currents ($\backsim$nA), we have confirmed that the insulating-state resistivity of the micrsocopic samples matches that of their mm-sized counterparts, signalling the absence of strain. Moreover, in a previous work on the isotructural unconventional superconductor Sr214, we have prepared microscopic samples using equal methods and substrates [72]. These samples retained bulk properties to sizes below 200 nm, whereas, like Ca214, its transport properties are heavily dependent on strain [73–75]. Therefore we conclude that our microscopic samples do not experience strain at zero current bias. In simultaneous transport and XRD measurements, it has been shown that at the FOM current density, there is no detectable change of the lattice parameters [53]. Combined with the absence of strain at zero current bias, this leads to the conclusion that our samples do not experience any strain at the FOM, regardless of their size. Thus, we do not regard strain as a plausible explanation for the observed size dependence.

Near the the IMT, and independent whether that is induced by current or temperature, the arguments supporting the absence of strain no longer hold, as the lattice constants significantly alter [3, 53]. Although we are far below the IMT in our current-driven experiments, we pass the IMT in the

temperature sweep, presented in Fig. 3.1(d). Strain related effects could be responsible for the observed broadening of the transition. Moreover, a broadened transition is commonly observed in thin films, where strain induced by the substrate is expected to be an influential parameter [68–70].

Finally, an inhomogeneous distribution of current throughout the cross-sectional area could potentially explain the size dependence found here. Since the current density is calculated by dividing the applied current by the entire cross section, the apparent current density in mm-sized bulk samples might be lower than the actual current density that is physically relevant. Due to their size and geometry, however, in the microscopic samples the apparent and actual current densities can be more similar.

Metallic filament formation, which are known to occur in Mott insulators, may induce such highly inhomogeneous current distributions [76]. Contrarily, for Ca214, Zhang et al. inspected phase separation using scanning near field optical microscopy (SNOM) and found a ripple pattern at the phase boundary between the insulating and metallic states [31]. Although the resolution of the SNOM technique might be insufficient to rule out sub 100 nm channel formation, it is difficult to reconcile the striped pattern found in SNOM with filament formation at present.

Furthermore, Zhang et al. find that the metallic phase nucleates at the top of the sample and its depth increases when traversing a phase boundary in the phase-separated state. This could suggest an inhomogeneous distribution of current throughout the cross-sectional area, that is high at the edges of the crystal and decreases towards the center of the bulk. Since the microscopic crystals have a larger surface to volume ratio, the edges are relatively more dominant. If the current density gradually increases below the current-carrying surface, this proposed mechanism will not feature any length scale at which a discontinuous change is expected in the FOM, which is compatible with our findings. In Supplementary Note S7, a minimal toy model describing the inhomogeneous current density is presented. This model can reproduce the power law dependence observed in Fig. 3.2(b).

In conclusion, we have performed a detailed study on size-dependent electrical properties of the Mott insulator Ca_2RuO_4. We find a surprising relation between crystal size and the current density at which nonlinear conduction occurs, which increases four orders of magnitude when the sample size is reduced from 0.5 mm^2 to 0.5 μm^2. We have strong indications that the observed size dependence is not caused by Joule heating, using a local Pt-thermometer

fabricated on top of selected microscopic samples. Our findings indicate an intrinsically inhomogeneous current density distribution in single crystals of Ca_2RuO_4. This calls for a reexamination of the relevant role of current in the meta-stable phase and its possible relation to the IMT. As an outlook, the combination of microscopic samples with a well-controlled current path, and local platinum temperature probes, provides a novel approach to study the interplay between thermal and electronic effects, which can be used to study the IMT in Mott insulators.

3.4 Methods

Bulk single crystals of Ca214 were grown by a flux feeding floating zone technique with Ru self-flux using a commercial image furnace equipped with double elliptical mirrors described elsewhere [30, 41]. Several techniques, including XRD, energy dispersive spectroscopy, and polarized light optical microscopy analysis, have been used to fully characterize the structure, quality, and purity of the crystals.

The microscopic samples were fabricated by the use of mechanical exfoliation on highly resistive $SrTiO_3$ or sapphire substrates. The flake samples are significantly thicker than monolayers. Therefore, random strain patterns, wrinkles and folds associated with the thin film limit are absent. Due to the natural shape of the crystal flakes, the produced samples are suited best for passing current in the ab-plane. Therefore all experiments are carried out in this configuration.

Considerable effort was put into the fabrication of the electrical connections on the samples to reduce the contact resistance that possibly becomes an extrinsic origin for nonlinear conduction due to local Joule heating. To perform electrical transport measurements, the samples obtained by the exfoliation process were contacted by means of an electron beam lithography step followed by a Ti/Au sputtering deposition and a lift-off procedure. When necessary, we used electron beam induced deposition to provide an electrical reinforcement of the contacts by locally depositing an additional layer of tungsten-carbide on them. On the mm-sized samples, we found a resistive background in the $E(J)$-characteristics, from which we extracted the contact resistance to be less than 10 Ω, which is significantly smaller than the sample resistance, supporting the use of a 2-probe measurement.

We used the FIB technique to modify both the sample width and thickness

enabling the full control of sample dimensions and geometry over a large crystal size range (see Supplementary Note S4). After fabrication, we have confirmed by scanning electron microscope inspection that the microscopic samples lack any micro cracks. Some microscopic samples were contacted in a 4-probe geometry. Using these samples, we could confirm that the contact resistance is negligible in comparison to the sample resistance. In addition to the microscopic samples, we have fabricated conventionally mm-sized bulk samples that are contacted by hand using silver paint (*Agar Scientific G3691*).

In a second step of electron beam lithography, the Pt-thermometer was added on selected samples. The Pt-circuit is electrically isolated by a thin layer of sputter deposited SiO_x ($\sim$100 nm).
This ensures that the Pt-thermometer and sample form two decoupled electrical systems. The resistance between the Pt-circuit and the Ca214 sample was found to be over 1 GΩ and the $E(J)$-characteristic measured before and after the application of the Pt-thermometer was found unaffected, as demonstrated in Supplementary Note S1.

The electrical transport measurements were carried out by applying a current using a Keithley 6221 current source. The voltage drop over the sample was measured using a Keithley 2182a nanovolt meter.

3.5 Supplementary information

3.5.1 Supplementary Note S1: Measuring the local temperature of a microscopic sample with an embedded thermometer

Measuring the local sample temperature proved to be vital in many proceeding studies [5,28,31,42,64–66]. In order to have full insight on the local temperature, we fabricate a thermometer in direct contact with selected microscopic samples. After contacting the microscopic sample by Ti/Au contacts, using electron beam lithography and a lift-off procedure (see Fig. S1(b)), we sputter deposit a layer of approximately 100 nm SiO_x. In a second step of lithography, we design a patch over the microscopic sample that has four leads, enabling a 4-terminal measurement over the deposited material directly on top of the crystal, as depicted in Fig. S1(d). The material of choice for the thermometer circuit is platinum since its resistivity is highly linear over the temperature range where we carry out our experiments, as can be seen in the thermometer calibration in Fig. S1(c). The resistance of the Pt-thermometer changes by 0.27 K/mΩ. Furthermore, the thickness of the SiO_x layer was found to be optimal, providing both a disconnected electrical system from the crystal whereas remaining in thermal contact to provide sub-Kelvin measurement precision. Fig. S1(a) depicts the IV-characteristic acquired before and after the application of the thermometer. The induced change is found to be minimal as expected since the crystal and sample circuits are electrically decoupled. Generally, a resistance of over 1 GΩ is found between the crystal and the Pt-thermometer circuit.

Thermometry experiments were carried out on multiple microscopic samples. On thicker samples, it is technically more challenging to connect a Pt layer on top of the crystal, to the leads on the substrate. Therefore, these experiments are carried out on the smallest crystals only. To complement the data presented in the main text, we present a full data set obtained on another microscopic sample in Fig. S2.

3.5.2 Supplementary Note S2: Abrupt transition in a relatively thick microscopic sample

In most of the microscopic samples the temperature-driven IMT is broadened. Fig. 3.1(d) of the main text shows the general resistivity versus temperature behaviour of microscopic samples. However, on one of our microscopic samples with a relative large thickness (1.5 μm) with respect to the width (3 μm) we have acquired a resistivity versus temperature curve that is more resembling data acquired on a mm-sized bulk crystal (see Fig. S3(a)). We observe a hysteretic curve that displays an abrupt transition upon cooling through the MIT. N.B., the other transport properties of this sample are fully resembling a typical microscopic sample, including a high Figure of Merit current density. A false colored scanning electron micrograph of this sample is found in Fig. S3(b).

A possible origin of the observed broadening of the transition might be strain patterns in the sample caused by the coupling to the substrate. In the main text we argue that our microscopic samples do not experience any strain while driving a low current (current densities well below the IMT; including the FOM). Near the the IMT - independent whether it is induced by current or temperature - this no longer holds, as the lattice constants significantly alter and strain effect can dominate [3, 53]. Furthermore, a broadening of the transition is commonly observed in thin films, where strain caused by the substrate is a key parameter [68–70].

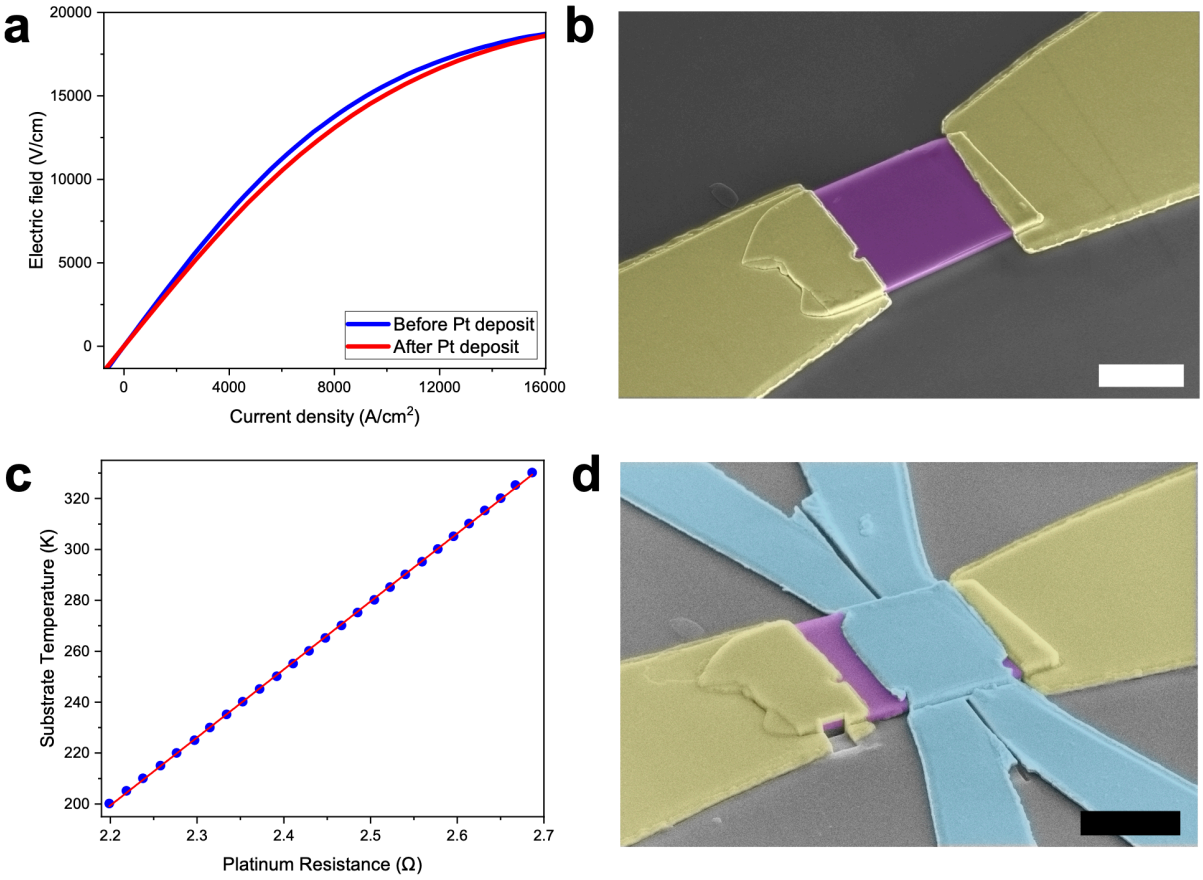

Fig. S1: Images and transport properties of the embedded Pt-thermometer. (a) Displays the $E(J)$-characteristic before and after the deposition of the Pt-thermometer. (b) Shows a false colored SEM image of the sample before the application of the thermometer and (d) shows a false colored SEM image that is acquired after the fabrication of the thermometer. In these images, the crystal is colored purple, the titanium/gold contacts to the crystal are yellow, and the platinum is light blue. The scale bar corresponds to 3 μm in both SEM images. In (c) the calibration curve of the Pt-thermometer, which is fitted by a linear curve, is shown. The slope of the fit corresponds to 0.27 K per mΩ. This enables sub-Kelvin precision thermometry.

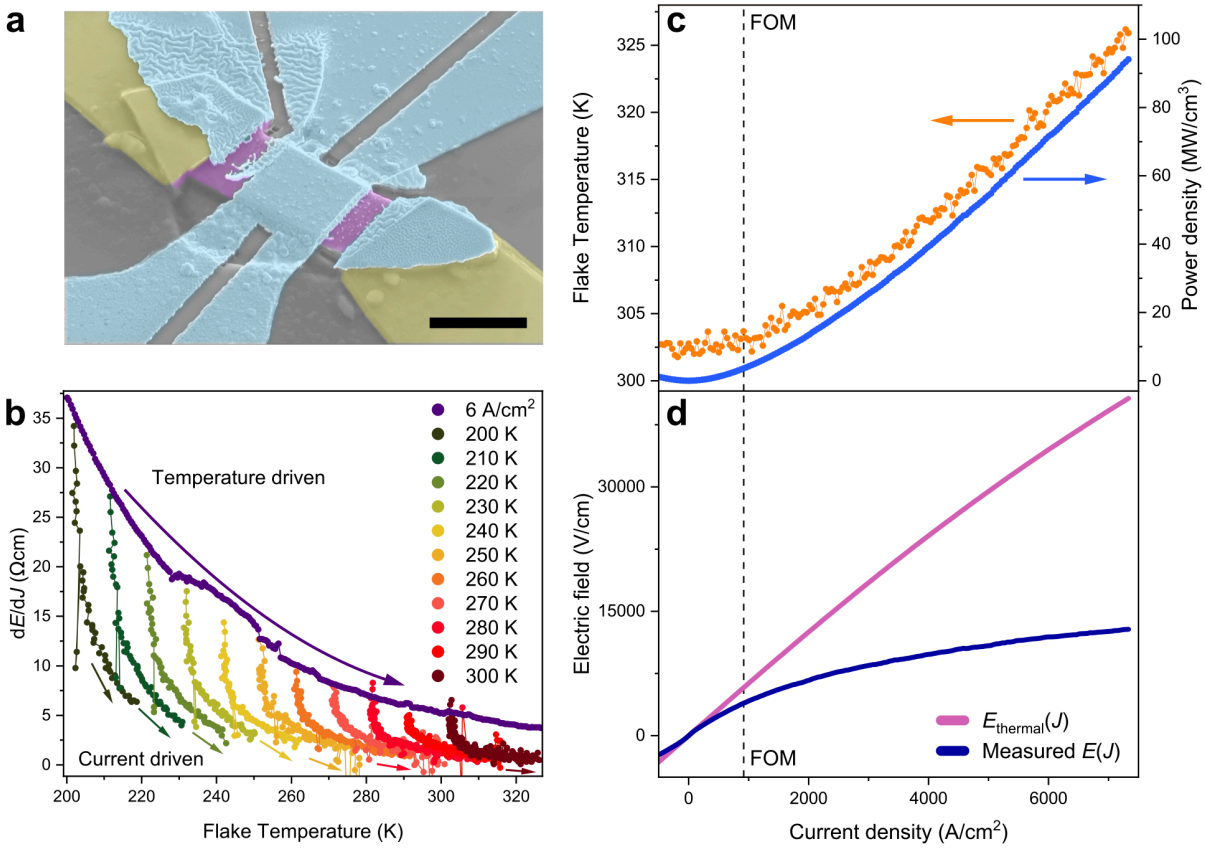

Fig. S2: Complementary thermometry data set obtained on a microscopic sample. (a) Shows a false colored scanning electron micrograph of a microscopic sample with a Pt-thermometer ($A = 1.8\ \mu$m). The crystal is colored purple, the titanium/gold contacts are yellow and the platinum is indicated by light blue. The scale bar corresponds to 6 μm. In (b) the differential resistivity as a function of local sample temperature, analogous to Fig. 3.3(d) of the main text, is shown. (c) depicts the local temperature and dissipated power density (product of E and J) as a function of current density. A comparison between the measured $E(J)$-characteristic and E_{thermal} (see section S5 and section 2.3 of the main text) is shown in (d). The dashed line indicates the Figure of Merit current density.

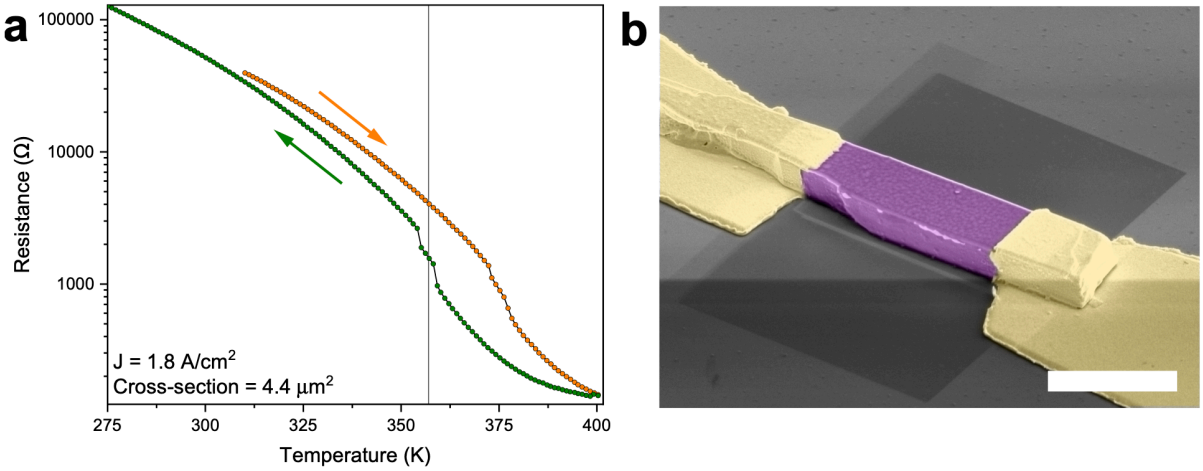

Fig. S3: Resistance versus temperature of a relatively thick microscopic sample. (a) Shows the resistance versus temperature of a microscopic sample that is 1.5 μm thick and 3 μm wide, which is relatively thick for a microscopic sample. We observe hysteresis on cycling the temperature and see an abrupt change in resistance when passing the thermal transition temperature of 357K as indicated by the vertical reference line. In (b) a false colored scanning electron micrograph is shown of the sample on which the data in (a) is acquired. Purple indicates the crystal and yellow colored are the titanium/gold contacts to it. The scale bar corresponds to 5 μm.

3.5.3 Supplementary Note S3: The Figure of Merit as a function of other length scales

In Fig. 3.2(b) of the main text, we have chosen to plot the Figure of Merit as a function of the cross-sectional area. Here we present the same data as a function of thickness, width and length (between the voltage contacts) of the crystal, as plotted in Fig. S4. Most instructive is to inspect the samples on which we have performed a thinning study, these are highlighted by the use of a non-circular symbol in Fig. S4. If we first consider samples of constant thickness, we observe that the FOM can change an order of magnitude in a single sample while decreasing the width, which rules out a dependence solely on thickness. A similar argument can be made for the width and length dependence. Indeed, we have carried out a single step of decreasing the thickness of a sample, which is indicated by the use of arrows in Fig. S4. While the width is constant, the Figure of Merit changes again if we decrease the thickness of this sample.

If we, however, plot the Figure of Merit as a function of the cross-sectional area of the sample, as is done in Fig. 3.2(b) of the main text, we find that the thinning study samples follow a more coherent trend. We therefore use the cross-section as a typical length scale measure.

We can conclude from this observation that neither thickness, width or length of the crystal solely govern the Figure of Merit, meaning that none of these dimensions are more special in determining the transport properties of the crystal.

Fig. S5 shows the FOM as a function of sample volume. Since $V^c = l^c A^c$ (where, V is the volume, l is the distance between the voltage contacts, A is the sample cross-section, and c is a constant) we see a very similar dependence of the FOM on volume as on the cross-sectional area.

3.5.4 Supplementary Note S4: Additional information on FIB structuring

The motivation for using FIB structuring in this work is two-fold. Employing FIB, we can structure the microscopic samples to have a rectangular cross-sectional area, which ensures full control over the current path. Furthermore, in order to rule out any geometry related artifacts, we performed a thinning study on three different samples corresponding to three different sample size ranges. By the use of FIB, we can sculpt the sample and reduce the cross-sectional area between consecutive $E(J)$-measurements.

An often heard point of criticism on FIB processing is the implantation of Ga-ions in the material and in general damages of the crystal due to the high impulse of the ions. Key in resolving these issues is the combination of ultra-low beam currents and a SiO_x capping layer. The first ensures that the damages are only very local (approximately within 30 nm from the edge of the milled structure), the second protects the top side of the crystal during inevitable radiation of Ga-ions.

In a previous work on the isostructural superconducting ruthenate Sr214, we have shown that it is possible to structure this complex oxides with up to 200 nm features without sacrificing sample quality [72]. Superconductivity in Sr214 is very sensitive to disorder and therefore producing samples with high residual resistivity ratios that show a literature value critical temperature, is a strong indication of the absence of any FIB induced damages. To illustrate the thinning experiment, Fig. S6 shows false colored images of the three samples before thinning and after a couple of thinning steps.

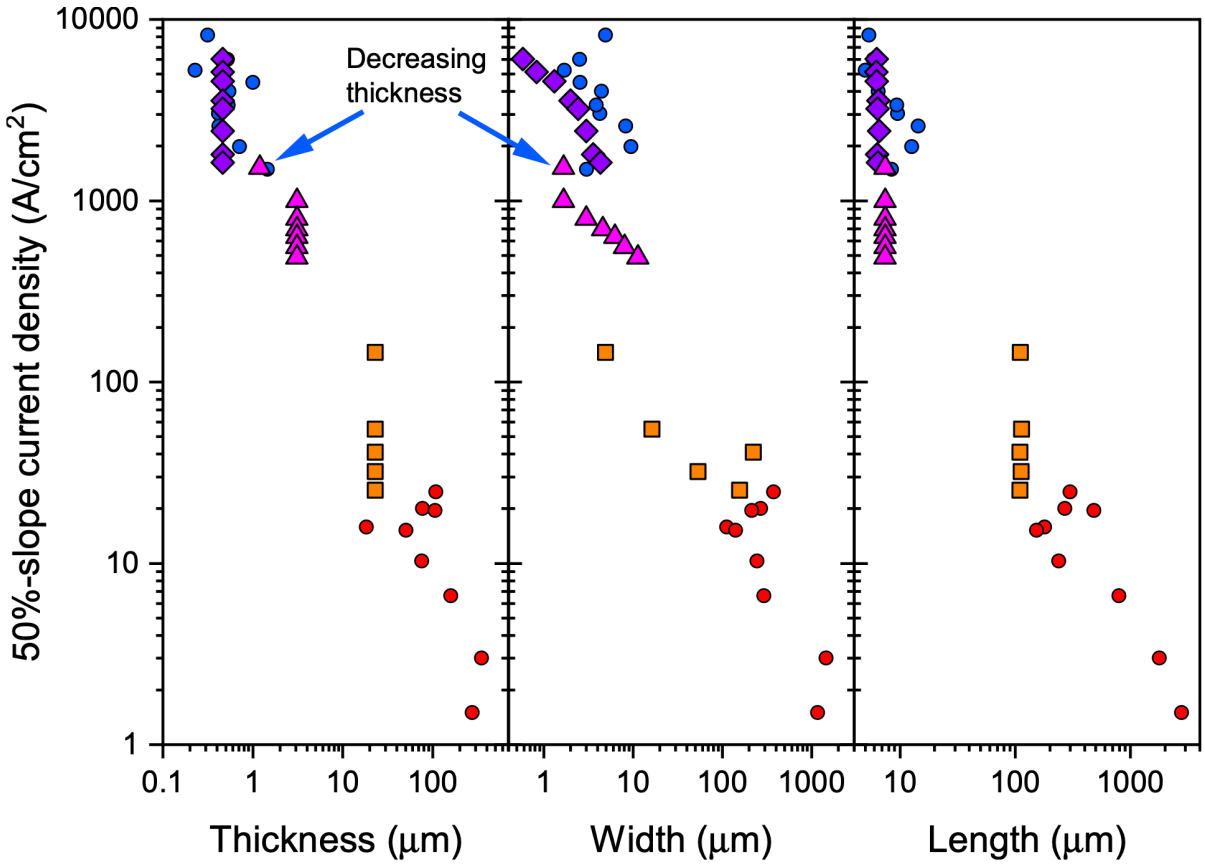

Fig. S4: the 50%-slope current density (FOM) shown as a function of different length scale parameters of the measured samples. In this figure, each circular symbol represents a single sample. The non-circular symbols represent the thinning study samples (see Fig. S6 for images of these). The arrows indicate the decrease of thickness during the thinning study on the sample depicted in Fig. S6(c) and S6(d).

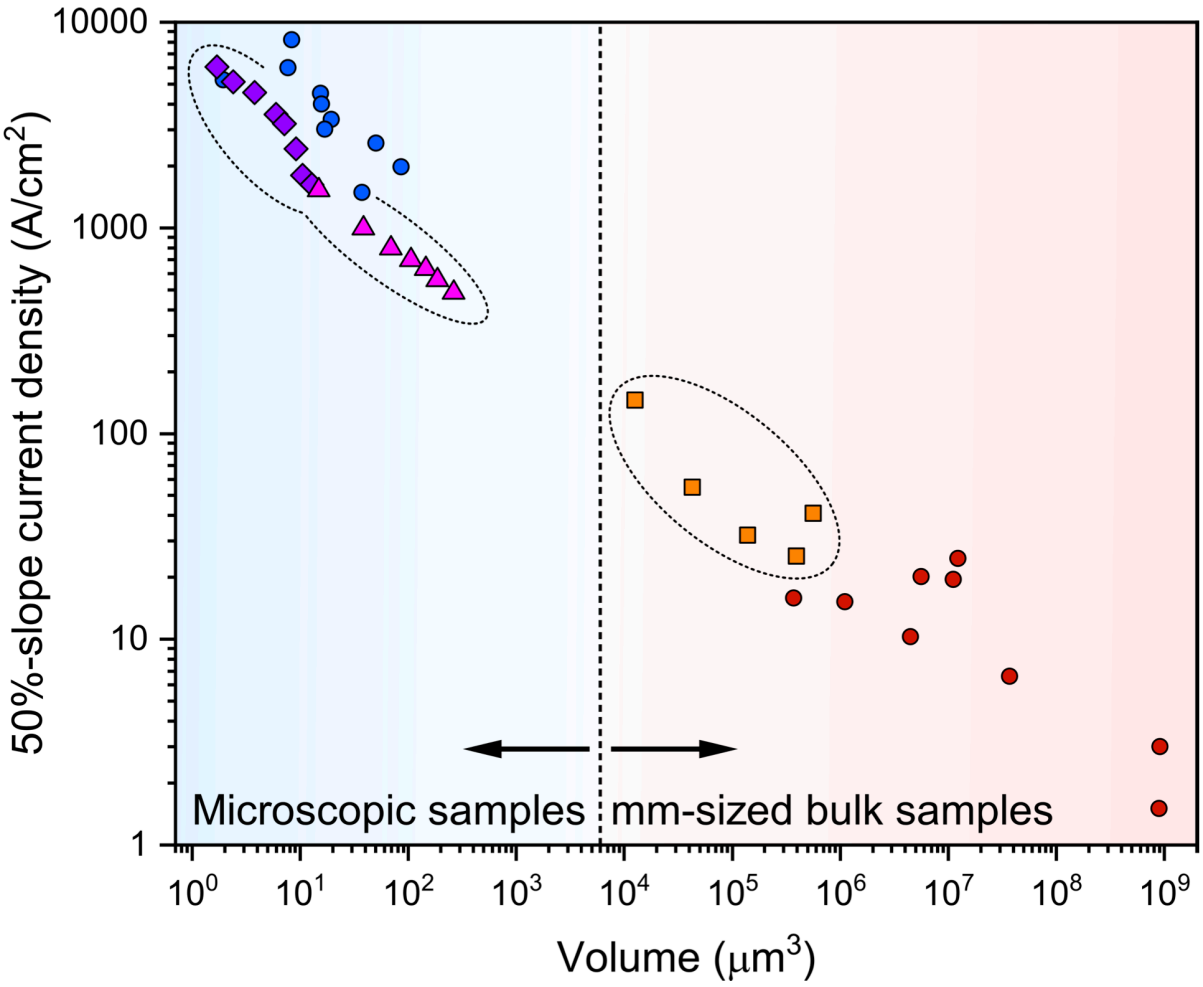

Fig. S5: The Figure of Merit as a function of volume. The FOM as a function of volume for all measured samples at room temperature on a log-log scale. N.B. each circular point corresponds to a single sample. The thinning study samples are depicted with a unique non-circular symbol and a different color. The FOM shows a similar dependence on volume as on the cross-sectional area.

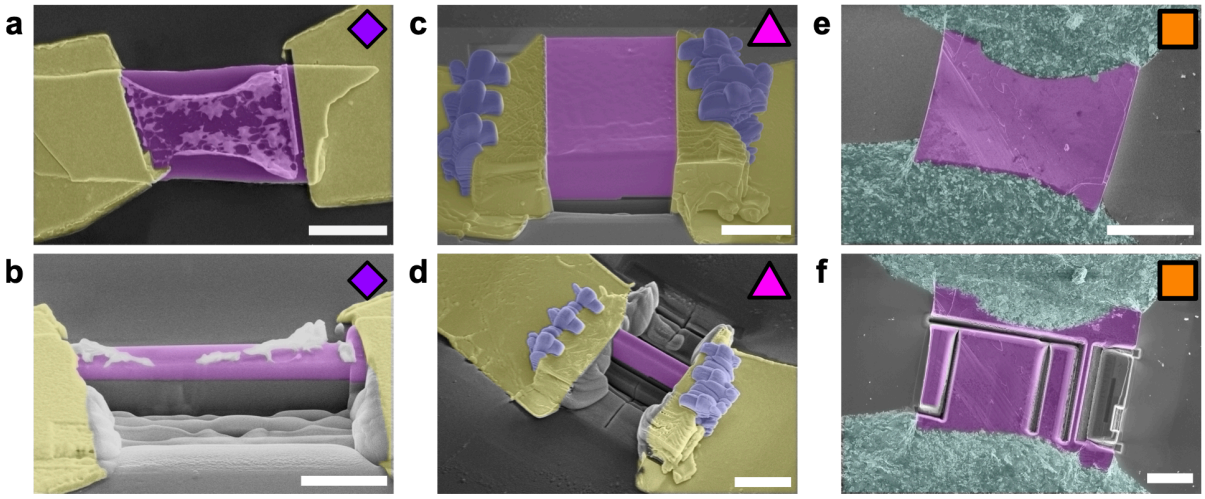

Fig. S6: False colored scanning electron micrographs of samples used for the thinning experiment in different stages of thinning. In all images, purple is used to indicate the crystal and yellow is indicating titanium/gold contacts to the sample. (a) and (b) correspond to the sample indicated by diamond signs in Fig. 3.2(b) of the main text. It covers the smallest size ranges; the scale bars correspond to 3 μm and 2 μm respectively. Some lithography resist residue can be observed in white. The sample depicted in (c) and (d) is covering the intermediate sizes (scale bars are respectively 4 μm and 5 μm long) and is represented by triangles in Fig. 3.2(b) of the main text. Indicated in blue in these images is the electron beam induced deposited tungsten used to strengthen the contacts to the crystal. The third sample of the thinning study is shown in images (e) and (f). It is a relatively small mm-sized bulk sample that is contacted using silver epoxy, which is false colored in light blue. The FOM data of this sample is depicted by red squares in Fig. 3.2(b) in the main text. The scale bars in these images represent 100 μm and 50 μm respectively.

3.5.5 Supplementary Note S5: Reconstructing the $E(J)$-characteristic on basis of Joule heating only

Using analytical differentiation it is possible to calculate $\mathrm{d}E/\mathrm{d}J$ from $E(J)$. Reversely, one can calculate $E(J)$ by integration of $\mathrm{d}E/\mathrm{d}J$. The latter introduces an integration constant that needs to be set by a boundary condition. The boundary condition in our case is the requirement of zero electric field for zero current density: $E(0) = 0$. To summarize:

$$E(J) \xrightarrow{\text{diff.}} \frac{\mathrm{d}E}{\mathrm{d}J}(J) \xrightarrow{\text{int.}} E_{\text{recon.}}(J) + C_{\text{int.}} \xrightarrow{\text{bound. con.}} E_{\text{recon.}}(J) = E(J) \tag{3.4}$$

Here $C_{\text{int.}}$ is the integration constant and $E_{\text{recon.}}$ is the reconstructed electric field from the derivative $\mathrm{d}E/\mathrm{d}J$. As a sanity check, we perform differentiation and integration sequentially on acquired electric field and recover the originally measured data (see Fig. S7(a)).

The resistivity as a function of temperature is measured by calculating the slope of the $E(J)$-characteristic for low currents (*i.e.*, here, the slope of the $E(J)$ is current independent and no local temperature increase is measured). We can therefore interchange the resistivity as a function of temperature for the $\mathrm{d}E/\mathrm{d}J$ as a function of temperature at approximately zero applied current:

$$\rho(T) = \frac{\mathrm{d}E}{\mathrm{d}J}(T, J \approx 0) \tag{3.5}$$

The application of the Pt-thermometer allows us to measure the local absolute temperature as a function of current density in the sample. When the crystal is heated, the resistivity lowers, causing a decrease of $\mathrm{d}E/\mathrm{d}J$ and therefore a decline of the slope of the $E(J)$-characteristic. Since we have both the $\mathrm{d}E/\mathrm{d}J$ as a function of temperature and the temperature as a function of current density available, we can combine these to find the $\mathrm{d}E/\mathrm{d}J$ as a function of the locally measured temperature caused by the application of current density, which we denote as $\mathrm{d}E_{\text{thermal}}/\mathrm{d}J$:

$$\frac{\mathrm{d}E}{\mathrm{d}J}(T, J \approx 0) \;\&\; T(J) \xrightarrow{substitution} \mathrm{d}E_{\mathrm{thermal}}/\mathrm{d}J(J) \tag{3.6}$$

To make this substitution, we fit the measured resistivity as a function of temperature with a 5th order polynomial to capture its phenomenological behaviour (see Fig. S7(b)). Next, we use the fitted function to calculate $\mathrm{d}E_{\mathrm{thermal}}/\mathrm{d}J$, which is depicted in Fig. S7(c). Finally, we apply the above described procedure to reconstruct E_{thermal} using integration, yielding the data that is shown in Fig. 3.3 of the main text and Fig. S7(d).

3.5.6 Supplementary Note S6: Details of the Comsol simulations and the homogeneity of the local temperature

Since the resistance of the platinum thermometer is determined by its average temperature, our thermometry technique might be insensitive to local temperature inhomogeneity in the sample. Furthermore, due to the thermal coupling of the platinum leads to the substrate, a temperature difference might exist between the Pt and the part of the crystal that is most effected by heating. In order to eliminate these concerns, we have carried out thermal simulations in Comsol multiphysics version 5.4.

We consider the geometry displayed in Fig. S8(b), which is a true to size model of the sample shown in Fig. 3.1(a) of the main text. First, we assume that power is only dissipated in the part of the crystal between the gold contacts (*i.e.*, not in the parts covered by gold). The input power is calculated from the product of current and voltage, taken from transport measurements (see Fig. S8(a)). Next, we assume that the substrate temperature is constant 50 μm away from the crystal. Using these two boundary conditions, we solve for a steady state solution where the temperature of the geometry is constant. The results of these simulations are governed by the thermal conductivity of the materials. Terasaki et al. have evaluated the in- and out-of-plane thermal conductivity of Ca214 to be 5.1 W/mK and 1.8 W/mK respectively [65].

In the main text, we report that the Pt-sensor is an accurate measure for the average sample temperature. Fig. S8(c) and S8(d) give an overview of the temperature variations within the sample at the FOM current density. Here, the temperature increase is plotted as a function of a vertical and horizontal line cut respectively. The temperature increases roughly quadratically from the sides of the crystal towards the hottest point of the flake. The temperature

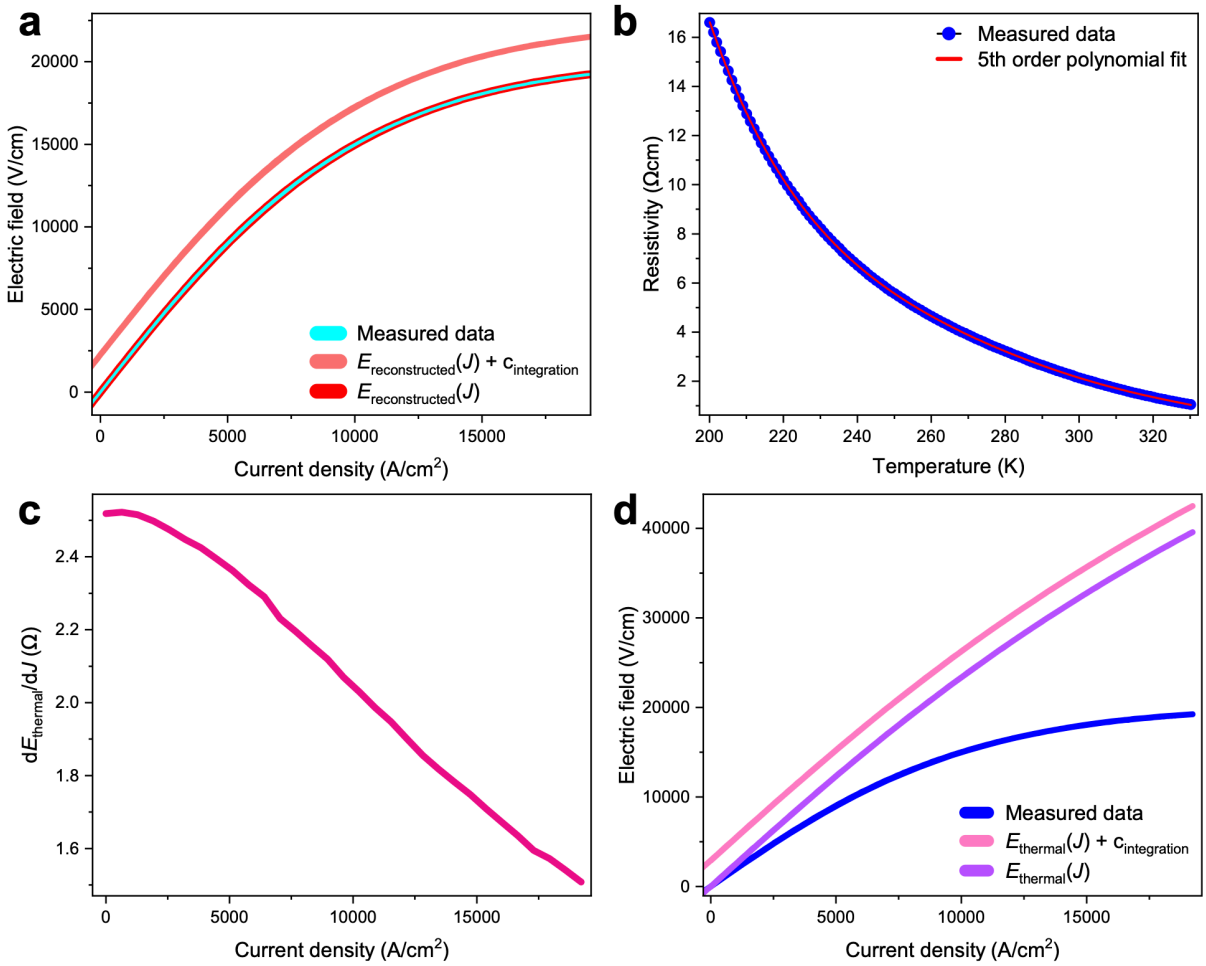

Fig. S7: Summary of calculating E_{thermal}. As a sanity check, we perform subsequent differentiation and integration of a dataset and retrieve the original measured data, which is depicted in (a). (b) shows the resistivity versus temperature curve measured on a sample with embedded Pt-thermometer. The data is fitted by a 5th order polynomial to capture its phenomenological behaviour. This fit is used to find the $\mathrm{d}E_{\mathrm{thermal}}/\mathrm{d}J(J)$ (shown in (c)), which is integrated to retrieve E_{thermal} (shown in (d) and Fig. 3.3 of the main text).

variations in the flake were found to be lower than 3 K at the FOM.

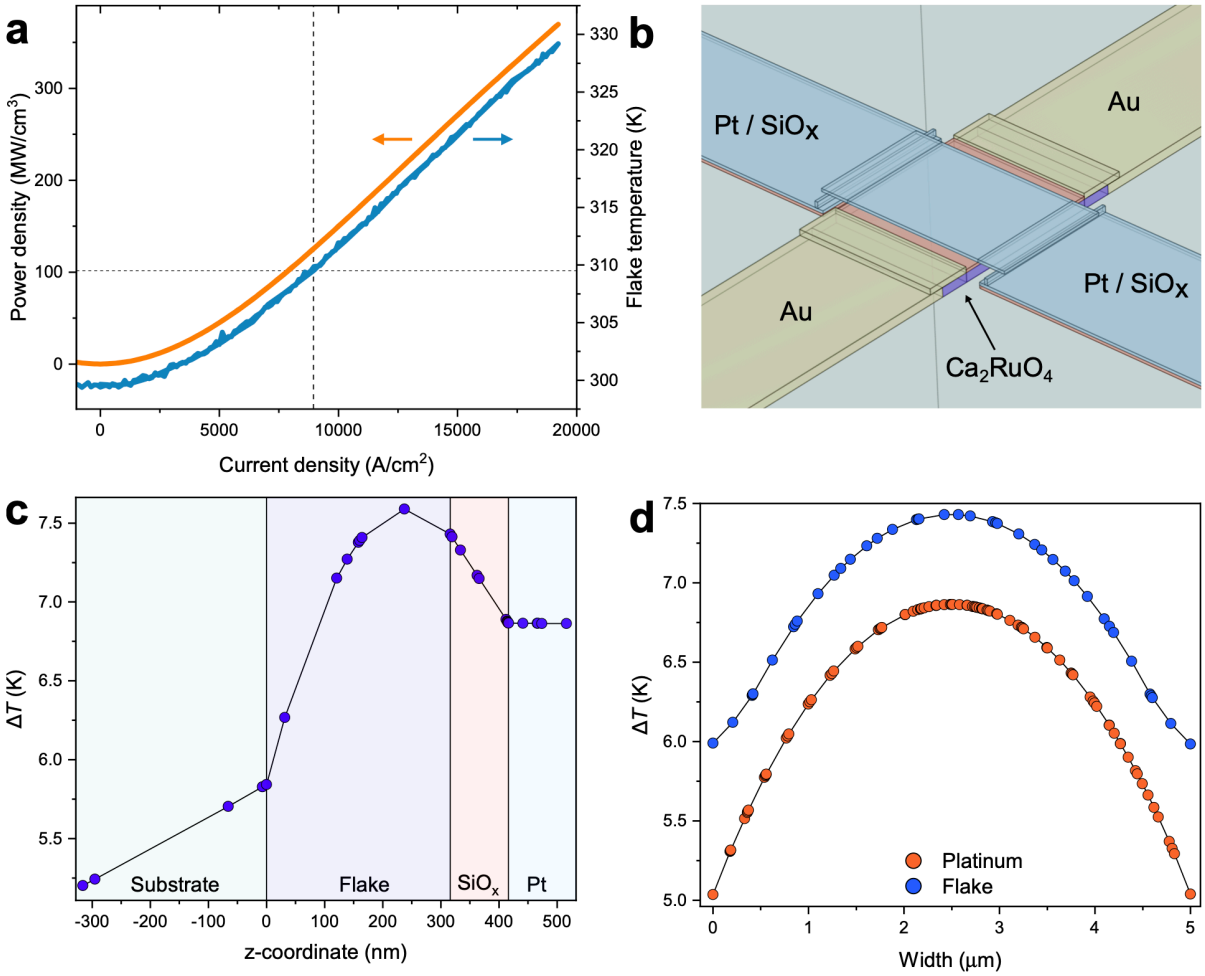

Fig. S8: Temperature inhomogeneity in the Comsol simulations. (a) displays the power density calculated from the transport data together with the measured local sample temperature. There is a one to one correspondence of the local temperature to the power density, giving a strong indication that we are measuring the local sample temperature. The dissipated power is used as input data for the simulations. (b) Shows a schematic overview of the different elements simulated. Each color corresponds to the labeled material. (c) depicts the temperature increase $\Delta T = T_{\text{flake}} - 300$ K along a vertical line cut through the center of the substrate, flake and thermometer, at the FOM current density. The different parts of the sample are labeled by the same colors as in (b). The temperature variations along a horizontal line cut parallel to the Pt-thermometer leads, at the FOM current density, are displayed in (d).

3.5.7 Supplementary Note S7: Minimal model for current density inhomogeneity over the cross-sectional area

As described in the main text, the cross section dependence might be explained by an inhomogenous current density distribution throughout the

cross-sectional area. Here we present a minimal toy model, and phenomenologically compare it to the measured data.

Crucial in this analysis is the difference between the *apparent* current density, namely the total current (I) divided by the total cross-sectional area (A):

$$J_{\text{app}} = I/A \tag{3.7}$$

and the *actual* current density that might be dependent on parameters describing the cross-sectional area:

$$J_{\text{act}} = \frac{\mathrm{d}I}{\mathrm{d}A}(t, w) \tag{3.8}$$

Where t (w) is a length parameter that runs between $-T/2$ ($-W/2$) and $T/2$ ($W/2$), with T (W) the thickness (width) of the crystal. The actual and apparent current density can be related to each other by integrating the actual current density to find the total current:

$$J_{\text{app.}} = I/A = 1/A \iint \frac{\mathrm{d}I}{\mathrm{d}A}(t, w)\mathrm{d}A \tag{3.9}$$

Therefore a homogeneous current distribution (*i.e.*, a constant actual current density) yields an equal apparent current density:

$$J_{\text{act.}} = J_0 \rightarrow J_{\text{app}} = 1/A \iint J_0 \mathrm{d}A = \frac{AJ_0}{A} = J_0 = J_{\text{act.}} \tag{3.10}$$

Now we can examine what type of actual current density features the power law dependence on the cross-sectional area that is observed in the measured current density (displayed in Fig. 3.2(b) of the main text). To do so we assume that the actual current density decreases as l^{-a}, where a is a constant and l is the distance from the edges of the sample. This means, for a rectangular cross-section, that the total current is given by:

$$I = 4 \int_0^{T/2} \int_0^{W/2} \frac{\mathrm{d}I}{\mathrm{d}A}(t, w) \mathrm{d}t \mathrm{d}w \tag{3.11}$$

Here we used the fact that the system is symmetric in four sectors. Each of those can be divided in two parts:

$$I = 4 \left[\int_0^{T/2} \int_0^{\frac{W}{T}t} w^{-a} \mathrm{d}w \mathrm{d}t + \int_0^{w/2} \int_0^{\frac{T}{W}w} t^{-a} \mathrm{d}t \mathrm{d}w \right] \tag{3.12}$$

Leading to:

$$I = \frac{4}{(1-a)(2-a)} \left[\left(\frac{T}{W}\right)^{1-a} \left(\frac{W}{2}\right)^{2-a} + \left(\frac{W}{T}\right)^{1-a} \left(\frac{T}{2}\right)^{2-a} \right] \tag{3.13}$$

Where we assumed $a \neq 1$. This can be simplified to:

$$I = \frac{8}{(1-a)(2-a)} (TW)^{1-a} = \frac{8}{(1-a)(2-a)} A^{1-a} \tag{3.14}$$

That entails for the apparent current density:

$$J_{\text{app.}} = I/A = \frac{8}{(1-a)(2-a)} \frac{A^{1-a}}{A} = \frac{8}{(1-a)(2-a)} A^{-a} \sim A^{-a} \tag{3.15}$$

Which is the observed power law dependence of the measured current density.

Chapter 4

Unconventional Features of Non-Centrosymmetric Superconductors

4.1 Theoretical Aspects

Since its discovery (110 years ago), superconductivity has aroused enormous interest in the scientific community. Indeed, over the years, the research on superconductivity has given rise not only to applications impossible to achieve without superconductors but also to the microscopic understanding of this intriguing macroscopic quantum effect. Nowadays, the best microscopic theory that explains superconductivity is the work of Bardeen, Cooper and Schrieffer [8] (BCS theory) which explains superconductivity as the formation of a macroscopic coherent state of Cooper pairs formed by conduction electrons. Indeed, in the BCS theory the interaction that enables the electrons to pair results from the electron-phonon coupling. This kind of interaction requires the electrons to develop Cooper pairs in their most symmetric way, usually termed the "s-wave" channel, and thus the corresponding pair wavefunction has even parity.

To see all the possible symmetry configurations of the wavefunction, let's consider 2 fermions having $(\mathbf{r_1}, \mathbf{r_2})$ as spatial coordinates and (σ_1, σ_2) as spin coordinates respectively. If the total hamiltonian of this system can be written as the sum of a piece dependent only by spatial coordinates plus one dependent only by spin coordinates, namely

$$H = H(\mathbf{r_1}, \mathbf{r_2}) + H(\sigma_1, \sigma_2) \tag{4.1}$$

then the wavefunction of the system could be factorized and thus written as follow

$$\Psi(\mathbf{r_1}, \mathbf{r_2}, \sigma_1, \sigma_2) = \Phi(\mathbf{r_1}, \mathbf{r_2})\chi(\sigma_1, \sigma_2) \tag{4.2}$$

To satisfy the Pauli principle, the wavefunction (4.2) must be fully antisymmetric

$$\Psi(\mathbf{r_1}, \mathbf{r_2}, \sigma_1, \sigma_2) = \Psi(\mathbf{r_2}, \mathbf{r_1}, \sigma_2, \sigma_1) \tag{4.3}$$

Now, if the parity, P, and the time reversal, T, are conserved, that is to say the commutators $[H, \mathsf{P}] = 0$ and $[H, \mathsf{T}] = 0$, then

$$\mathsf{P}\Psi(\mathbf{r_1}, \mathbf{r_2}, \sigma_1, \sigma_2) = \pm\Psi(\mathbf{r_1}, \mathbf{r_2}, \sigma_1, \sigma_2) \tag{4.4}$$

$$\mathsf{T}\Psi(\mathbf{r_1}, \mathbf{r_2}, \sigma_1, \sigma_2) = \Psi(\mathbf{r_1}, \mathbf{r_2}, \sigma_1, \sigma_2) \tag{4.5}$$

In this conditions the wavefunction, Ψ, can be classified as in the Table 4.1. Superconductors based on the pairing configuration of the first line in the Table 4.1 are called "conventional". They are well described in the BCS theory. Putting electron-phonon coupling aside for a moment could open the opportu-

Table 4.1: Possible symmetries of the wavefunction.

$\Phi(\mathbf{r_1}, \mathbf{r_2})$	$\chi(\sigma_1, \sigma_2)$
Even	**Odd**
s-wave l=0, d-wave l=2,...	spin-singlet S=0
	$\frac{1}{\sqrt{2}}[\lvert\uparrow\downarrow\rangle - \lvert\downarrow\uparrow\rangle]$
Odd	**Even**
p-wave l=1, f-wave l=3,...	spin-triplet S=1
	$\lvert\uparrow\uparrow\rangle$
	$\frac{1}{\sqrt{2}}[\lvert\uparrow\downarrow\rangle + \lvert\downarrow\uparrow\rangle]$
	$\lvert\downarrow\downarrow\rangle$

nity for alternative pairing mechanisms driven by electron-electron coupling, e.g. spin fluctuation exchange. These interactions are usually longer-ranged and allow for other pairing channels with higher angular momentum. This is

the case of superconductors based on the pairing configuration of the second line in the Table 4.1 that are called "unconventional".

Therefore, pairing states may be distinguished by even and odd parity. Furthermore, the totally antisymmetric Cooper pair wavefunction, requested by the Pauli principle, imposes the condition that even parity is tied to the spin-singlet and odd parity to the spin-triplet configuration. Triplet superconductors open a new world in the Physics of superconductivity since they add the spin as a new degree of freedom. This makes them more exciting and interesting than singlet superconductors. Unfortunately, there are still few experiments that confirm spin-triplet superconductivity.

However, we emphasize that this classification relies (according to Anderson's theorem) on the presence of an inversion centre in the crystal structure, as to have the parity as a proper quantum number and, in addition, the time-reversal symmetry. Nevertheless, there is a class of superconductors where the crystal structure lacks a centre of inversion and the above classification does not hold anymore. These superconductors go by the name of non-centrosymmetric superconductors (NCS). In this case, the hamiltonian of the system does not commute with the parity, $[H, \mathsf{P}] \neq 0$. This means that the parity is no longer a good quantum number, and we cannot choose a common base for P and H. As a consequence, we cannot classify the wavefunction with the eigenstates of P as in the Table 4.1.

The discovery of bulk superconductivity in the heavy fermion compound $CePt_3Si$, that has not inversion symmetry, by Bauer et al. [77] appeared quite surprising and attracted great interest, since signatures of a singlet, as well as a triplet order parameter, were observed in different response and transport measurements [78]. The resolution of this inconsistency was pointed out by Frigeri et al. [79, 80]: the loss of the inversion symmetry introduces a special form of spin-orbit coupling, the so-called antisymmetric spin-orbit coupling (ASOC), which invalidates the classification of the superconducting order parameter for spin-singlet/even parity and spin-triplet/odd parity leading to the spin splitting of the electronic states at the Fermi level. This may give rise to a mixture of spin-singlet and spin-triplet pairing states in the superconducting wavefunction. This mixed pairing leads NCS to display significantly different properties from conventional superconducting systems. Indeed, NCS can exhibit a variety of unconventional properties, for instance, magneto-electrical effects, multigap behaviour, large upper critical fields (exceeding the Pauli limit) [81–83], helical vortex-state, nodes in the superconducting gap, non-

trivial topological effects and time-reversal symmetry breaking (TRSB) [84]. These extensive exotic behaviours in NCS are fundamental to investigate since they could even support the development of a new technological era.

Recently, non-centrosymmetric heavy fermion superconductors have attracted great interest due to the above mentioned unconventional behaviour observed in these strongly correlated electron materials [77,85,86]. Indeed, the effect of strong electron correlations and spin fluctuations are responsible for the observation of unconventional superconductivity in these systems [84,87].

On the other hand, due to the absence of magnetic correlations, the weakly-correlated electron systems, like Nb_xRe_{1-x} [88], $LaNiC_2$ [89], $Li_2(Pd, Pt)_xB$ [90, 91], (Rh, Ir)Ga_9 [92] etc., are particularly promising for studying the unconventional superconductivity in NCS. Indeed, these systems generally exhibit weak electron correlation effects and lack the magnetic complexities arising from the f-electron rare-earth heavy fermions. This makes the matter easier to explore the ramifications of inversion symmetry breaking and thus isolate the salient features of ASOC-mediated superconductivity [93–97]. However, most of the weakly-correlated electron systems appear to show s-wave behaviour, albeit, in some cases, they also show unconventional signatures, for example, nodal superconducting gap structure [84,98,99] and TRSB. It is clear that the role of lacking inversion symmetry on the superconducting pairing states remains a fundamentally open question. Therefore, it is highly desirable to shed light on the electrons pairing mechanism in NCS and thus get insight into the role of the ASOC. In this regard, the possibility to produce NCS in thin-film form could be very useful. Indeed, the availability of NCS thin films may allow one to sketch dedicated transport experiments that could benefit from the well established lithographic techniques (e.g. Electron Beam Lithography, Focused Ion Beam Lithography, etc.). That allows one to manage the design of a sample in any geometric configuration giving access to unprecedented experiments and thus get more insight into the unconventional nature of the NCS. For these reasons, we considered the system Nb_xRe_{1-x} exploiting both its feasibility in a thin film form and its weakly-correlated electron nature.

4.2 NbRe

In this section, we focus on NCS $Nb_{0.18}Re_{0.82}$ (hereafter NbRe) since can be a potential candidate for having a nonconventional superconducting order

parameter. The NbRe is a phonon-mediated type-II superconductor that has the bulk transition temperature, $T_c \sim 8.8$ K [88, 100]. Looking into the literature, it comes out that it is a weakly-correlated electron system and magnetic correlations are also absent, which makes this system a good playground to investigate the role of ASOC. Moreover, it is observed that the upper critical field, Hc_2, in this material reaches the Pauli limit, which points out the possibility of unconventional pairing [88, 101].

The structural phase (χ phase) of the NbRe is cubic, with space group I-43m, and includes 58 atoms in its unit cell that involve four crystallographically different sites (see Fig. 4.1). Since Re is a heavy element, the effect of the ASOC is expected to be strong in the low Nb percentage regime. This would give an opportunity for searching the existence of a mixture of the spin-singlet and spin-triplet states in this compound. However, the results observed on polycrystalline bulk samples are controversial [88, 100, 101], while a recent investigation [102] conducted by combining Andreev point contact spectroscopy and heat capacity measurements on high-quality NbRe single crystals [103] shows the appearance of two superconducting gaps, even though it has been asserted that there are a variety of different situations based on mixed spin singlet-triplet pairing that may also explain these observations [102]. Moreover, in a recent work by T. Shang et al., TRSB in NbRe has been observed. This result is suggestive of unconventional superconductivity in this system. In summary, various superconducting properties in NbRe, for instance, upper

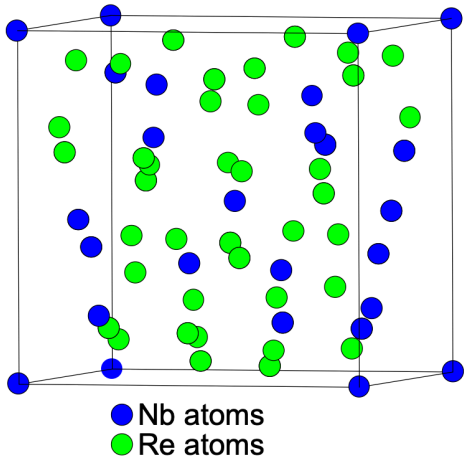

Fig. 4.1: Crystalline structure of NbRe.

critical field [88,101], energy gap behaviour [102] and TRSB [104], are not well described within the conventional BCS theory. Therefore, further investiga-

tions on this material to clarify its unconventional nature in terms of pairing symmetry and physical features are required. In this respect, phase-sensitive experiments of the pairing state could give important informations to clarify the pairing symmetry.

4.3 NbRe Little-Parks Experiment

As we have seen, in superconductors with inversion symmetry, the parity symmetry imposes a constraint on the pairing state, which must be either spin-singlet with even parity or spin-triplet with odd parity. For noncentrosymmetric superconductors, on the other hand, the broken parity symmetry is expected to give rise to an admixture of spin-triplet and spin-singlet pairing states. However, experimental confirmation of pairing mixing in any material remains elusive. A suitable way to probe the presence of spin-triplet components in the pairing state of a given material is represented by phase-sensitive measurements [105]. In ordinary superconductors with wave function $\Psi_S = |\Delta_S| e^{i\theta}$ the single-valuedness of Ψ_S requires that the phase of the superconducting order parameter can change only by multiples of 2π along any closed contour. As a consequence, the magnetic flux through a multiply connected superconducting body is quantized in discrete units of $\Phi_0 = hc/2e$, where h is the Planck constant, c is the speed of light, and e is the elementary charge. The observations of the fluxoid quantization served indeed as the first experimental verifications of the BCS theory of conventional superconductors [106–108].

Shortly after the initial magnetometry measurements, Little and Parks further demonstrated oscillations of the superconducting transition temperature T_c as a function of the applied magnetic flux which results from the corresponding periodicity of the free energy of the superconducting state [109]. The minimum of the free energy, or the maximum of the T_c, is achieved when the applied magnetic flux takes the form $\Phi = n\Phi_0$, where n is an integer number. In the following decades, the Little-Parks (LP) effect, as a stringent test for the electron pairing, has been observed in numerous superconducting materials [110–112].

In the case of the spin-triplet pairing state, the gap function has odd parity, i.e., $\Delta_k = -\Delta_{-k}$. As a consequence, a sign change can occur at certain crystalline grain boundaries, inducing an additional π phase shift which is responsible for half-quantum flux (HQF) of $\Phi' = (n + 1/2)\Phi_0$ [113]. The

realization of HQF depends on the total number of crystalline grain boundaries that produce such π phase shift, or π junctions [105, 113, 114]. Over the circumference of a ring, only an odd number of π junctions would produce a net phase change of π, which leads to a HQF-hosting π ring. For an even number of π junctions where the total phase changes add up to 2π, the loop would show integer flux quantization, or a 0 ring.

The distinctive experimental signature of HQF in π rings and 0 rings can be particularly powerful in determining the presence of spin-triplet components in polycrystalline rings of unconventional superconductors [114], and in particular in non-centrosymmetric superconductors such as NbRe [9]. For this reason, we performed LP experiment on NbRe thin films. In the following we show the preliminary results obtained.

4.3.1 Experimental details

NbRe thin film

NbRe thin film[1] of thickness $\mathtt{t} = 100$ nm was sputtered on Si(100) substrate. The fabrication was performed employing a UHV dc diode magnetron sputtering system from a $Nb_{0.20}Re_{0.80}$ 99.9 % pure target. After reaching the base pressure of the sputtering system (10^{-9} mbar regime), the deposition was carried out holding the substrate at room temperature in an Ar pressure of 3.5 μbar at a deposition rate of 0.33 nm/s. The Nb concentration of the obtained sample was found to be $x = 0.18$ as estimated by energy dispersive spectroscopy. Consequently, the resulting concentration of the NbRe film is close to the optimal one in terms of superconducting transition temperature in the case of bulk samples [101].

NbRe micro bridge fabrication and characterization

Starting from a single film of NbRe, prepared as described above, we used the FIB lithography to obtain a micro-bridge. As already mentioned, this method provides a highly precise and versatile nanostructuring that can be depicted as "cutting" the desired structure by shooting ions at a specimen to mill away the surrounding material. Fig. 4.2 shows a schematisation of the NbRe film and the FIB together with an actual picture of the lithography

[1] Thin films of NbRe were obtained for the first time at the superconducting laboratory of the University of Salerno [115].

FIB system we used at *Leiden University–Netherlands Centre for Electron Nanoscopy.*

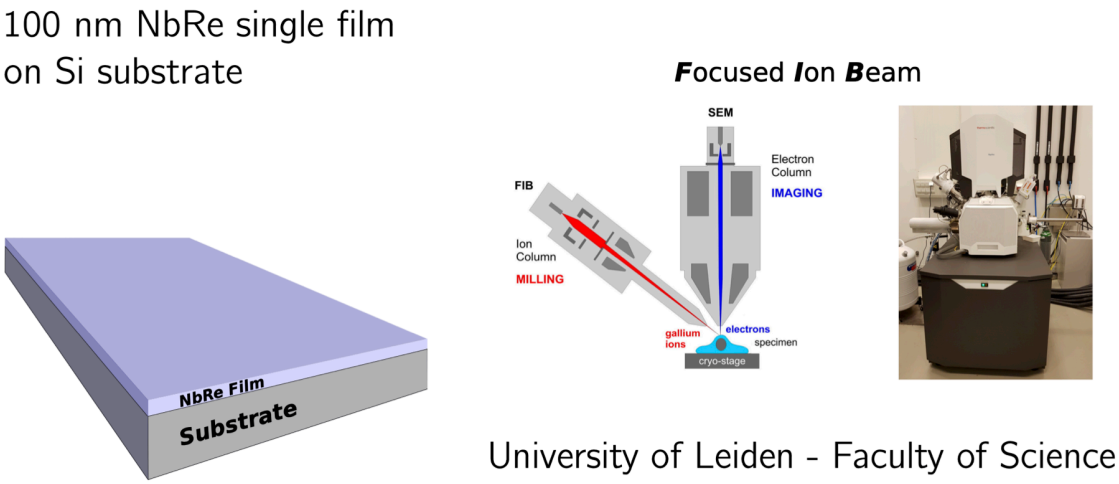

Fig. 4.2: Schematisation of the NbRe film on Si substrate and the focused ion beam. The picture is the actual lithography FIB system used at *Leiden University–Netherlands Centre for Electron Nanoscopy.*

Fig. 4.3 summarises the main four steps we followed to shape the micro-bridge with the contact pads and the wires (the black lines are the milled part). In particular, panel (a) shows the "sculpted" contact pads, panel (b) and (c) the wires, and panel (d) the micro-bridge of about 3.3 μm wide and 6 μm long. In order to ensure that the superconducting properties of the NbRe remained unaltered after the lithographic process, and to estimate the parameters needed for LP experiment, we have acquired both the $R(T)$ curve at zero field and with different magnetic field applied perpendicularly to the micro-bridge plane with a bias-current $I_b = 5$ μA (see Fig. 4.5). In this way, we obtained the T_c and estimated the upper critical field $\mu_0 H_{c2}$ of the micro-bridge, respectively. The Fig. 4.4 shows the superconducting transition of the micro-bridge. The T_c, defined as the temperature at which the resistance is half of the one measured at $T = 10$ K, is $T_c = 6.8$ K. Furthermore, we obtained the T_c values from the $R(T)$ curves acquired at different magnetic field applied. These T_c values are highlighted by blue solid circles in Fig. 4.5 and reported in Fig. 4.6 as a function of the magnetic field. The solid black line is the best fit to the data obtained by using a linear relation that allows to extrapolate the upper magnetic field at $T = 0$, $\mu_0 H_{c2}(0) = (14.6 \pm 0.7)$ T. Moreover, with the assumption of a linear dependence of the perpendicular upper critical field, it is also possible to

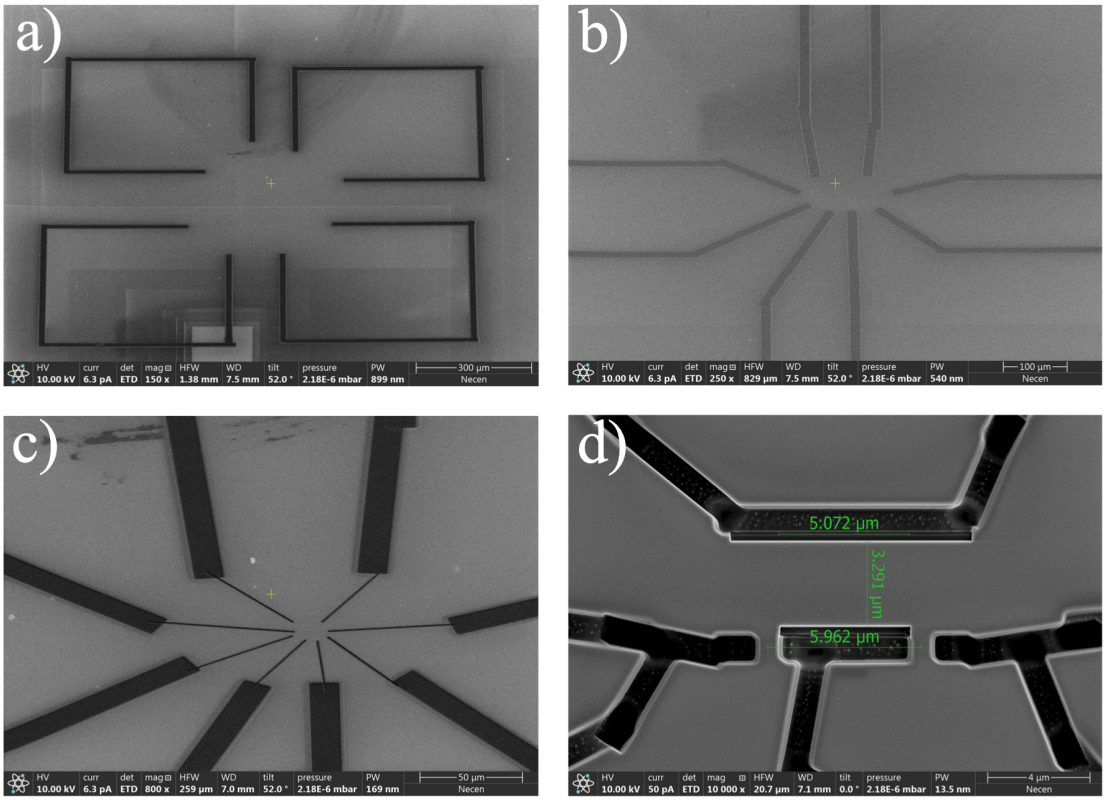

Fig. 4.3: SEM images acquired during the micro-bridge structuring. In particular, panel (a) shows the contact pads, (b) the wires, (c) the smaller wires, and (d) the micro-bridge.

evaluate the superconducting coherence length, since $\mu_0 H_{c2} = \Phi_0/2\pi\xi(0)^2$ where $\Phi_0 = 2.07 \times 10^{-15}$ Wb is the flux quantum [116]. Adopting this relation we have $\xi(0) = 4.7$ nm. Therefore, the values of T_c, $\mu_0 H_{c2}$, and $\xi(0)$ estimated are in reasonable accordance with the literature [88, 115], thus this analysis ensure the good quality of the NbRe nano-bridge. Finally we want to point out to the reader that since the LP oscillations are ruled by the following equation

$$T_c(H) = T_{c0}\left[1 - \frac{\pi^2}{3}\left(\frac{\omega\xi(0)\mu_0 H}{\Phi_0}\right)^2 - \frac{\xi^2(0)}{R^2}\left(n - \frac{\Phi}{\Phi_0}\right)^2\right] \tag{4.6}$$

having the value of $\xi(0) = 4.7$ nm means that the amplitude of LP oscillations are expected to be a factor 100 smaller than in for example Sr214 or β-PdBi [114, 117].

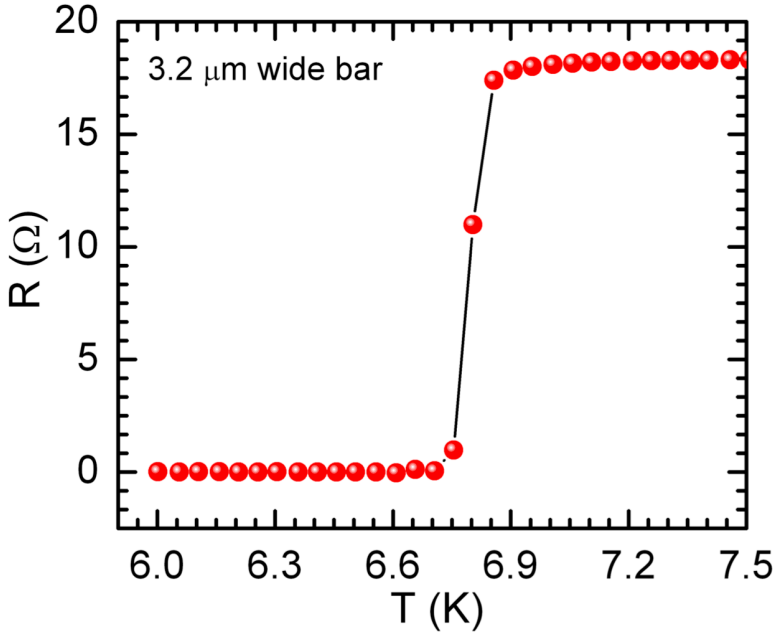

Fig. 4.4: Resistance as a function of temperature of the micro-bridge. The resistive transition is quite sharp, and the T_c, defined as the temperature at which the resistance is half of the one measured at $T = 10$ K is $T_c = 6.8$ K.

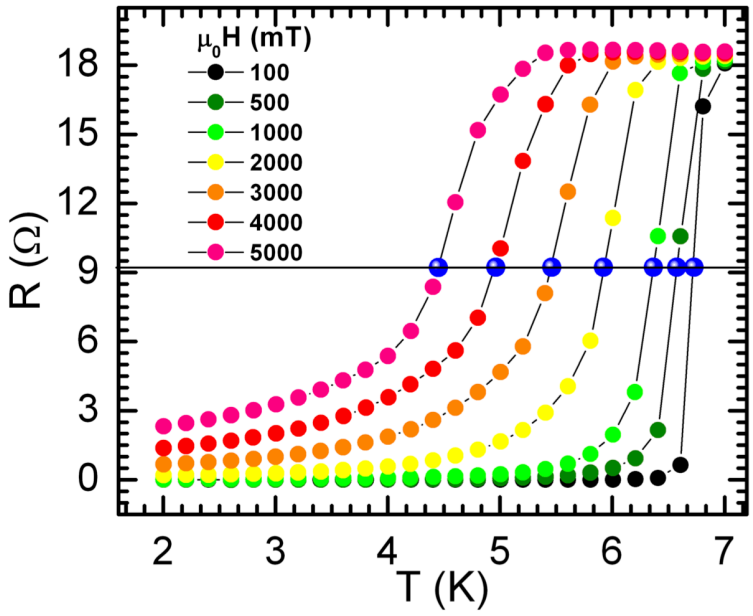

Fig. 4.5: Resistive transitions of the micro-bridge at different magnetic field. The T_c values, defined as the temperature at which the resistance is half of the one measured at $T = 10$ K, are identified by the interception of the horizontal line with the curves, and highlighted by blue solid circles.

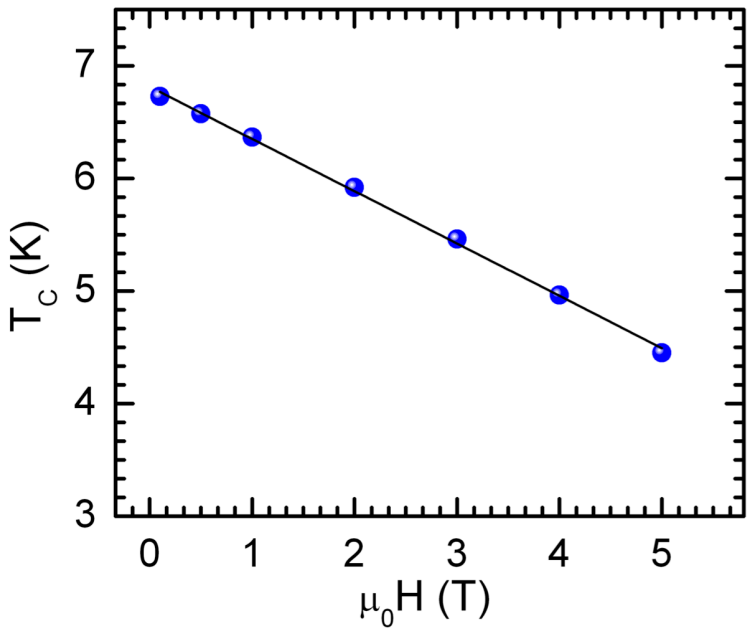

Fig. 4.6: T_c values as a function of the magnetic field. The solid black line is the best fit to the data obtained by using a linear relation to extrapolate $\mu_0 H_{c2}(0)$.

4.3.2 Results and discussion

Exploiting the potentialities of the FIB lithography, we fabricated an array of rings, cutting them out of the micro-bridge. This array, shown in Fig. 4.7(a), is made up of 27 rings in series. This way, the expected LP oscillations in the rings get added in series, and the signal becomes larger. Moreover, supposing that half of the rings are π-rings, then they will be added to the other half that are 0-rings. This means that assuming the crystalline orientations of the grains are random, we would expect to see oscillations of HQF in this specific sample geometry if there is any triplet pairing channel. We designed each ring (in Fig. 4.7(b) is reported a representative one) to have a field periodicity of about 50 Oe. For this purpose, the geometric dimensions (see Fig. 4.8) have been estimated by using the following equation $\Phi_0 = \pi R^2 \mu_0 H$, where Φ_0 is the magnetic flux quantum, $R^2 = R_1 R_2$ is the product of inner and outer loop radius, and μ_0 is the vacuum permeability. We carefully calibrated and focused the ionic Ga^+ beam-current to have high precision and accuracy. Indeed, the whole 27 rings were milled in a single session of 50 minutes by using a beam-current of 1.5 pA at 30 kV. The sample has been measured by using a Physical Property Measurement System (PPMS) by *Quantum Design* in a 4-probe configuration (providing the bias-current by using a Keithley 6221

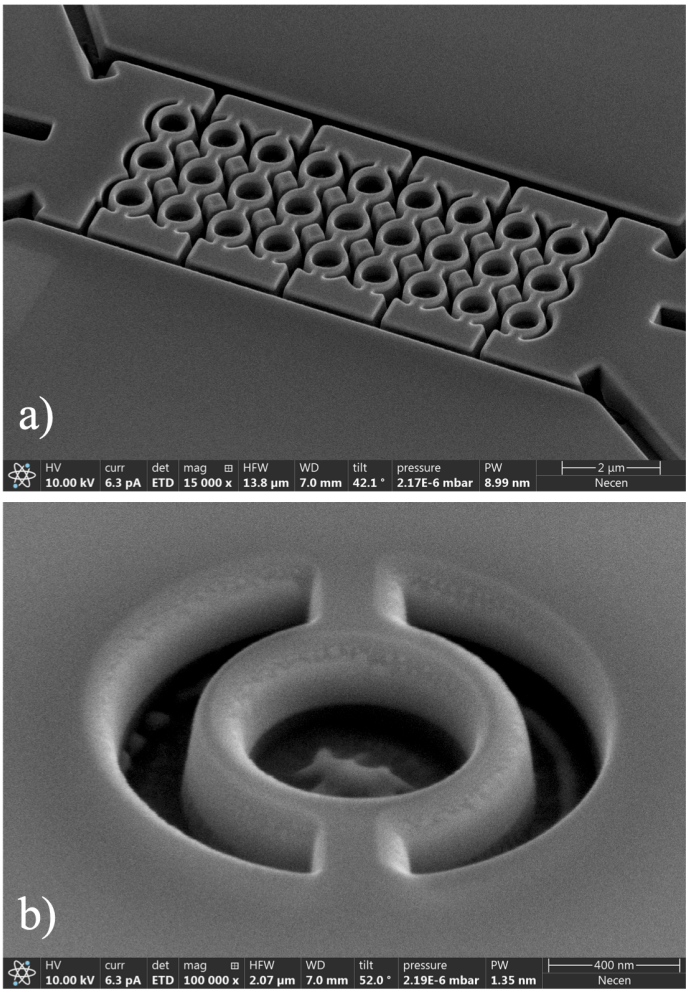

Fig. 4.7: (a) SEM image of the NbRe array of rings. (b) SEM image of a representative ring obtained during the calibration of the patterning parameters.

current source and sensing the sample voltage drop with a Keithley 2182a nanovolt meter). Fig. 4.9 shows the superconducting transition of the ring array at 0, 50, and 100 mT magnetic field applied perpendicularly to the plane of the sample. The broadening of the transition width (∼1.5 K) compared with that of the micro bridge (∼0.2 K, see Fig. 4.4) is typical for submicrometer-sized devices [117, 118]. The LP effect can be observed when the sample is placed at a fixed temperature within the superconducting transition regime where field-induced resistance variations occur. We identified this regime for temperatures around 6.0 K (see inset in Fig. 4.9). However, to investigate the field dependence, it is crucially important to examine V_+ and V_- individually since LP oscillations are not necessarily invariant under reflection. In other words, it is essential to examine magnetovoltage rather

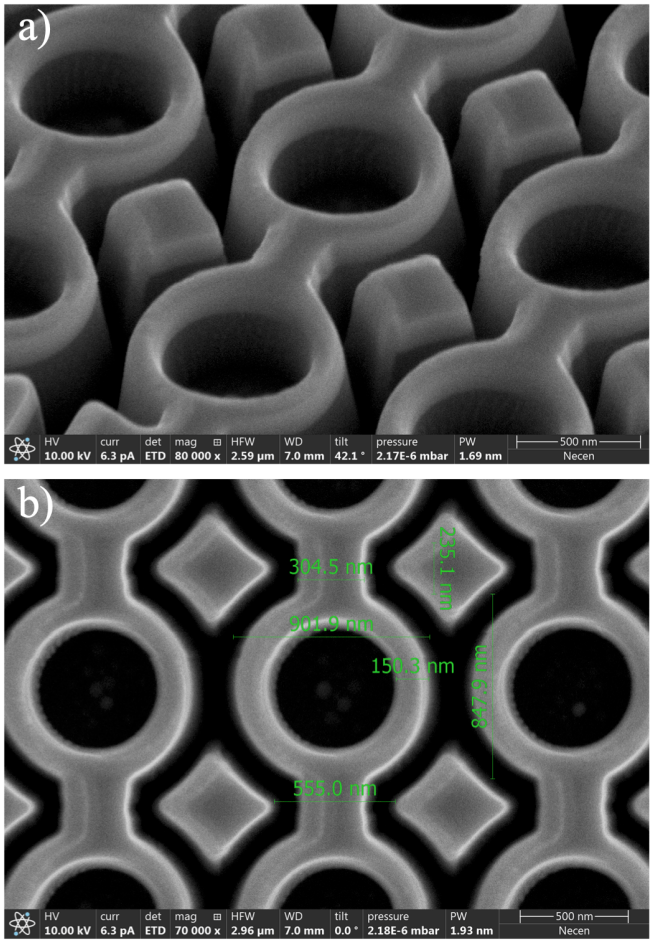

Fig. 4.8: (a) SEM zoomed image of the ring array shown in Fig. 4.7(a). (b) SEM image with the measured geometric parameters of the rings.

than magnetoresistance. Therefore, we chose to acquire IV characteristics as a function of field at $T = 6.02$ K. The protocol used is:

- Setting the temperature to 6.02 K
- Field sweep from 0 to 150 Oe acquiring an IV every 2 Oe
- Warm the sample up to 7 K and oscillate to zero field
- Setting the temperature to 6.02 K
- Repeat the field sweep to -150 Oe acquiring an IV every 2 Oe

This measurement protocol ensures that no vortices are trapped in the rings. The LP oscillations of the NbRe device are shown in Fig. 4.10. The magnetovoltage curves were acquired at different I_b in steps of 2 μA up to ± 12

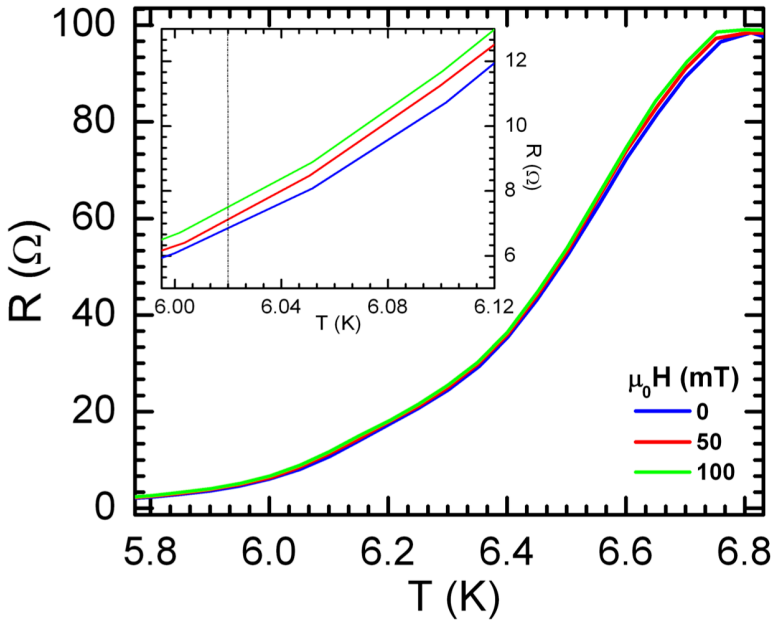

Fig. 4.9: Resistance as a function of temperature of the NbRe device with 0, 50, 100 mT magnetic field applied perpendicularly to the plane of the sample. The inset shows a zoomed image of the superconducting transitions between 6.00 and 6.12 K. The vertical line indicates the temperature at which we performed the measurements.

μA. The oscillations have been observed on a roughly parabolic-shaped background (see Fig. 4.11(b)) that is commonly observed in LP experiments, and it is believed to originate from the misalignment of the magnetic field and the finite line width of the ring.

Zooming in the magnetovoltage curves as in Fig. 4.11, we observed that typical LP oscillations occur for $I_b > 6$ μA (and $I_b < -6$ μA) with an oscillation period of $\sim$45 Oe, slightly lower the expected estimated value. However, for $I_b < 6$ μA (and $I_b > -6$ μA) we still observe oscillations but with a different oscillation period of about $\sim$25 Oe (see Fig. 4.11(a)). Moreover, we note that the magnetovoltage curves are shifted and not fully symmetric respect to the zero field axis. Furthermore, in general, the changing of the oscillation period with the bias-current is unusual in a classic LP experiment.

In the light of these observations, it is still not possible to make any conclusions for the pairing symmetries in NbRe, but these preliminary data show that, albeit the complexity of this experiment, the feasibility is established. Moreover the anomalous behaviour of the magnetovoltage curves suggests that it is important to continue the experiment since these anomalies could

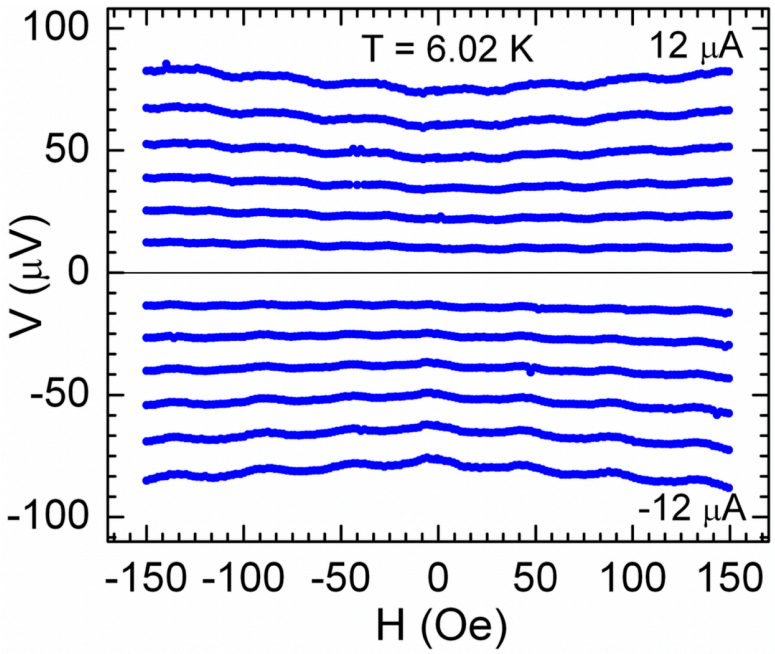

Fig. 4.10: Magnetovoltage curves acquired at $T = 6.02$ K and different bias-current in steps of 2 μA up to ± 12 μA.

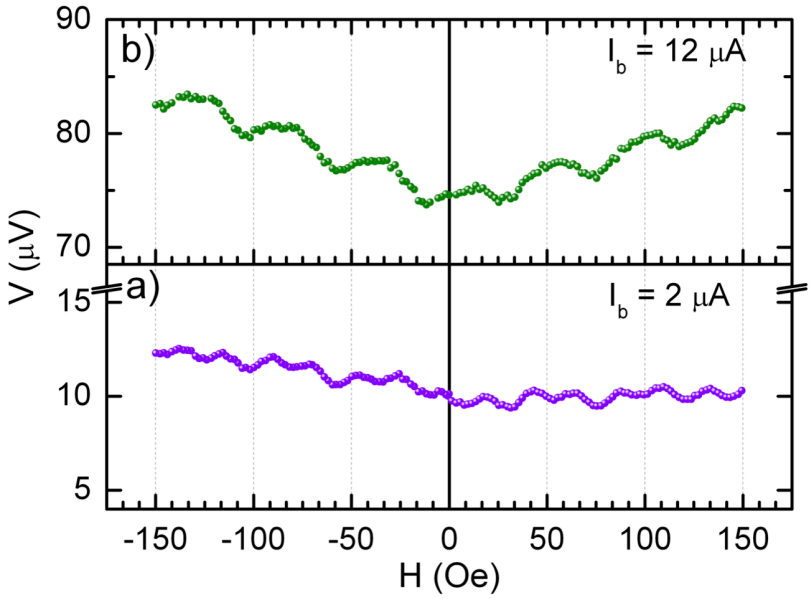

Fig. 4.11: Two representative magnetovoltage curves. (a) Magnetovoltage curve acquired providing a bias-current $I_b = 2$ μA, and (b) $I_b = 12$ μA.

be originated by unconventional superconducting mechanisms in NbRe. Indeed, the same experiment is going to be performed on more samples using the same geometry and also different ones.

Summary

We explored the transport and structural properties of single crystals of the Mott insulator Ca_2RuO_4 in different conditions, namely, tuning its properties acting on different parameters. In particular, by feeding mm-sized samples with a steady-current along the c axis and within the ab plane of the crystal, we measured the correspondent voltage drop in these two configurations, varying the temperature. This measurement protocol allowed us to determine the resistivity as a function of the temperature and current $\rho(J,T)$, as well as the $V(I)$ characteristics at different temperatures in both configurations. Moreover, we combined electronic measurements and x-ray diffraction spectra. Specifically, we acquired the x-ray diffraction patterns while passing the current along the c axis, and within the ab plane of the crystal. By taking advantage of this protocol, it was possible to access a region of the phase diagram not yet explored and to unveil the nucleation and evolution of a metallic crystallographic phase, L', completely compatible with the transport data. Its corresponding cell dimensions depart from those of the insulating short phase and approach those of the metallic long phase. These measurements explain the unexpected and counterintuitive results of the transport data and completely determine the behaviour in the metastable phase (L'). Furthermore, in the configuration where the current is within the ab plane, the x-ray diffraction spectra have been acquired also as a function of the temperature. These measurements show that all the phases (S, S', L', L) are still present in the investigated temperature range, and in particular, the value of the c axis in the metallic phase (L) does not change with temperature and current, enhancing that L is a structurally rigid phase from the elastic point of view. This last analysis is a valuable starting point to get the c axis phase diagram that would allow discerning the conduction states as a function of temperature and current density in the Ca_2RuO_4 single crystals. Additionally, we describe the electrical characterisation of the eutectic sys-

tem Ca_2RuO_4 with embedded Ru inclusions. In this preliminary study, we acquired the resistivity as a function of the temperature at different current-bias, and current-voltage characteristics measured using a current-bias and a voltage-bias. We found qualitatively the same curves observed in the pure Ca_2RuO_4. Here, the very surprising effect we observed is that the sample does not break as in the case of pure Ca_2RuO_4. Our results make this eutectic system valuable and durable. Indeed, it not only conserves the properties of the pure Ca_2RuO_4 but is also a relevant material that could be used for electronic applications more efficiently than the pure one.

Our findings on mm-sized samples are consistent with the literature and represent a significant improvement of the current knowledge of a complex system such as Ca_2RuO_4, and have opened an outlook in its microscopic characterization. For these reasons, we have also performed a detailed study on the size-dependent electrical properties of Ca_2RuO_4 single crystals. Indeed, by using an advanced fabrication method, we were able to obtain μm sized samples with very accurate geometry. We found a surprising relation between crystal size and the current density at which nonlinear conduction occurs, which increases four orders of magnitude when the sample size is reduced from 0.5 mm^2 to 0.5 μm^2. Moreover, employing a local Pt-thermometer fabricated on top of selected microscopic samples, we have established that the observed size dependence is not caused by Joule heating. Our findings indicate an intrinsically inhomogeneous current density distribution in single crystals of Ca_2RuO_4. This requires a re-examination of the relevant role of the electric current in the metastable phase and its possible relation with the insulator to metallic transition. The combination of microscopic samples with a well-controlled geometry and current path, and local platinum temperature probes, pave the way for an innovative approach to study the interplay between thermal and electronic effects, which can be used to study the insulator to metallic transition in Mott insulators.

In the last part of this thesis, we have considered non-centrosymmetric superconductors, with a particular interest in the unconventional nature of these materials that could arise from the lack of an inversion centre in their structure. In particular, we examined the flux quantization in polycrystalline thin-film devices of the non-centrosymmetric superconductor $Nb_{0.18}Re_{0.82}$ since phase-sensitive experiments are unambiguous for distinguishing unconventional effects such as spin-triplet pairing components. In this respect, we have successfully fabricated a $Nb_{0.18}Re_{0.82}$ array of submicrometer-sized rings and

performed Little-Parks experiments. Indeed, the observation of half quantum flux (instead of the integer ones) could be the decisive evidence for the presence of a spin-triplet pairing component in non-centrosymmetric superconductors, where a mixed pairing state is generally expected. Our preliminary data show that, although the complexity of this experiment, the feasibility is established. Moreover, the anomalous behaviour of the magnetovoltage curves acquired suggests to continue the experiment since these anomalies could be originated by unconventional superconducting mechanisms in $Nb_{0.18}Re_{0.82}$. For this reason, this experiment is still in progress at the moment we are presenting this thesis on more samples using the same geometry and different ones.

Bibliography

[1] Jeffrey G. Rau, Eric Kin-Ho Lee, and Hae-Young Kee. Spin-orbit physics giving rise to novel phases in correlated systems: Iridates and related materials. *Annual Review of Condensed Matter Physics*, 7(1):195–221, 2016.

[2] William Witczak-Krempa, Gang Chen, Yong Baek Kim, and Leon Balents. Correlated quantum phenomena in the strong spin-orbit regime. *Annual Review of Condensed Matter Physics*, 5(1):57–82, 2014.

[3] J. Bertinshaw, N. Gurung, P. Jorba, H. Liu, M. Schmid, D. T. Mantadakis, M. Daghofer, M. Krautloher, A. Jain, G. H. Ryu, O. Fabelo, P. Hansmann, G. Khaliullin, C. Pfleiderer, B. Keimer, and B. J. Kim. Unique Crystal Structure of Ca_2RuO_4 in the Current Stabilized Semimetallic State. *Phys. Rev. Lett.*, 123:137204, Sep 2019.

[4] Hengdi Zhao, Bing Hu, Feng Ye, Christina Hoffmann, Itamar Kimchi, and Gang Cao. Nonequilibrium orbital transitions via applied electrical current in calcium ruthenates. *Phys. Rev. B*, 100:241104, Dec 2019.

[5] Ryuji Okazaki, Kensuke Kobayashi, Reiji Kumai, Hironori Nakao, Youichi Murakami, Fumihiko Nakamura, Hiroki Taniguchi, and Ichiro Terasaki. Current-induced giant lattice deformation in the Mott insulator Ca_2RuO_4. *Journal of the Physical Society of Japan*, 89(4):044710, 2020.

[6] M. Ge, T. F. Qi, O. B. Korneta, D. E. De Long, P. Schlottmann, W. P. Crummett, and G. Cao. Lattice-driven magnetoresistivity and metal-insulator transition in single-layered iridates. *Phys. Rev. B*, 84:100402, Sep 2011.

[7] H. Zheng, W. H. Song, J. Terzic, H. D. Zhao, Y. Zhang, Y. F. Ni, L. E. DeLong, P. Schlottmann, and G. Cao. Observation of a pressure-induced transition from interlayer ferromagnetism to intralayer antiferromagnetism in $Sr_4Ru_3O_{10}$. *Phys. Rev. B*, 98:064418, Aug 2018.

[8] J. Bardeen, L. N. Cooper, and J. R. Schrieffer. Microscopic theory of superconductivity. *Phys. Rev.*, 106:162–164, Apr 1957.

[9] Xiaoying Xu, Yufan Li, and C. L. Chien. Spin-triplet pairing state evidenced by half-quantum flux in a noncentrosymmetric superconductor. *Phys. Rev. Lett.*, 124:167001, Apr 2020.

[10] D. Pines and P. Nozières. *The Theory of Quantum Liquids.* Addison-Wesley, New York, 1998.

[11] L. D. Landau. The theory of a fermi liquid. *JETP*, 3(6):920, 1957.

[12] M. Gell-Mann and K. A. Brueckner. Correlation energy of an electron gas at high density. *Phys. Rev.*, 106:364–368, Apr 1957.

[13] N. F. Mott. *Metal-Insulator Transitions.* Taylor and Francis, London, 1990.

[14] F. Gebhard. *The Mott Metal-Insulator Transition.* Springer tracts in modern physics, Berlin, 1997.

[15] B.H. Brandow. Electronic structure of mott insulators. *Advances in Physics*, 26(5):651–808, 1977.

[16] V. Korenman, J. L. Murray, and R. E. Prange. Local-band theory of itinerant ferromagnetism. i. fermi-liquid theory. *Phys. Rev. B*, 16:4032–4047, Nov 1977.

[17] N. W. Ashcroft and N. D. Mermin. *Solid-State Physics.* Holt-Saunders, Philadelphia, 1976.

[18] P. W. Anderson. Theory of magnetic exchange interactions: Exchange in insulators and semiconductors. volume 14 of *Solid State Physics*, pages 99–214. Academic Press, 1963.

[19] S. Nakatsuji, S. Ikeda, and Y. Maeno. Ca_2RuO_4: New Mott Insulators of Layered Ruthenate. *Journal of the Physical Society of Japan*, 66(7):1868–1871, 1997.

[20] Y. Maeno, H. Hashimoto, K. Yoshida, S. Nishizaki, T. Fujita, J. G. Bednorz, and F. Lichtenberg. Superconductivity in a layered perovskite without copper. *Nature*, 372:532–534, Dec 1994.

[21] M. Braden, G. André, S. Nakatsuji, and Y. Maeno. Crystal and magnetic structure of Ca_2RuO_4 : Magnetoelastic coupling and the metal-insulator transition. *Phys. Rev. B*, 58:847–861, Jul 1998.

[22] S. Nakatsuji and Y. Maeno. Quasi-Two-Dimensional Mott Transition System $Ca_{2-x}Sr_xRuO_4$. *Phys. Rev. Lett.*, 84:2666–2669, Mar 2000.

[23] S. Nakatsuji, D. Hall, L. Balicas, Z. Fisk, K. Sugahara, M. Yoshioka, and Y. Maeno. Heavy-mass fermi liquid near a ferromagnetic instability in layered ruthenates. *Phys. Rev. Lett.*, 90:137202, Apr 2003.

[24] O. Friedt, M. Braden, G. André, P. Adelmann, S. Nakatsuji, and Y. Maeno. Structural and magnetic aspects of the metal-insulator transition in $Ca_{2-x}Sr_xRuO_4$. *Phys. Rev. B*, 63:174432, Apr 2001.

[25] E. Gorelov, M. Karolak, T. O. Wehling, F. Lechermann, A. I. Lichtenstein, and E. Pavarini. Nature of the Mott Transition in Ca_2RuO_4. *Phys. Rev. Lett.*, 104:226401, Jun 2010.

[26] P. L. Alireza, F. Nakamura, S. K. Goh, Y. Maeno, S. Nakatsuji, Y. T. C Ko, M. Sutherland, S. Julian, and G. G. Lonzarich. Evidence of superconductivity on the border of quasi-2D ferromagnetism in Ca_2RuO_4 at high pressure. *Journal of Physics: Condensed Matter*, 22:052202, Jan 2010.

[27] F. Nakamura, M. Sakaki, Y. Yamanaka, S. Tamaru, T. Suzuki, and Y. Maeno. Electric-field-induced metal maintained by current of the Mott insulator Ca_2RuO_4. *Scientific Reports*, 3:2536 EP –, Aug 2013.

[28] R. Okazaki, Y. Nishina, Y. Yasui, F. Nakamura, T. Suzuki, and I. Terasaki. Current-Induced Gap Suppression in the Mott Insulator Ca_2RuO_4. *Journal of the Physical Society of Japan*, 82(10):103702, 2013.

[29] F. Nakamura, T. Goko, M. Ito, T. Fujita, S. Nakatsuji, H. Fukazawa, Y. Maeno, P. Alireza, D. Forsythe, and S. R. Julian. From Mott insulator to ferromagnetic metal: A pressure study of Ca_2RuO_4. *Phys. Rev. B*, 65:220402, May 2002.

[30] Hideto Fukazawa, Satoru Nakatsuji, and Yoshiteru Maeno. Intrinsic properties of the Mott insulator $Ca_2RuO_{4+\delta}$ ($\delta = 0$) studied with single crystals. *Physica B: Condensed Matter*, 281-282:613–614, 2000.

[31] J. Zhang, A. S. McLeod, Q. Han, X. Chen, H. A. Bechtel, Z. Yao, S. N. Gilbert Corder, T. Ciavatti, T. H. Tao, M. Aronson, G. L. Carr, M. C. Martin, C. Sow, S. Yonezawa, F. Nakamura, I. Terasaki, D. N. Basov, A. J. Millis, Y. Maeno, and M. Liu. Nano-Resolved Current-Induced Insulator-Metal Transition in the Mott Insulator Ca_2RuO_4. *Phys. Rev. X*, 9:011032, Feb 2019.

[32] C. Sow, R. Numasaki, G. Mattoni, S. Yonezawa, N. Kikugawa, S. Uji, and Y. Maeno. In Situ Control of Diamagnetism by Electric Current in $Ca_3(Ru_{1-x}Ti_x)_2O_7$. *Phys. Rev. Lett.*, 122:196602, May 2019.

[33] G. Cao, S. McCall, M. Shepard, J. E. Crow, and R. P. Guertin. Magnetic and transport properties of single-crystal $\mathbf{ca_2ruo_4}$: relationship to superconducting $\mathbf{sr_2ruo_4}$. *Phys. Rev. B*, 56:R2916–R2919, Aug 1997.

[34] M. Sakaki, N. Nakajima, F. Nakamura, Y. Tezuka, and T. Suzuki. Electric-Field-Induced Insulator–Metal Transition in Ca_2RuO_4 Probed by X-ray Absorption and Emission Spectroscopy. *Journal of the Physical Society of Japan*, 82(9):093707, 2013.

[35] C. S. Alexander, G. Cao, V. Dobrosavljevic, S. McCall, J. E. Crow, E. Lochner, and R. P. Guertin. Destruction of the mott insulating ground state of ca_2ruo_4 by a structural transition. *Phys. Rev. B*, 60:R8422–R8425, Sep 1999.

[36] G. H. Major, N. Fairley, P. M. A. Sherwood, M. R. Linford, J. Terry, V. Fernandez, and K. Artyushkova. Practical guide for curve fitting in x-ray photoelectron spectroscopy. *Journal of Vacuum Science & Technology A*, 38(6):061203, 2020.

[37] D. Sutter, M. Kim, C. E. Matt, M. Horio, R. Fittipaldi, A. Vecchione, V. Granata, K. Hauser, Y. Sassa, G. Gatti, M. Grioni, M. Hoesch, T. K. Kim, E. Rienks, N. C. Plumb, M. Shi, T. Neupert, A. Georges, and J. Chang. Orbitally selective breakdown of Fermi liquid quasiparticles in $Ca_{1.8}Sr_{0.2}RuO_4$. *Phys. Rev. B*, 99:121115, Mar 2019.

[38] Y. Maeno, T. Ando, Y. Mori, E. Ohmichi, S. Ikeda, S. NishiZaki, and S. Nakatsuji. Enhancement of Superconductivity of Sr_2RuO_4 to 3 K by Embedded Metallic Microdomains. *Phys. Rev. Lett.*, 81:3765–3768, Oct 1998.

[39] X. Wang, Y. Zhong, D. Wang, L. Sun, B. Jiang, and J. Wang. Effect of interfacial energy on microstructure of a directionally solidified Al_2O_3/YAG eutectic ceramic. *Journal of the American Ceramic Society*, 101(3):1029–1035, 2018.

[40] R. Qun, S. Haijun, Z Jun, F. Guangrao, M. Weidan, L. Haifang, G. Min, L. Lin, and F. Hengzhi. Microstructure control, competitive growth and precipitation rule in faceted $Al_2O_3/Er_3Al_5O_{12}$ eutectic in situ composite ceramics prepared by laser floating zone melting. *Journal of the European Ceramic Society*, 39(5):1900–1908, 2019.

[41] V. Granata, R. Fittipaldi, A. Guarino, A. Ubaldini, E. Carleschi, A. M. Strydom, F. Chiarella, and A. Vecchione. Crystal growth of the Ca_2RuO_4–Ru metal system by the floating-zone technique. *Journal of Alloys and Compounds*, 832:154890, 2020.

[42] K. Jenni, F. Wirth, K. Dietrich, L. Berger, Y. Sidis, S. Kunkemöller, C. P. Grams, D. I. Khomskii, J. Hemberger, and M. Braden. Evidence for current-induced phase coexistence in Ca_2RuO_4 and its influence on magnetic order. *Physical Review Materials*, 4(8):85001, 2020.

[43] B. Keimer, S. A. Kivelson, M. R. Norman, S. Uchida, and J. Zaanen. From quantum matter to high-temperature superconductivity in copper oxides. *Nature*, 518(7538):179–186, 2015.

[44] P. J. W. Moll, Pallavi Kushwaha, Nabhanila Nandi, Burkhard Schmidt, and Andrew P. Mackenzie. Evidence for hydrodynamic electron flow in $PdCoO_2$. *Science*, 351(6277):1061–1064, 2016.

[45] Joseph A. Sulpizio, Lior Ella, Asaf Rozen, John Birkbeck, David J. Perello, Debarghya Dutta, Moshe Ben-Shalom, Takashi Taniguchi, Kenji Watanabe, Tobias Holder, Raquel Queiroz, Alessandro Principi, Ady Stern, Thomas Scaffidi, Andre K. Geim, and Shahal Ilani. Visualizing Poiseuille flow of hydrodynamic electrons. *Nature*, 576(7785):75–79, dec 2019.

[46] Juan M. Maldacena. The Large N Limit of Superconformal Field Theories and Supergravity. *International Journal of Theoretical Physics*, 38(4):1113–1133, 1997.

[47] Sean A. Hartnoll, Andrew Lucas, and Subir Sachdev. Holographic quantum matter. Preprint at http://arxiv.org/abs/1612.07324. 2016.

[48] M. Zhu, J. Peng, T. Zou, K. Prokes, S. D. Mahanti, T. Hong, Z. Q. Mao, G. Q. Liu, and X. Ke. Colossal Magnetoresistance in a Mott Insulator via Magnetic Field-Driven Insulator-Metal Transition. *Physical Review Letters*, 116(21), 2016.

[49] Yoshiteru Maeno, Shunichiro Kittaka, Takuji Nomura, Shingo Yonezawa, and Kenji Ishida. Evaluation of spin-triplet superconductivity in Sr_2RuO_4. *Journal of the Physical Society of Japan*, 81(1):1–29, 2012.

[50] Anthony J. Leggett and Ying Liu. Symmetry Properties of Superconducting Order Parameter in Sr_2RuO_4 : A Brief Review. *Journal of Superconductivity and Novel Magnetism*, 2020.

[51] G. Cao, S. McCall, J. E. Crow, and R. P. Guertin. Observation of a metallic antiferromagnetic phase and metal to nonmetal transition in $Ca_3Ru_2O_7$. *Physical Review Letters*, 78(9):1751–1754, 1997.

[52] S. A. Grigera, R. S. Perry, A. J. Schofield, M. Chiao, S. R. Julian, G. G. Lonzarich, S. I. Ikeda, Y. Maeno, A. J. Millis, and A. P. Mackenzie. Magnetic Field-Tuned Quantum Criticality in the Metallic Ruthenate $Sr_3Ru_2O_7$. *Science*, 294(5541):329–332, 2001.

[53] C. Cirillo, V. Granata, G. Avallone, R. Fittipaldi, C. Attanasio, A. Avella, and A. Vecchione. Emergence of a metallic metastable phase induced by electrical current in Ca_2RuO_4. *Phys. Rev. B*, 100(23):1–9, 2019.

[54] K. Fürsich, J. Bertinshaw, P. Butler, M. Krautloher, M. Minola, and B. Keimer. Raman scattering from current-stabilized nonequilibrium phases in Ca_2RuO_4. *Physical Review B*, 100(8):1–5, 2019.

[55] Satoru Nakatsuji, Takashi Ando, Zhiqiang Mao, and Yoshiteru Maeno. Metal–insulator transition in $Ca_{x-2}Sr_xRuO_4$. *Physica B: Condensed Matter*, 259-261:949–950, 1999.

[56] Satoru Nakatsuji and Yoshiteru Maeno. Synthesis and Single-Crystal Growth of $Ca_{x-2}Sr_xRuO_4$. *Journal of Solid State Chemistry*, 156(1):26 – 31, 2001.

[57] P. Steffens, O. Friedt, P. Alireza, W. G. Marshall, W. Schmidt, F. Nakamura, S. Nakatsuji, Y. Maeno, R. Lengsdorf, M. M. Abd-Elmeguid, and M. Braden. High-pressure diffraction studies on Ca_2RuO_4. *Phys. Rev. B*, 72(9):1–7, 2005.

[58] Fumihiko Nakamura. Pressure-Induced Mott Transition and Related Novel Quantum Phenomena in Ca_2RuO_4. *Journal of the Physical Society of Japan*, 76(Suppl.A):96–99, 2007.

[59] I. Zegkinoglou, J. Strempfer, C. S. Nelson, J. P. Hill, J. Chakhalian, C. Bernhard, J. C. Lang, G. Srajer, H. Fukazawa, S. Nakatsuji, Y. Maeno, and B. Keimer. Orbital ordering transition in Ca_2RuO_4 observed with resonant X-ray diffraction. *Physical Review Letters*, 95(13):1–4, 2005.

[60] Y. Taguchi, T. Matsumoto, and Y. Tokura. Dielectric breakdown of one-dimensional Mott insulators Sr_2CuO_3 and $SrCuO_2$. *Phys. Rev. B*, 62:7015–7018, 2000.

[61] Teruo Kanki, Kenichi Kawatani, Hidefumi Takami, and Hidekazu Tanaka. Direct observation of giant metallic domain evolution driven by electric bias in VO_2 thin films on $TiO_2(001)$ substrate. *Applied Physics Letters*, 101(24):243118, 2012.

[62] Zheng Yang, Changhyun Ko, and Shriram Ramanathan. Oxide electronics utilizing ultrafast metal-insulator transitions. *Annual Review of Materials Research*, 41(1):337–367, 2011.

[63] Pablo Stoliar, Julien Tranchant, Benoit Corraze, Etienne Janod, Marie-Paule Besland, Federico Tesler, Marcelo Rozenberg, and Laurent Cario. A leaky-integrate-and-fire neuron analog realized with a Mott insulator. *Advanced Functional Materials*, 27(11):1604740, 2017.

[64] Giordano Mattoni, Shingo Yonezawa, Fumihiko Nakamura, and Yoshiteru Maeno. Role of local temperature in the current-driven metal-insulator transition of Ca_2RuO_4. *Phys. Rev. Materials*, 4:114414, 2020.

[65] Ichiro Terasaki, Isuzu Sano, Kosuke Toda, Shuji Kawasaki, Akitoshi Nakano, Hiroki Taniguchi, Hai Jun Cho, Hiromichi Ohta, and Fumihiko Nakamura. Non-equilibrium Steady State in the Mott Insulator Ca_2RuO_4. *Journal of the Physical Society of Japan*, 89(9):093707, 2020.

[66] Giuliano Chiriacò and Andrew J. Millis. Polarity dependent heating at the phase interface in metal-insulator transitions. *Phys. Rev. B*, 102:085116, 2020.

[67] Yuan Huang, Eli Sutter, Norman N. Shi, Jiabao Zheng, Tianzhong Yang, Dirk Englund, Hong-Jun Gao, and Peter Sutter. Reliable exfoliation of large-area high-quality flakes of graphene and other two-dimensional materials. *ACS Nano*, 9(11):10612–10620, 2015.

[68] Atsushi Tsurumaki-Fukuchi, Keiji Tsubaki, Takayoshi Katase, Toshio Kamiya, Masashi Arita, and Yasuo Takahashi. Stable and tunable current-induced phase transition in epitaxial thin films of Ca_2RuO_4. *ACS Applied Materials & Interfaces*, 12(25):28368–28374, 2020.

[69] Ludi Miao, Punam Silwal, Xiaolan Zhou, Ilan Stern, Jin Peng, Wenyong Zhang, Leonard Spinu, Zhiqiang Mao, and Dae Ho Kim. Itinerant ferromagnetism and geometrically suppressed metal-insulator transition in epitaxial thin films of Ca_2RuO_4. *Applied Physics Letters*, 100(5):10–13, 2012.

[70] X. Wang, Y. Xin, P. A. Stampe, R. J. Kennedy, and J. P. Zheng. Epitaxial thin film growth of $Ca_2RuO_{4+\delta}$ by pulsed laser deposition. *Applied Physics Letters*, 85(25):6146–6148, 2004.

[71] C. Dietl, S. K. Sinha, G. Christiani, Y. Khaydukov, T. Keller, D. Putzky, S. Ibrahimkutty, P. Wochner, G. Logvenov, P. A. van Aken, B. J. Kim, and B. Keimer. Tailoring the electronic properties of Ca_2RuO_4 via epitaxial strain. *Applied Physics Letters*, 112(3):031902, 2018.

[72] Yuuki Yasui, Kaveh Lahabi, Victor Fernández Becerra, Remko Fermin, Muhammad Shahbaz Anwar, Shingo Yonezawa, Takahito Terashima, Milorad V. Milošević, Jan Aarts, and Yoshiteru Maeno. Spontaneous emergence of Josephson junctions in homogeneous rings of single-crystal Sr_2RuO_4. *npj Quantum Materials*, 5(1):1–8, 2020.

[73] Vadim Grinenko, Shreenanda Ghosh, Rajib Sarkar, Jean Christophe Orain, Artem Nikitin, Matthias Elender, Debarchan Das, Zurab Guguchia, Felix Brückner, Mark E. Barber, Joonbum Park, Naoki Kikugawa, Dmitry A. Sokolov, Jake S. Bobowski, Takuto Miyoshi, Yoshiteru Maeno, Andrew P. Mackenzie, Hubertus Luetkens, Clifford W. Hicks, and Hans Henning Klauss. Split superconducting and time-reversal symmetry-breaking transitions in Sr_2RuO_4 under stress. *Nature Physics*, 17(6):748–754, 2021.

[74] M. E. Barber, A. S. Gibbs, Y. Maeno, A. P. Mackenzie, and C. W. Hicks. Resistivity in the vicinity of a van Hove singularity: Sr_2RuO_4 under uniaxial pressure. *Physical Review Letters*, 120(7):76602, 2018.

[75] Alexander Steppke, Lishan Zhao, Mark E. Barber, Thomas Scaffidi, Fabian Jerzembeck, Helge Rosner, Alexandra S. Gibbs, Yoshiteru Maeno, Steven H. Simon, Andrew P. Mackenzie, and Clifford W. Hicks. Strong peak in T_c of Sr_2RuO_4 under uniaxial pressure. *Science*, 355(6321), 2017.

[76] Matthias Lange, Stefan Guénon, Yoav Kalcheim, Theodor Luibrand, Nicolas Manuel Vargas, Dennis Schwebius, Reinhold Kleiner, Ivan K. Schuller, and Dieter Koelle. Optical imaging of strain-mediated phase coexistence during electrothermal switching in a Mott insulator. Preprint at https://arxiv.org/abs/2009.12536. 2020.

[77] E. Bauer, G. Hilscher, H. Michor, Ch. Paul, E. W. Scheidt, A. Gribanov, Yu. Seropegin, H. Noël, M. Sigrist, and P. Rogl. Heavy Fermion Superconductivity and Magnetic Order in Noncentrosymmetric $CePt_3Si$. *Phys. Rev. Lett.*, 92:027003, Jan 2004.

[78] E. Bauer, I. Bonalde, and M. Sigrist. Superconductivity and normal state properties of non-centrosymmetric $CePt_3Si$: a status report. *Low Temperature Physics*, 31(8):748–756, 2005.

[79] P A Frigeri, D F Agterberg, and M Sigrist. Spin susceptibility in superconductors without inversion symmetry. *New Journal of Physics*, 6:115–115, sep 2004.

[80] P. A. Frigeri, D. F. Agterberg, A. Koga, and M. Sigrist. Superconductivity without Inversion Symmetry: MnSi versus $CePt_3Si$. *Phys. Rev. Lett.*, 92:097001, Mar 2004.

[81] J. Chen, M. B. Salamon, S. Akutagawa, J. Akimitsu, J. Singleton, J. L. Zhang, L. Jiao, and H. Q. Yuan. Evidence of nodal gap structure in the noncentrosymmetric superconductor Y_2C_3. *Phys. Rev. B*, 83:144529, Apr 2011.

[82] N. Kimura, K. Ito, H. Aoki, S. Uji, and T. Terashima. Extremely High Upper Critical Magnetic Field of the Noncentrosymmetric Heavy Fermion Superconductor $CeRhSi_3$. *Phys. Rev. Lett.*, 98:197001, May 2007.

[83] R. Settai, Y. Miyauchi, T. Takeuchi, F. Lévy, I. Sheikin, and Y. Ōnuki. Huge Upper Critical Field and Electronic Instability in Pressure-induced Superconductor $CeIrSi_3$ without Inversion Symmetry in the Crystal Structure. *Journal of the Physical Society of Japan*, 77(7):073705, 2008.

[84] M. Smidman, M. B. Salamon, H. Q. Yuan, and D. F. Agterberg. Superconductivity and spin–orbit coupling in non-centrosymmetric materials: a review. *Reports on Progress in Physics*, 80(3):036501, jan 2017.

[85] N. Kimura, K. Ito, K. Saitoh, Y. Umeda, H. Aoki, and T. Terashima. Pressure-Induced Superconductivity in Noncentrosymmetric Heavy-Fermion $CeRhSi_3$. *Phys. Rev. Lett.*, 95:247004, Dec 2005.

[86] T. Akazawa, H. Hidaka, T. Fujiwara, T.C. Kobayashi, E. Yamamoto, Y. Haga, R. Settai, and Y. Nuki. Pressure-induced superconductivity in ferromagnetic UIr without inversion symmetry. *Journal of Physics: Condensed Matter*, 16(4):L29–L32, jan 2004.

[87] M. Sigrist E. Bauer. *Non-Centrosymmetric Superconductors*. Springer-Verlag Berlin Heidelberg, Physics Editorial Department I Tiergartenstrasse 17 69121 Heidelberg/Germany, 2012.

[88] A. B. Karki, Y. M. Xiong, N. Haldolaarachchige, S. Stadler, I. Vekhter, P. W. Adams, D. P. Young, W. A. Phelan, and Julia Y. Chan. Physical properties of the noncentrosymmetric superconductor $Nb_{0.18}Re_{0.82}$. *Phys. Rev. B*, 83:144525, Apr 2011.

[89] Susumu Katano, Kohei Shibata, Kotaro Nakashima, and Yohei Matsubara. Magnetic impurity effects on the superconductivity of noncen-

trosymmetric $LaNiC_2$: Ce substitution for La. *Phys. Rev. B*, 95:144502, Apr 2017.

[90] K. Togano, P. Badica, Y. Nakamori, S. Orimo, H. Takeya, and K. Hirata. Superconductivity in the metal rich li-pd-b ternary boride. *Phys. Rev. Lett.*, 93:247004, Dec 2004.

[91] Petre Badica, Takaaki Kondo, and Kazumasa Togano. Superconductivity in a New Pseudo-Binary $Li_2B(Pd_{1-x}Pt_x)_3$ (x=0–1) Boride System. *Journal of the Physical Society of Japan*, 74(3):1014–1019, 2005.

[92] Takeshi Shibayama, Minoru Nohara, Hiroko Aruga Katori, Yoshihiko Okamoto, Zenji Hiroi, and Hidenori Takagi. Superconductivity in rh_2ga_9 and ir_2ga_9 without inversion symmetry. *Journal of the Physical Society of Japan*, 76(7):073708, 2007.

[93] A. B. Karki, Y. M. Xiong, I. Vekhter, D. Browne, P. W. Adams, D. P. Young, K. R. Thomas, Julia Y. Chan, H. Kim, and R. Prozorov. Structure and physical properties of the noncentrosymmetric superconductor Mo_3Al_2C. *Phys. Rev. B*, 82:064512, Aug 2010.

[94] E. Bauer, G. Rogl, Xing-Qiu Chen, R. T. Khan, H. Michor, G. Hilscher, E. Royanian, K. Kumagai, D. Z. Li, Y. Y. Li, R. Podloucky, and P. Rogl. Unconventional superconducting phase in the weakly correlated noncentrosymmetric Mo_3Al_2C compound. *Phys. Rev. B*, 82:064511, Aug 2010.

[95] M. Nishiyama, Y. Inada, and Guo-qing Zheng. Spin Triplet Superconducting State due to Broken Inversion Symmetry in Li_2Pt_3B. *Phys. Rev. Lett.*, 98:047002, Jan 2007.

[96] K. Tahara, Z. Li, H. X. Yang, J. L. Luo, S. Kawasaki, and Guo-qing Zheng. Superconducting state in the noncentrosymmetric $Mg_{9.3}Ir_{19}B_{16.7}$ and $Mg_{10.5}Ir_{19}B_{17.1}$ revealed by NMR. *Phys. Rev. B*, 80:060503, Aug 2009.

[97] H. Takeya, M. ElMassalami, S. Kasahara, and K. Hirata. Specific-heat studies of the spin-orbit interaction in noncentrosymmetric $Li_2(Pd_{1-x}Pt_x)_3B$ $(x = 0, 0.5, 1)$ superconductors. *Phys. Rev. B*, 76:104506, Sep 2007.

[98] F. Kneidinger, E. Bauer, I. Zeiringer, P. Rogl, C. Blaas-Schenner, D. Reith, and R. Podloucky. Superconductivity in non-centrosymmetric materials. *Physica C: Superconductivity and its Applications*, 514:388–398, 2015. Superconducting Materials: Conventional, Unconventional and Undetermined.

[99] J. F. Landaeta, D. Subero, P. Machado, F. Honda, and I. Bonalde. Unconventional superconductivity and an ambient-pressure magnetic quantum critical point in single-crystal $LaNiC_2$. *Phys. Rev. B*, 96:174515, Nov 2017.

[100] C. S. Lue, T. H. Su, H. F. Liu, and Ben-Li Young. Evidence for s-wave superconductivity in noncentrosymmetric $Re_{24}Nb_5$ from ^{93}Nb NMR measurements. *Phys. Rev. B*, 84:052509, Aug 2011.

[101] J. Chen, L. Jiao, J. L. Zhang, Y. Chen, L. Yang, M. Nicklas, F. Steglich, and H. Q. Yuan. BCS-like superconductivity in the noncentrosymmetric compounds Nb_xRe_{1-x} ($0.13 \leq x \leq 0.38$). *Phys. Rev. B*, 88:144510, Oct 2013.

[102] C. Cirillo, R. Fittipaldi, M. Smidman, G. Carapella, C. Attanasio, A. Vecchione, R. P. Singh, M. R. Lees, G. Balakrishnan, and M. Cuoco. Evidence of double-gap superconductivity in noncentrosymmetric $Nb_{0.18}Re_{0.82}$ single crystals. *Phys. Rev. B*, 91:134508, Apr 2015.

[103] Crystal growth of the non-centrosymmetric superconductor $Nb_{0.18}Re_{0.82}$. *Journal of Crystal Growth*, 361:129–131, 2012.

[104] T. Shang, M. Smidman, S. K. Ghosh, C. Baines, L. J. Chang, D. J. Gawryluk, J. A. T. Barker, R. P. Singh, D. McK. Paul, G. Balakrishnan, E. Pomjakushina, M. Shi, M. Medarde, A. D. Hillier, H. Q. Yuan, J. Quintanilla, J. Mesot, and T. Shiroka. Time-reversal symmetry breaking in re-based superconductors. *Phys. Rev. Lett.*, 121:257002, Dec 2018.

[105] C. C. Tsuei and J. R. Kirtley. Pairing symmetry in cuprate superconductors. *Rev. Mod. Phys.*, 72:969–1016, Oct 2000.

[106] Bascom S. Deaver and William M. Fairbank. Experimental evidence for quantized flux in superconducting cylinders. *Phys. Rev. Lett.*, 7:43–46, Jul 1961.

[107] R. Doll and M. Näbauer. Experimental proof of magnetic flux quantization in a superconducting ring. *Phys. Rev. Lett.*, 7:51–52, Jul 1961.

[108] N. Byers and C. N. Yang. Theoretical considerations concerning quantized magnetic flux in superconducting cylinders. *Phys. Rev. Lett.*, 7:46–49, Jul 1961.

[109] W. A. Little and R. D. Parks. Observation of quantum periodicity in the transition temperature of a superconducting cylinder. *Phys. Rev. Lett.*, 9:9–12, Jul 1962.

[110] R. D. Parks and W. A. Little. Fluxoid quantization in a multiply-connected superconductor. *Phys. Rev.*, 133:A97–A103, Jan 1964.

[111] P. L. Gammel, P. A. Polakos, C. E. Rice, L. R. Harriott, and D. J. Bishop. Little-Parks oscillations of T_c in patterned microstructures of the oxide superconductor $YBa_2Cu_3O_7$: Experimental limits on fractional-statistics-particle theories. *Phys. Rev. B*, 41:2593–2596, Feb 1990.

[112] X. Cai, Y. A. Ying, N. E. Staley, Y. Xin, D. Fobes, T. J. Liu, Z. Q. Mao, and Y. Liu. Unconventional quantum oscillations in mesoscopic rings of spin-triplet superconductor Sr_2RuO_4. *Phys. Rev. B*, 87:081104, Feb 2013.

[113] V. B. Geshkenbein, A. I. Larkin, and A. Barone. Vortices with half magnetic flux quanta in "heavy-fermion" superconductors. *Phys. Rev. B*, 36:235–238, Jul 1987.

[114] Yufan Li, Xiaoying Xu, M.-H. Lee, M.-W. Chu, and C. L. Chien. Observation of half-quantum flux in the unconventional superconductor β-Bi_2Pd. *Science*, 366(6462):238–241, 2019.

[115] C. Cirillo, G. Carapella, M. Salvato, R. Arpaia, M. Caputo, and C. Attanasio. Superconducting properties of noncentrosymmetric $Nb_{0.18}Re_{0.82}$ thin films probed by transport and tunneling experiments. *Phys. Rev. B*, 94:104512, Sep 2016.

[116] M. Tinkham. *Introduction to Superconductivity.* International series in pure and applied physics. McGraw Hill, 1996.

[117] Yuuki Yasui, Kaveh Lahabi, Muhammad Shahbaz Anwar, Yuji Nakamura, Shingo Yonezawa, Takahito Terashima, Jan Aarts, and Yoshiteru Maeno. Little-Parks oscillations with half-quantum fluxoid features in Sr_2RuO_4 microrings. *Phys. Rev. B*, 96:180507, Nov 2017.

[118] Franco Carillo, Gianpaolo Papari, Daniela Stornaiuolo, Detlef Born, Domenico Montemurro, Pasqualantonio Pingue, Fabio Beltram, and Francesco Tafuri. Little-Parks effect in single nanoscale $YBa_2Cu_3O_{6+x}$ rings. *Phys. Rev. B*, 81:054505, Feb 2010.

Acknowledgments

First of all, I would like to thank my Italian supervisors Prof. Carmine Attanasio and Dr Carla Cirillo, and my foreign supervisor Prof. Jan Aarts. I am very grateful to him for allowing me to join his very prestigious and friendly research group in Leiden. The valuable and very stimulating discussions with him were of inestimable value and helped me grow scientifically and personally. His experience and knowledge, together with his kindly and permissive character that prevailed in any situation, made him my point of reference. Thank you very much, Jan.

I am extremely grateful to Dr Antonio Vecchione for his expert leadership and patience with me, for helping me in any situation providing every time nice and elegant solutions. During these years, I have looked at him as a Mentor, someone I could always rely on, a very talented scientist from all points of view, a special person, a friend... "Grazie Maestro!".

My special thanks go to Dr Umberto Gambardella, who helped me to face up the many problems that I have encountered during the PhD period. He is always a rock to lean on, and I am happy that he welcomed me in his "fantastic" group as a son. I thank him also for allowing me, during these difficult months, to work on the writing of this thesis in complete serenity.

I would like to convey my gratitude to the director of our department, Prof. Salvatore De Pasquale, for helping me during the last period of my PhD work.

Warm thanks go to Prof. Canio Noce, that I always consider a very very very brilliant physicist. I really appreciate his priceless help in the last period.

I want to thank Prof. Alfonso Romano for his continued interest in me and for the encouragement he has given to me.

I thank Dr Mario Cuoco that I like to call "il cucinatore di idee" for the helpful discussions and the theoretical suggestions.

I am very thankful to Veronica for helping me during the PhD years. Her determination, her impressive way to approach the life, and her incredible patience are unique. I wish you all the best in your career, Veronica!

I am very grateful to Paola Gentile that without her impactful competencies and her help, my thesis would lack an important piece of theoretical physics. She encouraged me many many times with her irrepressible tenacity in difficult moments.
I want to manifest my sincere gratitude to Tatiana for her friendship and for the many perspicacious conversations. She helped and encouraged me in different circumstances, and always made me feel very welcome in her laboratory during these years.
I would like to give my huge gratitude to my "new" colleagues and friends for their moral support, Gerardo "Gerannone", Domenico "Austino", Amedeo "il tecnico affascinante", Nello Saggese "il tecnico che come me ama la follia negli esperimenti", Enrico "lo zio", Claudio "la roccia che cammina", and Fabio "che è finito nel laboratorio dei pazzi".
Many thanks to Antonio Leo, Prof. Marco, Ofelia, Paola Forlenza, Stefano, Elisabetta, Daniela Mayo, Danilo Romano, Fabio Caliendo, and all the people of the Physics Department of Salerno for their friendship, availability, advice, and lots of moral support. I want to thank also Carmen, Enzo, Dino, and Fabiana. They were always available and kind to me, like a family.
I cannot forget the fantastic period I spent in the Netherlands. Who forgets Kaveh? He makes me feel at home from the first day I meet him. A brilliant physicist, I learned a lot from him. Thank you for everything wajiò... and at the end of the day I really enjoyed the time we spent speaking about Physics... and I think he really likes my songs on him that I wrote and rehearsed with Remko, another very skilled colleague and friend that I meet in the MSM group. We worked together in a very nice atmosphere combining the work with our craziness. There were no sad days at work, especially when we talked about "the quality"! Thank you very much for everything also to you wajiò. A big thank you is for Dyon, my Dutch friend, but with Italian habits. Our after-lunch coffee and the passion for good food took me to Salerno for a moment every day. I am also grateful to the "intrusive" (let's say Italian) technician Federica that although she was originally from north Italy at the end of the day was a nice person. Thank you for your support and your pieces of advice, "polentona"!
Finally, I would like to express my love to my family, dad, mum, and the "little" brother, thank you all for your constant support, for your belief in me and for being close to me in the bad and good times. I would like to give a huge thanks to my Angela that always support "e sopporta" me.

At this moment while I am writing these lines, my thoughts go to my grandfather Antonio, to my grandmother Angela, who for me was like a second mother, and I am sure that today she would be very happy and proud of me. And then the pandemic that ripped my grandfather Angelo away from us in a horrible way. I still remember his tears of joy when I discussed the bachelor's degree, and unfortunately, I can only imagine how happy he would be today. My grandmother Giuseppina ("la nonna dei baci") tragically left us. I spent together with her a lot of lovely and special moments. Her spontaneity and sense of humour were exceptionally uniques. It is to all of them that I dedicate this thesis. I will never forget their teachings and their love.

List of Publications

- **G. Avallone**[†], R. Fermin[†], K. Lahabi, V. Granata, R. Fittipaldi, C. Cirillo, C. Attanasio, A. Vecchione, and J. Aarts, "Universal size-dependent nonlinear charge transport in single crystals of the Mott insulator Ca_2RuO_4", accepted for publication in *npj Quantum Materials – Nature.*

- E. Allahyari, J. JJ Nivas, **G. Avallone**, M. Valadan, M. Singh, V. Granata, C. Cirillo, A. Vecchione, R. Bruzzese, C. Altucci, and S. Amoruso, "Femtosecond laser surface irradiation of silicon in air: Pulse repetition rate influence on crater features and surface texture", *Optics & Laser Technology* **126**, 106073 (2020).

- C. Cirillo, V. Granata, **G. Avallone**, R. Fittipaldi, C. Attanasio, A. Avella, and A. Vecchione, "Emergence of a metallic metastable phase induced by electrical current in Ca_2RuO_4", *Phys. Rev. B* **100**, 235142 (2019).

- M. Salvato, M. Scagliotti, M. De Crescenzi, M. Boscardin, C. Attanasio, **G. Avallone**, C. Cirillo, P. Prosposito, F. De Matteis, R. Messi, and P. Castrucci, "Time response in carbon nanotube/Si based photodetectors", *Sensors and Actuators A: Physical.* **292**, 71-76 (2019).

[†]These authors contributed equally to this work.